
# THESE DE DOCTORAT
# DE SORBONNE UNIVERSITÉ

## Spécialité : Physique et Astrophysique

**École doctorale n°127 : Astronomie et astrophysique d'Ile de France**

**réalisée à**

## l'Institut d'Astrophysique de Paris

**présentée par**


# Hugo Pfister


**pour obtenir le grade de**

**DOCTEUR EN ASTROPHYSIQUE**

**Sujet de la thèse :**

## Dynamics of supermassive black holes in galaxies

**sous la direction de Marta Volonteri et Yohan Dubois**

## soutenue le 20 Septembre 2019

**devant le Jury composé de :**

| | |
|---|---|
| Marie-Christine Angonin | Présidente |
| Pau Amaro-Seoane | Rapporteur |
| Thorsten Naab | Rapporteur |
| Tamara Bogdanovic | Examinatrice |
| Fréderic Bournaud | Examinateur |
| Françoise Combes | Examinatrice |
| Yohan Dubois | Directeur |
| Marta Volonteri | Directrice |

# RÉSUMÉ

On trouve des trous noirs supermassifs au centre des galaxies les plus massives. De plus, on pense que les galaxies les plus massives proviennent partiellement de la fusion de galaxies moins massives. Par conséquent, suite à la fusion de galaxies, on s'attend à ce que des trous noirs se lient gravitationellement au centre de la galaxie obtenue, puis fusionnent en emettant des ondes gravitationelles que l'on detectera avec LISA dans un futur proche. Avec cette Thèse, je contribue à une meilleure compréhension de la formation des binaires de trous noirs (Chapitres 2 et 3). J'ai d'abord confirmé que la friction dynamique due aux étoiles peut suffisamment décélérer les trous noirs pour former une binaire séparée d'environ 1 pc; j'ai aussi montré que, pour prendre en compte cette décélération, les simulations doivent *a priori* résoudre la trainée ralentissant le trou noir, dont la taille est typiquement le rayon d'influence du trou noir. J'ai ensuite modélisé, implémenté et testé un modèle physique pour prendre en compte la friction dynamique des étoiles et de la matière noire dans les simulations cosmologiques, dont la résolution ne permet en général pas de résoudre la trainée, et donc dans les lesquelles la friction dynamique n'est pas prise en compte. Cela m'a permis d'étudier la formation des binaires de trous noirs dans un contexte cosmologique. J'ai trouvé que, à haut redshift, la distribution très irrégulière de la matière dans les jeunes galaxies conduit à une marche aléatoire des trous noirs de faible masse ($< 10^5\,M_\odot$), rendant la fusion et l'émission d'ondes gravitationelles peu probable, sauf s'ils sont situés dans une structure plus massive comme un amas stellaire nucléaire.

J'ai aussi travaillé sur les événements de rupture des étoiles par effets de marée, dont le nombre de détection va être multiplié par plusieurs ordres de grandeur grâce aux futurs relevés d'effets transitoires LSST ou eROSITA. En particulier, j'ai utilisé les résultats analytiques de la théorie du cône perdu à des profils stellaires réalistes obtenus grâce à une simulation de fusion de galaxies (Chapitre 4). Cela m'a permis d'étudier l'évolution du taux de rupture pendant les fusions de galaxies. J'ai trouvé que ce taux est multiplié par $\sim 30$ durant les $\sim 300$ millions d'années qui suivent la fusion, avec un pic où il est multiplié par plus de deux ordres de grandeur.

# ABSTRACT

Supermassive black holes (BHs) reside in the center of most massive galaxies. In addition, given our current understanding of galaxy formation, massive galaxies build up part of their mass through mergers with other galaxies. Consequently, following galaxy mergers, we expect BHs to gravitationally bind in the center of galaxy remnants and merge, emitting gravitational waves which we will detect with LISA in the near future. With this Thesis, I contribute to a better understanding of the formation of binary BHs (Chapters 2 and 3). I first confirmed that dynamical friction in a stellar background can provide sufficient deceleration to form binaries on pc scales, and highlighted that in order to capture this deceleration, numerical simulations need *a priori* to resolve the wake lagging the BH, which has a size similar to the influence radius of the BH. Then I modeled, developed and tested a physically motivated model to take into account dynamical friction from stars and dark matter in cosmological simulations, in which the wake is usually not resolved and therefore in which dynamical friction is not correctly taken into account. This allowed me to study the formation of binary BHs in a cosmological context. I found that, at high redshift, the highly irregular distribution of matter in young galaxies leads to a physical random walk for low mass ($< 10^5\,M_\odot$) BHs, rendering mergers and gravitational waves emission unlikely, unless they are embedded into a more massive structure, like a nuclear star cluster.

I also worked on tidal disruption events of stars by BHs, whose detection will be enhanced by orders of magnitude with the next transient surveys LSST or eROSITA. In particular, I applied analytical results from the loss cone theory to realistic evolving stellar density profiles obtained from a galaxy merger simulation (Chapter 4). This allowed me to estimate how nuclear star formation affects the evolution of the tidal disruption event rate during mergers. I found that the mean enhancement can be $\sim 30$ during the $\sim 300\,\mathrm{Myr}$ following the merger, with a peak of more than two orders of magnitude enhancement.

# ACKNOWLEDGEMENTS

**Marta** and **Yohan**, thank you for teaching me basically all I know about astronomy and research. We have had some disagreement (who talked about boosts?), but you considered my ideas and opinions as equally as yours. Thank you also for giving me freedom to do research I like, even if this means changing the title of this Thesis.

Thank you **Massimo** and **Monica** for hosting me in Milan. It was a pleasure to eat pizze everyday, have aperetivo, play GeoGuessr and thanks for introducing me to climbing.

Thanks to the members of the Jury: **Marie-Christine Angonin**, **Pau Amaro-Seoane**, **Thorsten Naab**, **Tamara Bogdanovic**, **Frédéric Bournaud** and **Françoise Combes**. I particularly thank Pau and Thorsten for accepting to review the manuscript, and Tamara for crossing the Atlantic ocean to attend the defense.

Thank you **Jane** and **Enrico** for hiring me in Copenhagen/Hong-Kong and took a load off my shoulders just before I started writing the manuscript, nice timing.

Merci aux **co-doctorants** pour ces cafés et ces discussions au milieu de l'aprem.

Merci au **club resto**, aux **GP** et aux **habitués du mardi** pour toutes ces bières, chacune d'entre elles bue avec vous est un plaisir.

Merci à toute la **famille**, particulièrement **Dad**, **Mom**, **Clara** et **Poky** pour me rappeler quotidiennent que j'ai un métier utile à la société.

Enfin, merci **Ise** pour ta patience, ton support, ton rire et ta (plutôt) bonne humeur durant toutes ces années (pas que pendant la thèse). Voilà, j'ai rayé "manuscrit" de ma todo-list à tes côtés, et j'espère encore rayer pleins de trucs à tes côtés. Copenhague, Hong-Kong, autre part...? peu importe, tant que tu es là ça sera chouette.

# ACRONYMS

AGN Active Galactic Nucleus

AMR Adaptive Mesh Refinement

BH Black Hole

CIC Cloud In Cell

CMB Cosmic Microwave Background

NFW Navarro Frenk and White

LISA Large Interferometer Space Antenna

LSST Large Synoptic Survey Telescope

SPH Smooth Particle Hydrodynamics

TDE Tidal Disruption Event

# CONTENTS

# 1

# INTRODUCTION

In this Chapter, we first define the objects we will study in this Thesis: supermassive black holes (BHs) and galaxies. In particular, we give orders of magnitude for their size and mass. In the second part, we discuss how these objects have evolved since the beginning of the Universe about 14 billions years ago, and how they impacted each others during this time. Finally, in the third and fourth sections, we present two ways of observing black holes: gravitational waves and tidal disruption events (TDEs). We discuss the physical processes involved and how they correlate to the work done during this Thesis.

## 1.1 BLACK HOLES AND GALAXIES

We shall start by defining the words entering in the title of this Thesis: galaxy and (supermassive) black holes.

**Galaxies** are gravitationally bound objects formed by gas, stars and dark matter. The easiest component to understand are stars, as we are familiar with these objects, having one in our neighborhood (the Sun), and as they emit the light we see in well known images of galaxies (see Fig. 1). In the case of our own galaxy, The Milky-Way, stars take the form of a disc surrounding a bulge, similar to Fig. 1. The height of the disk is about 100 pc ($1\,\mathrm{pc} = 3.09 \times 10^{18}\,\mathrm{cm}$, for comparison, the Sun is at $1.5 \times 10^{13}\,\mathrm{cm}$ from Earth) and radius 10 kpc. The total mass of stars is $10^{11}\,\mathrm{M}_\odot$ (McMillan, 2011), where $\mathrm{M}_\odot$ is the mass of the Sun and equals $2 \times 10^{33}\,\mathrm{g}$, a direct consequence is that the disc of this image contains about $10^{11}$ stars! Mixed to these stars, there is gas, which mass is sub-dominant in our Galaxy, about $10^{10}\,\mathrm{M}_\odot$, but forms the reservoir of matter which will turn into stars, at current rate, about one star forms per year in our Galaxy (Robitaille and Whitney, 2010). Gas cannot be seen directly in Fig. 1 because the image is taken in the optical part of the light spectrum, where stars can be seen. At other wavelength (microwaves), where we can see gas, a similar disky shape appears. Finally, around this disc of gas and stars, there is a dark matter halo. The nature of dark matter is still poorly understood (Peter, 2012), but it forms the most massive part of galaxies, $10^{12}\,\mathrm{M}_\odot$ for our Milky-Way, and extent to 150 kpc.

We have observed galaxies for a long time. However, understanding that these objects are island Universes, as named by the german philosopher Kant, and not spiral nebulae in our own Galaxy, as suggested by the french observer Messier (Messier, 1781), has been a great debate in the 1920's. The answer has been given by the american astronomer Hubble (Hubble, 1925), who used cepheids, stars for which the periodicity in lightcurves depend on the absolute magnitude (Leavitt, 1908), from which he could infer the distance of these spiral nebulae and found out that they are much farther than the size of our Galaxy, proving they are island Universes.

Today, we know of millions of galaxies with different masses and sizes. The goal of galaxy evolution studies (*e.g.* Benson, 2010; Somerville and Davé, 2015; Naab and Ostriker, 2017) is to understand how these objects form and evolve, and by using physically motivated models, on the one hand reproduce observed quantities such as the number of galaxies per unit volume with a given mass (*i.e.* the galaxy mass function; see Fig. 2, left) or the relation between the mass of dark matter halos and of galaxies (see Fig. 2, right) and on the other hand make predictions on still unknown properties of the galaxy population, *e.g.* how galactic discs and bulges form or why star formation in some galaxies ends abruptly.

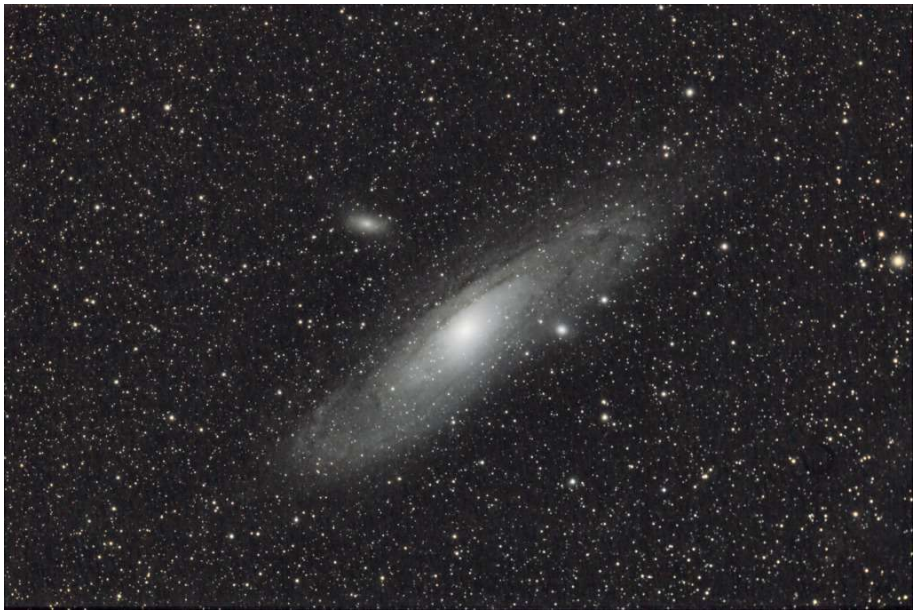

Figure 1: Image, in the optical part of the spectrum of the of the Andromeda Galaxy, or M31 in the Messier catalog (Messier, 1781).

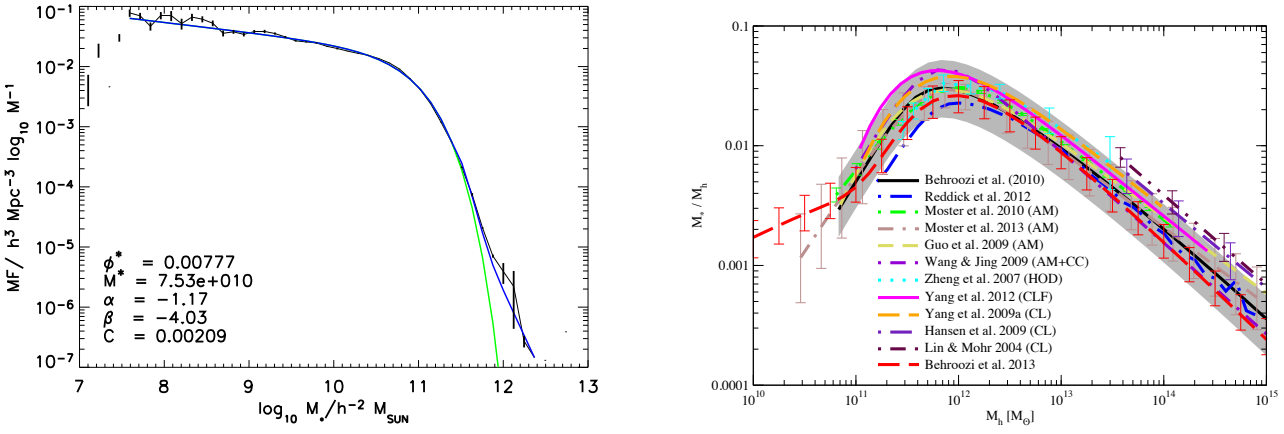


Figure 2: **Left:** Galaxy mass function at z=0. Taken from Panter, Heavens, and Jimenez, 2004. **Right:** Stellar mass to halo mass ratio as a function of the halo mass. Taken from Behroozi, Wechsler, and Conroy, 2013.

**Black holes** can be understood as following: *for an object of mass* $M_\bullet$, *what must be the radius,* $r$, *of this object such that, even light moving at a speed* $c$, *cannot escape?* This can be easily solved comparing the kinetic and gravitational energy of such a system:

$$\frac{G\,M_\bullet}{r} > \frac{1}{2}c^2 \tag{1}$$

$$\Leftrightarrow \quad r < r_{Sch} \equiv \frac{2G\,M_\bullet}{c^2} = 3\,\mathrm{km}\,\frac{M_\bullet}{M_\odot}\,, \tag{2}$$

where $r_{Sch}$ is the Schwarzschild radius. By some happy coincidence, the solution of general relativity outside a static point source object shows a similar behavior, where light cannot escape below $r_{Sch}$[1].

Given their compactness (see below for a clear definition), BHs are also formidable sources of energy. Consider an object with mass $m$ initially at rest and at infinite distance from another object of mass $M_\bullet$ and radius $r$. The change of energy when $m$ reaches the surface of $M_\bullet$ is:

$$\Delta E = -\frac{G\,M_\bullet\,m}{r} - 0 = -\Xi mc^2\,, \tag{3}$$

where we introduce the compactness $\Xi = G\,M_\bullet/(rc^2)$ and give some values in Table 1. As the total energy of the system has to be conserved, a fraction $\Xi$ of the rest mass energy is emitted in the surrounding, either through radiation, or through kinetic energy if some mass is expelled. For a BH[2], $\Xi = 50\%$, for comparison, the efficiency of hydrogen nuclear fusion which power stars is slightly less than 0.7%, making BHs the most efficient machines in the Universe to produce energy. When it is not an object with fixed mass falling onto the BH but, instead, a constant inflow of matter $\dot{M}_{acc}$, then the luminosity $L$ of the BH can be estimated as:

$$L = \Xi\dot{M}_{acc}c^2 \tag{4}$$

$$= 6\times10^{46}\,\mathrm{erg\ s^{-1}}\,\Xi\frac{\dot{M}_{acc}}{M_\odot\ \mathrm{yr}^{-1}} \tag{5}$$

$$= 10^{13}L_\odot\,\Xi\frac{\dot{M}_{acc}}{M_\odot\ \mathrm{yr}^{-1}}\,. \tag{6}$$

where $L_\odot$ corresponds to the luminosity of the Sun.

This tremendous amount of energy emitted is actually the observational signature of BHs but, while BHs have been theorized in the 1920's, firsts hints of their existence have

1 Schwarzschild was the person who performed the calculation in the general relativity framework, which explains the name of the typical radius.

2 The correct fraction obtained with a detailed calculation using the general relativity framework depends on the spin. It is about 10% but can go up to 42% for a rotating BH.

| **Object** | **Mass** ( $M_\bullet$ ) ( $M_\odot$ ) | **Radius** ( $r$ ) ( km ) | **Compactness** ( $\Xi$ ) |
|---|---|---|---|
| Earth | $3 \times 10^{-6}$ | 6000 | $7 \times 10^{-10}$ |
| Sun | 1 | 696 000 | $2 \times 10^{-6}$ |
| Stellar black hole | 10 | 30 ( $r = r_{Sch}$ ) | 1/2 |
| Supermassive black hole | $10^6$ | $3 \times 10^6$ ( $r = r_{Sch}$ ) | 1/2 |

Table 1: Some example of astrophysical objects.

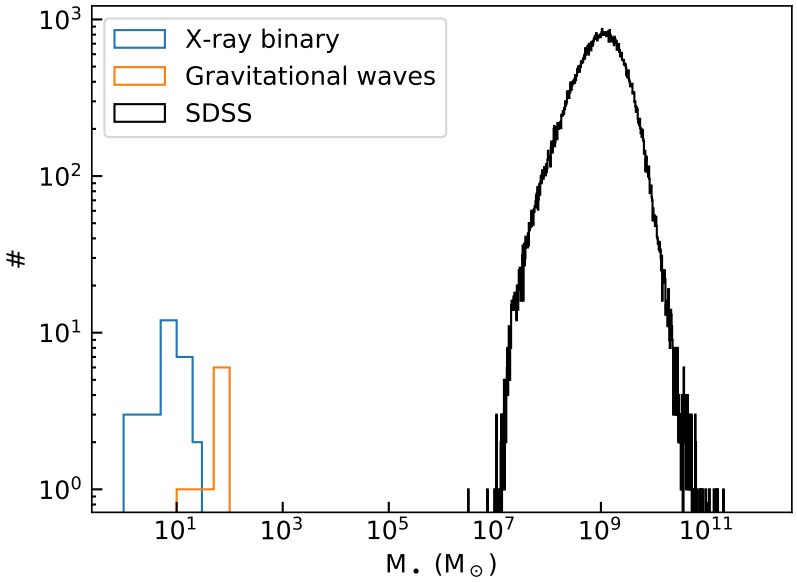


Figure 3: Histogram of the masses of observed BHs. Values are taken from Shen et al., 2011 for supermassive BHs; Xray database for X-ray binaries; and The LIGO Scientific Collaboration and the Virgo Collaboration, 2018 for gravitational wave detected BHs. For the last case, we use the mass of the remnant BH.

been found in the 1970's only. Today, we know hundreds of thousands of BHs, we report in Fig. 3 the (non exhaustive) histogram of BH mass detected using several techniques not discussed here (see §1.3 and §1.4 for the description of two methods). We distinguish three main populations:

1. *Stellar mass BHs* with a mass below 100 $M_\odot$ : They follow the death a supermassive star and, although they are thought to be fairly numerous in our Galaxy (and in galaxies in general), we only know a few tens. They are mostly detected through X-ray binaries but, recently, we started detecting them through gravitational waves (see §1.3).

2. *Intermediate mass BHs* with a mass in between 100 and $10^4\,M_\odot$ : There are thought to exist but, to date, only few *candidates* have been observed (Mezcua, 2017). A promissing method to detect more of them is through gravitational waves with the Large Interferometer Space Antenna (LISA, Amaro-Seoane, 2017) or through TDEs (see §1.4).

3. *Supermassive BHs* with a mass above a few $10^4\,M_\odot$ : They are thought to be present in the center of most galaxies in our Universe (Kormendy and Ho, 2013). As they are very massive and placed in gas-rich regions, they can, at times, accrete some of the surrounding gas (see §1.2.1) and therefore, according to Eq. (4), shine, sometime becoming more luminous than the entire galaxy itself. For this reason they are called active galactic nuclei (AGNs), and are among the most luminous objects in the Universe, powering quasars, galaxies observed even in the very early Universe (Bañados et al., 2018). Several models have been proposed to explain the formation of supermassive BHs (direct collapse, population III stars, runaway collisions of stars; see Volonteri and Bellovary, 2012), however the exact details are still poorly understood.

In this Section, we briefly described the main objects we will study in this Thesis: galaxies and BHs. We also presented some of the most fundamental questions regarding BHs: **What is the initial/current mass function of BHs? Do intermediate mass BHs exist?**

## 1.2 AN EVOLVING UNIVERSE

One of the most important discoveries of the $20^{\text{th}}$ century, both in physics and philosophy, is probably that the Universe is not static as it had long been thought. Instead, Friedmann, 1922 and Lemaître, 1927, solving Einstein's equation of general relativity to obtain the evolution of the metric in an isotropic and homogeneous universe (see Peter and Uzan, 2009), showed theoretically that the Universe is expanding and was formed about 14 billions years ago. The expansion was observationally confirmed shortly after by Hubble, 1929. It has the following consequence: if, today, at $t = t_0 \sim 14\,\text{Gyr}$ , a length (a wavelength, or the distance between two galaxies) is $\lambda_0$, then, at $t < t_0$, this length was shorter by a factor $a \equiv 1/(1+z)$,

where $a$ is the expansion factor and $z$ the redshift, which respectively equal 1 and 0 today, so that:

$$\lambda(t) = a(t) \times \lambda_0 = \frac{\lambda_0}{1 + z(t)}\,. \tag{7}$$

The Friedman-Lemaitre equations allow to compute the relation between $a$, $z$ and $t$ given the following properties, measured with exquisite precision with the satellite *Planck* (Planck Collaboration et al., 2016):

- $H_0 = 67.74\,\mathrm{km\ s^{-1}\,Mpc^{-1}}$ is the current Hubble constant;
- $\Omega_{m,0} = 0.3039$ is the current energy density of matter (dark matter+baryons);
- $\Omega_{b,0} = 0.0486$ is the current energy density of baryons;
- $\Omega_{\Lambda,0} = 0.6911$ is the current energy density of dark energy;
- $\Omega_{r,0} = 10^{-5}$ is the current energy density of relativistic matter;
- $\Omega_{K,0} = 0$ is the current curvature.

Overall, we have a fairly good idea of the global evolution of the Universe, we discuss here the different phases shown in Fig. 4:

1. *Big-bang* at $t = 0$: This corresponds to the birth of the Universe.
2. *Inflation and reheating* from $t \sim 10^{-36}\,\mathrm{s}$ to $10^{-32}\,\mathrm{s}$: The universe undergoes an accelerated expansion driven by some quantum field, which exact nature is still debated. Following this, most of particles of the standard model form.
3. *Recombination* at $t \sim 400\,000\,\mathrm{yr}$: So far, the Universe was so hot that photons were energetic enough to ionize Hydrogen. When the Universe becomes cooler than 3000 K, it is not the case anymore, Hydrogen recombines and becomes neutral. Photons emitted at this time are not energetic enough to re-ionize their surrounding medium, therefore they can travel through cosmic time, and in particular to us, forming the so called Cosmic Microwave Background (CMB). The satellite *Planck* has successfully observed the CMB, footprint of the Universe at the time of recombination, and has shown how homogeneous it was, with relative variations of density/temperature of $\sim 0.01\%$.
4. *Dark ages* from $t \sim 400\,000\,\mathrm{yr}$ to $150\,\mathrm{Myr}$: This period consist on the transition period between the recombination and the formation of the first stars in the Universe.
5. *Galaxy formation and evolution* from $t \sim 150\,\mathrm{Myr}$ to today: It is during this time that BHs and galaxies form and evolve, we get into more details in the following Sections.

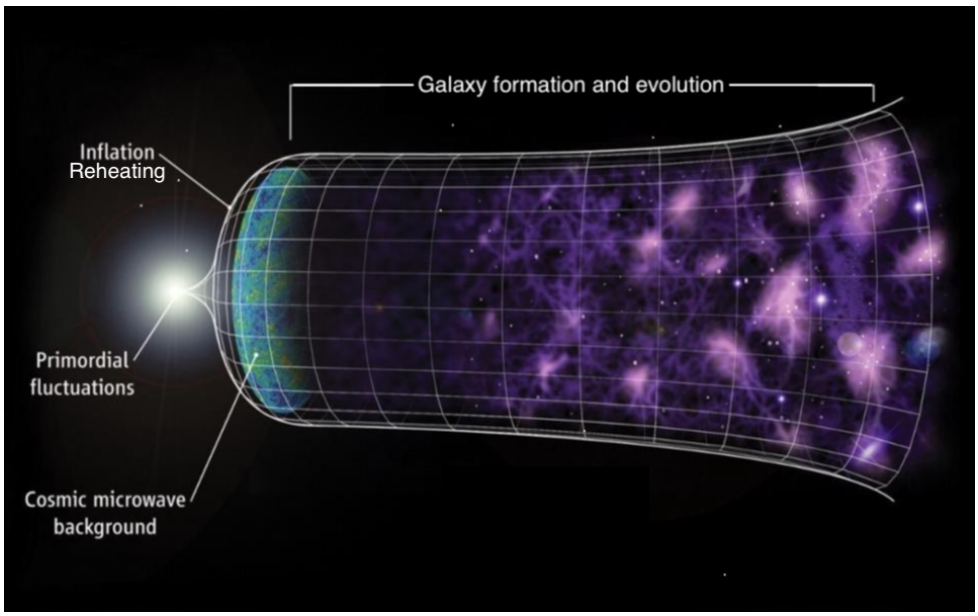


Figure 4: Sketch showing the expansion of the Universe and the different main phases it has been through.

The evolution of the Universe down to the recombination is far from the topic of this Thesis, and we will at best use an evolved–CMB (through the second order Lagrangian perturbation theory, see Buchert, 1989) as initial conditions for our simulations. However, the early life of the Universe composes an active field of research, necessary to understand why the Universe is homogeneous or how most of the particles we know were formed.

### 1.2.1 *Evolution of black holes*

In this Section, we describe how BHs evolve through cosmic time.

**Black hole growth** During the life of a BH, material will fall onto it and be swallowed, naturally increasing its mass. Estimating what is the inflow of mass given properties around the BH is key to understand how it will grow. In this Section we draw the picture of Bondi-Hoyle-Littleton accretion (Bondi and Hoyle, 1944; Bondi, 1952).

Assume a BH, with a mass $M_\bullet$, surrounded by gas with velocity $\mathbf{V_0}$ and density $\rho$. Consider a particle from the flow, with mass $m_\star << M_\bullet$, initially at a distance $r = +\infty$ with an impact parameter $b$, as in Fig. 5. If $b$ is "very large", where "very large" means larger than a threshold $b_{max}$ which will be derived in the following, then this particle will never fall onto the BH. Conversely, if $b < b_{max}$, then this particle will be swallowed. The net mass-flux, $\dot{M}_{acc}$, falling onto the BH is therefore:

$$\dot{M}_{acc} = \pi b_{max}^2 \rho V_0 \,. \tag{8}$$

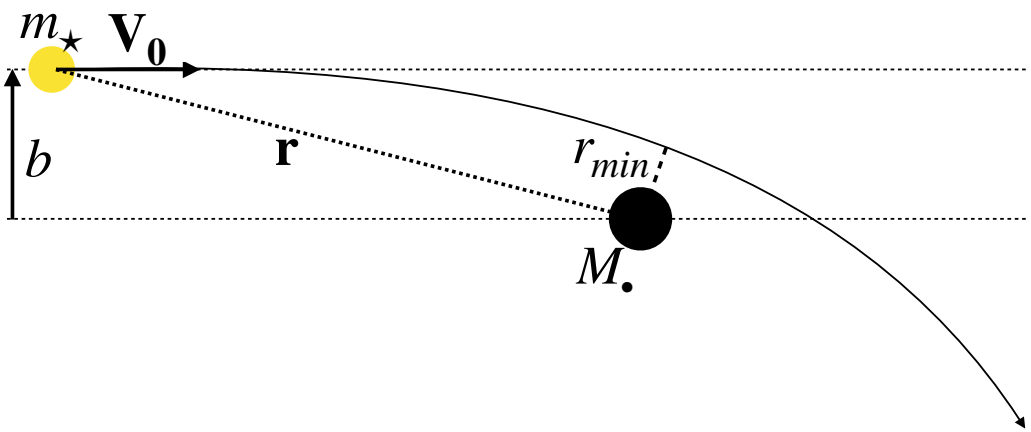


Figure 5: Sketch of a hyperbolic encounter between a particle and a BH.

In Appendix 7, we solve this hyperbolic two-body problem and derive the dynamics of particles pertaining to this problem. Eq. (202) gives the closest distance to the BH, $r_{min}$:

$$r_{min} = \frac{G\,M_\bullet}{V_0^2}\left(-1+\sqrt{1+\frac{b^2V_0^4}{G^2\,M_\bullet{}^2}}\right) \tag{9}$$

$$= r_{def}\left(-1+\sqrt{1+\frac{b^2}{r_{def}^2}}\right), \tag{10}$$

where we have used that $m_\star << M_\bullet$ and introduced the deflection radius, $r_{def} \equiv G\,M_\bullet/V_0^2$. To get a step further and determine the expression of $b_{max}$, we assume that this particle is swallowed by the BH, *i.e.* is accreted, if it is gravitationally bound[3] to the BH at $r_{min}$, considering, at first order, that its speed is $V_0$. This yields:

$$\frac{G\,M_\bullet}{r_{min}} > \frac{1}{2}v_0^2 \tag{11}$$

$$\Leftrightarrow \quad b < b_{max} \equiv 2\sqrt{2}r_{def}\,. \tag{12}$$

Combining Eq. (8) and Eq. (12), we obtain the Bondi-Hoyle-Littleton accretion rate:

$$\dot{M}_{acc} = 8\pi\frac{G^2\,M_\bullet{}^2\rho}{V_0^3} \tag{13}$$

$$= 1\,M_\odot\ \mathrm{yr}^{-1}\left(\frac{M_\bullet}{10^8\,M_\odot}\right)^2\left(\frac{\rho}{100\,\mathrm{amu\,cm}^3}\right)\left(\frac{V_0}{200\,\mathrm{km\ s}^{-1}}\right)^{-3}. \tag{14}$$

A few comments about this equation:

3 Note the swindle here: if the particle comes from infinity, it cannot be gravitationally bound, unless another process makes it lose energy. In practice, this particle is part of a flow where pressure forces, viscosity and shocks have to be taken into account.

- $\dot{M}_{acc} \propto M_\bullet{}^2$, therefore massive BHs can grow more easily, whereas it is harder for low mass BHs to grow. For instance, as the time to double the mass of a BH is about $M_\bullet/\dot{M}_{acc}$, for fiducial value of $\rho = 100 \mathrm{amu\,cm^3}$ and $V_0 = 200\,\mathrm{km\ s^{-1}}$, it takes about $10^8\,\mathrm{yr}$ for a $10^8\,M_\odot$ BH, and 1000 Gyr for a $10^4\,M_\odot$ BH.
- $\dot{M}_{acc} \propto V_0^{-3}$ therefore the dynamics of BHs is extremely important if one want to estimate properly their accretion.

We emphasize that this calculation, albeit simple, is in excellent agreement with numerical simulations of axisymmetric flow of inviscid ideal gas past a gravitating body (Shima et al., 1985). The most important caveat is probably the absence of super(sub)-sonic accretion flow and, in practice, many groups (Dubois et al., 2012) use the following expression:

$$\dot{M}_{acc} = 4\pi \frac{G^2 M_\bullet{}^2 \rho}{\left(V_0^2 + c_s^2\right)^{3/2}}, \tag{15}$$

where $c_s$ is the sound speed arround the BH. Note that this expression still assumes spherical symmetry, no rotation and a constant gas density.

**Black hole feedback** As showed by Eq. (4), a fraction[4] $\epsilon$ of the accreted mass is re-emitted as energy in the galaxy, heating and pushing away the surrounding gas. This process, known as feedback, has dramatic consequences onto galaxies (Silk and Rees, 1998; Choi et al., 2018; Dashyan et al., 2019).

Consider a BH with initial mass $M_{\bullet,0}$ and final mass $M_\bullet \gg M_{\bullet,0}$, we have:

$$\begin{aligned} M_\bullet - M_{\bullet,0} &= \int \dot{M}_\bullet dt && (16)\\ &= \int \dot{M}_{acc}(1-\epsilon) dt && (17)\\ &= M_{acc}(1-\epsilon) && (18)\\ &\sim M_\bullet\,. && (19) \end{aligned}$$

The amount of energy released in the surrounding is:

$$\begin{aligned} \Delta E_\bullet &= \epsilon M_{acc} c^2 && (20)\\ &= \frac{\epsilon}{1-\epsilon} M_\bullet\, c^2\,. && (21) \end{aligned}$$

4 We now use $\epsilon$ instead of $\Xi$. The first notation is usually used by astrophysicists and the second one by theoretical physicists.

This value has to be compared with the total energy needed to unbind all the gas, with mass $M_{gas}$, from a halo, with mass and radius $M_h$ and $R_h$, that is:

$$\Delta E_{gas} = \frac{G M_{gas} M_h}{R_h} \tag{22}$$

$$= M_{gas} \sigma_h^2 , \tag{23}$$

where $\sigma_h$ is the velocity dispersion of the halo, and the equality comes from the Virial Theorem, telling that gravitational energy equals twice the kinetic energy. Combining Eq. (21) and Eq. (23), we have:

$$\frac{\Delta E_\bullet}{\Delta E_{gas}} = \frac{\epsilon}{1-\epsilon} \left( \frac{M_\bullet}{M_{gas}} \right) \left( \frac{c}{\sigma_h} \right)^2 . \tag{24}$$

Due to the $(c/\sigma_h)^2$ factor, this ratio can be very large. For fiducial values $\epsilon = 0.1$, $M_\bullet / M_{gas} = 10^{-3}$ and $c/\sigma_h = 10^3$, we find $10^2$! Consequently, even if a very small fraction of the emitted energy is transferred to the gas, BHs have the capability of completely unbind and affect their host galaxy.

This effect is clear from an observational perspective, with the so called $M_\bullet - \sigma$ relation or, equivalently, the $M_\bullet - M_{bulge}$ relation (see Fig. 6), saying that there is a tight correlation between global quantities, such as velocity dispersion or mass, of galaxies and the mass of their central supermassive BH. We emphasize here that this relation is *not* trivial: the mass (size) of the BH is much lower than the mass (size) of its host galaxies, by orders of magnitude. This counter-intuitive results most likely comes from the tremendous amount of energy released when BHs grow.

### 1.2.2 *Evolution of halos and galaxies*

**Growth of structures** As discussed above, in the early phase of galaxy evolution, following the recombination, the Universe is extremely homogeneous. That is, the overdensity

$$\delta(\mathbf{r}) \equiv \frac{\rho(\mathbf{r}) - \langle \rho \rangle}{\langle \rho \rangle} , \tag{25}$$

where $\rho$ is the density and $\langle . \rangle$ is the spatial-mean, is very small. Therefore, the hydrodynamical equations in a Friedman-Lemaitre universe, expressing the evolution of the density field, can be linearized in $\delta$ to find out that these perturbation grow with time. Consequently, structures, halos and galaxies, form. What happens physically is that small over-dense regions attract, through gravity, under-dense regions, naturally increasing the contrast. We show in Fig. 7 two snapshots of a cosmological simulations at different times: in the early[5]

5 Note that we are far after recombination.

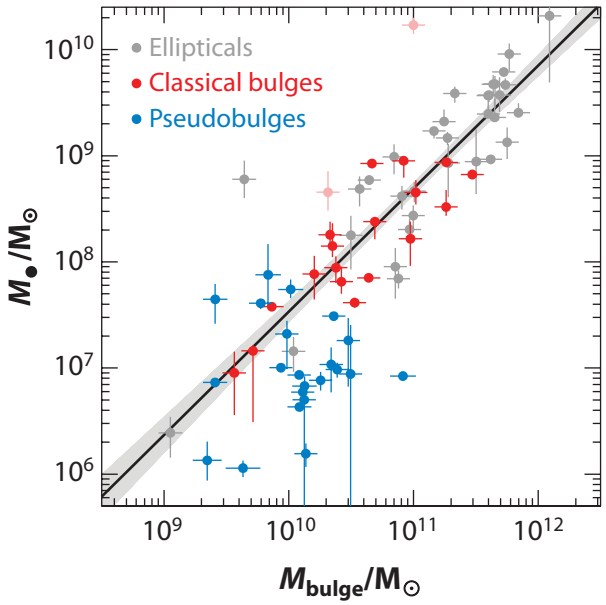


Figure 6: BH mass versus bulge mass relation. Taken from Kormendy and Ho, 2013.

homogeneous universe at $z \sim 30$, and today, at $z = 0$ where halos and galaxies have formed. One can see that, today, the overdensity can be very large, therefore the initial assumption made ($\delta << 1$) is not valid anymore and equations become highly non-linear. In this regime, only numerical simulations, such as the one used to produce Fig. 7, can track the evolution of the density field.

**Galaxy mergers** Another reason explaining the massive use of numerical simulations in the context of galaxy evolution is that galaxies and halos attract each-other, collide, merge to form a final remnant in a highly non-linear way. We show in Fig. 8 a 2D projection of the stellar density of a galaxy at $z \sim 7$, which is undergoing a merger with two other galaxies. These very violent events contribute to build up the mass of galaxies, but also to change their morphology (Toomre, 1977), trigger star formation (Mihos and Hernquist, 1996) and AGN feedback (Di Matteo, Springel, and Hernquist, 2005).

In this Section, we briefly discussed how BHs and structures grow through cosmic time and raised some of the main questions relating BHs and galaxies: **What are the exact effects of feedback of BHs onto galaxy evolution? How do these objects co-evolve?** We also presented galaxy mergers, which might result in BH mergers. Indeed, galaxies might host supermassive BHs, indicated by black bullets in Fig. 8, which could end in the center of the galaxy remnant and merge, emitting gravitational waves we will detect (see §1.3). **How many galaxy pairs result in galaxy mergers? How many galaxy mergers result in BH mergers? What are the properties of BH mergers?** are debated question in Astronomy, and we briefly explored this in this Thesis (see Chapter 3).

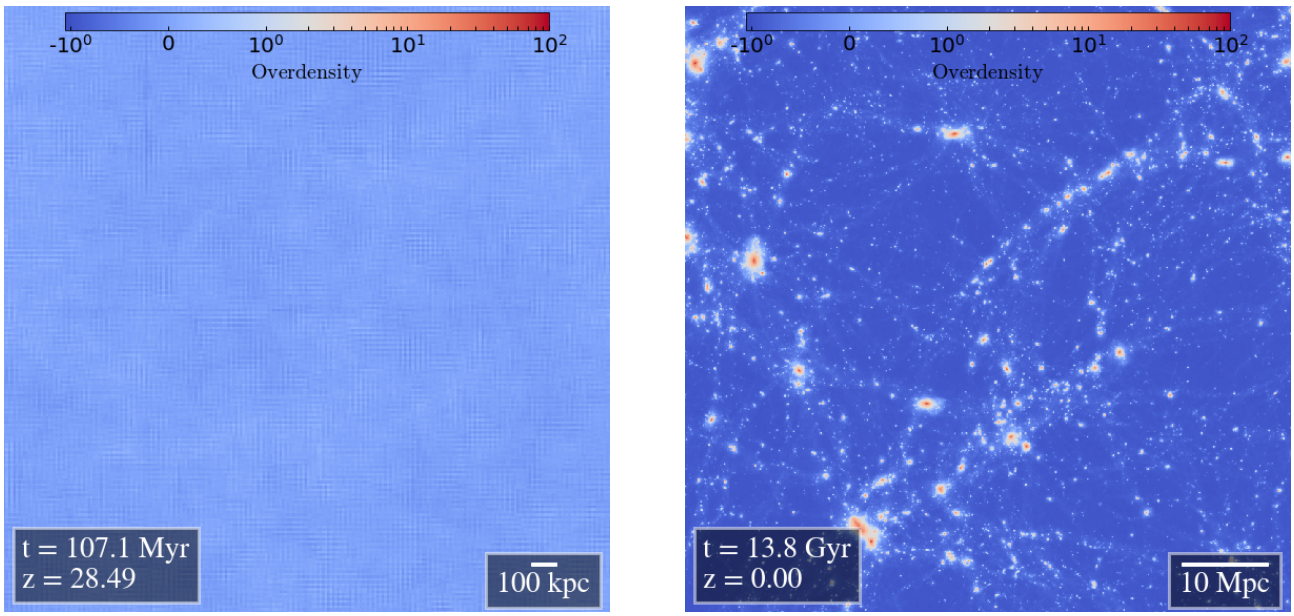


Figure 7: Overdensity as defined by equation Eq. (25), in a simulation, of the early homogeneous universe (left) and today (right).

## 1.3 GRAVITATIONAL WAVES AND LISA

In Einstein's general relativity, objects bend spacetime (see Fig. 9, left) in which they are moving, contrary to the Newtonian formalism, in which gravity is a force. Consequently, when two massive objects orbit around each other, they periodically bend spacetime, producing gravitational radiation that propagates at the speed of light, these are gravitational waves (see Fig. 9, right).

Let us consider two BHs, such that the sum of their masses is $M_b$, separated by a distance $r$ and at a distance $d$ from Earth. After some time, the gravitational waves emitted will cross the Earth and interact with matter, changing the length of objects by a factor (Maggiore, 2008):

$$1 + h \sim 1 + \frac{1}{d}\frac{G^2 M_b^2}{c^4 r} \tag{26}$$

$$\sim 1 + 10^{-20}\,\Xi \left(\frac{M_b}{M_\odot}\right)\left(\frac{d}{\text{Mpc}}\right)^{-1}, \tag{27}$$

where $h$ is the strain and $\Xi$ is the compactness defined in §1.1. For two BHs with a total mass $M_b = M_\odot$, 1 Mpc away from Earth, in the last phase of the merger, *i.e.* separated by $r \sim r_{Sch}$ so that $\Xi \sim 1/2$, we have $h \sim 10^{-20}$. This is the precision required by detectors to detect these gravitational waves.

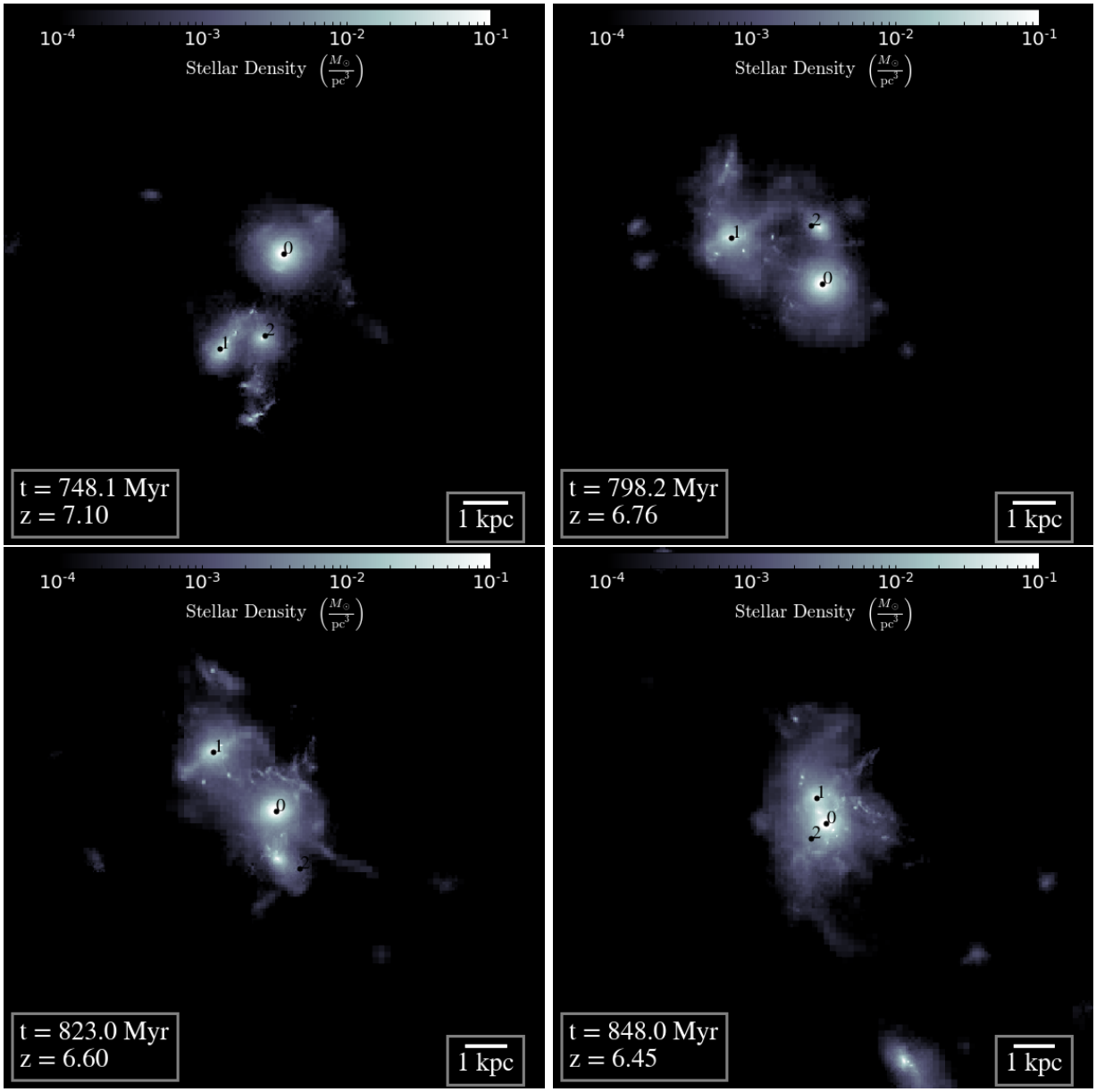


Figure 8: Three galaxies in interaction at different time of mergers in a cosmological simulation.

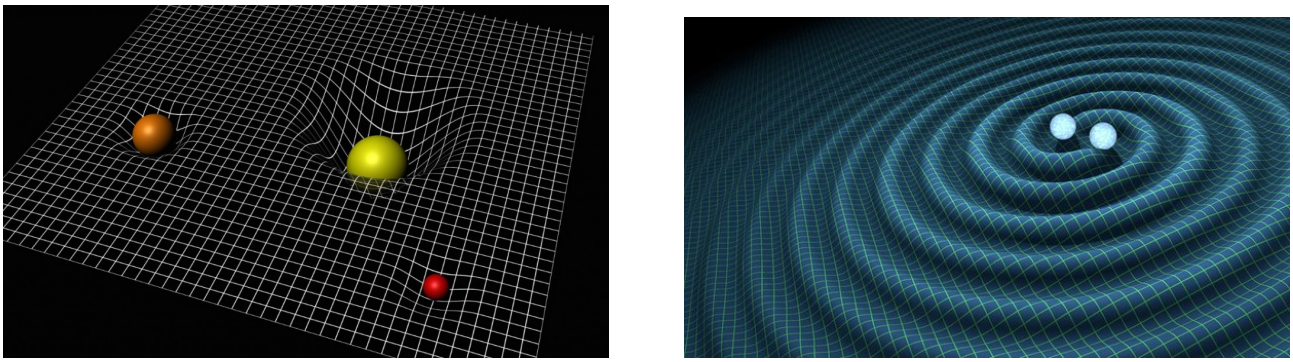

Figure 9: **Left:** Spacetime bent by massive objects. **Right:** Massive binary orbiting around each other, emitting gravitational waves.

### 1.3.1 *Gravitational wave detectors*

The first gravitational wave detectors were designed by Joseph Weber in the 1960's but, while he claimed to have detected them at multiple times (Weber, 1968; Weber, 1969), his results could not be reproduced nor confirmed by his peers.

Today, gravitational wave detectors consist in large scale (from kilo-meter to giga-meter) light interferometers. When gravitational waves pass through the interferometer, they vary the length of one of the two arms by a factor $1 + h$, causing interference fringes to appear and allowing detection (see LIGO Scientific Collaboration et al., 2015 for more details). There exist a few detectors on Earth: GEO 600 in Germany, which is 600 m long, VIRGO in Italy and the two LIGO ones in the US which are about 4 km long (300 effective km as light is reflected). LIGO successfully detected the first gravitational waves signal from a BH merger (Abbott et al., 2016), and both LIGO and VIRGO collaborated to detect the first neutron star merger (The LIGO Scientific Collaboration and the Virgo Collaboration, 2017), opening a new era in multi-messenger astronomy, *i.e.* observations with light and gravitational waves.

Unfortunately, ground based telescopes cannot detect the merger of supermassive BHs. Indeed, their sensitivity is best at frequencies around

$$f_{\text{detector}} \sim \frac{c}{L} \tag{28}$$

$$\sim 600\,\text{Hz}\,\frac{500\,\text{km}}{L}\,, \tag{29}$$

where $L$ is the length of the arms. However, the frequency of gravitational waves emitted during the merger is similar to the Keplerian period, around an object of mass $M_\bullet$, at the Schwarzschild radius, that is:

$$f_{GW} \sim \sqrt{\frac{G\,M_\bullet}{r_{\text{Sch}}^3}} \tag{30}$$

$$\sim 700\,\text{Hz}\,\frac{100\,M_\odot}{M_\bullet} \tag{31}$$

$$\sim 0.07\,\text{Hz}\,\frac{10^6\,M_\odot}{M_\bullet}\,. \tag{32}$$

Consequently, comparing Eq. (29) and Eq. (32), the typical length to detect gravitational waves emitted from $10^6\,M_\odot$ supermassive BHs is millions of km. As it is impossible to build an interferometer of this size on Earth, we will have to go to space. This is the LISA project (Amaro-Seoane, 2017) which has been selected by ESA, with NASA as a minor partner. LISA consists of three satellites forming a triangle with side 2.5 millions of km. Challenging technical development have to be carried out before LISA is launched, hopefully in the

2030's, but the first sensitivity tests with only one satellite, LISA *pathfinder* in 2015 were better than expected and the mission was a success (Armano et al., 2018).

### 1.3.2 *Formation of a binary black hole*

In the previous Sections, we presented how gravitational waves are emitted by binaries, and how we could possibly detect them. However, as we can only detect these gravitational waves in the last phase of the merger, when BHs are close enough, one can wonder **how can supermassive BH binaries form? and how these binaries reach few Schwarzschild radii separation?**

In the following paragraphs, we detail the different phases of a binary, with a primary of mass $M_\bullet$, a mass ratio $q < 1$, a total mass $M_b \equiv (1+q)\,M_\bullet$, a reduced mass $\mu \equiv q\ M_\bullet\ /\ (1+q)$, and separated by a distance $r$. In that case the energy of the binary is $E = -G\,\mu M_b/r$.

**Gravitational wave regime** A binary emitting gravitational waves shrinks because the waves carry energy and momentum. Even if gravitational waves are strongest when the binary has a small separation, they are emitted at all radii (see Eq. (27)). Assuming circular orbits, Peters, 1964 shows that the binary would shrink, due to the emission of gravitational waves, in a time

$$t_{GW} = \frac{5c^5 r^4}{256\,G^3 \mu M_b^2}\,. \tag{33}$$

From this, we can estimate what must be the initial separation, $r_{GW}$, such as the binary merges, through gravitational waves, within a time $\tau$. This yields:

$$r_{GW} = 1\,\mathrm{mpc}\left(\frac{\tau}{10\,\mathrm{Gyr}}\right)^{1/4}\left(\frac{M_b}{10^6\,M_\odot}\right)^{3/4}\left(\frac{4q}{(1+q)^2}\right)^{1/4} \tag{34}$$

Consequently, an equal mass ratio binary ($q = 1$) of two supermassive BHs with masses $5\times 10^5\,M_\odot$ merges, through gravitational waves, within the age of the Universe ($\tau \sim 10\,\mathrm{Gyr}$), if the initial separation is about 1 mpc. As a reminder, two supermassive BHs are initially separated by tens to hundreds of kpc and sit in the center of different galaxies (see §1.2.2 and Fig. 8), therefore there must be processes other than gravitational waves emission allowing to bridge these 8 orders of magnitude in separation.

**Stellar scattering** When two BHs are close enough ("close" to be defined) so they are embedded in a dense stellar environment, single stars can be ejected through gravitational

slingshot, as shown in Fig. 10 (left). In that case, these stars leave the system with (kinetic) energy, resulting in the shrinking of the binary.

If we consider the interaction of one star orbiting the binary, with mass $m_\star << q\,M_\bullet < M_\bullet$, at first order, we can write the variation of energy due to the scattering of the star as:

$$\Delta E = -C|E|\frac{m_\star}{M_b}\,, \tag{35}$$

where C is, *a priori*, a complex function of $\sigma$, $a$ etc... However, as shown by Monte Carlo scattering experiments (Quinlan, 1996; Sesana, Haardt, and Madau, 2006), C appears to be close to unity so we will assume $C = 1$ in the following. The binary effectively shrink if the star leaves the system, that is, its speed is larger than the escape velocity, which, at first order, equals the velocity dispersion $\sigma$. This yields:

$$-\Delta E > m_\star \sigma^2 \tag{36}$$

$$\Leftrightarrow \quad r < r_h \equiv \frac{G\,\mu}{\sigma^2} = 0.1\,\mathrm{pc}\left(\frac{M_b}{10^6\,M_\odot}\right)\left(\frac{\sigma}{200\,\mathrm{km\ s^{-1}}}\right)^{-2} \tag{37}$$

where we introduce the hardening radius $r_h$. For an equal mass ratio ($q = 1$) supermassive BH binary with masses of $5 \times 10^5\,M_\odot$ embedded in a Milky-Way like environment ($\sigma \sim 200\,\mathrm{km\ s^{-1}}$), stellar scattering becomes effectively efficient when the BHs are separated by 0.1 pc. Note that we "gained" 2 orders of magnitude compared with the gravitational waves regime, however, we still have to bridge 6 orders of magnitude... In addition, as more and more interactions occur to shrink the binary, stars are ejected and, at some point, these interactions become very rare and the binary stalls. Consequently, there must be a process which "refills" the surrounding with stars, known as the loss cone refilling problem. This refilling depends on the geometry of the nucleus but is still poorly understood (Vasiliev, Antonini, and Merritt, 2014).

**Gas torques** In addition to stars, BHs could be surrounded by gas (Fig. 10, right). As the binary axis (black line passing by the two BHs) may be miss-aligned with the main axis of the nucleus (other black line), negative torques can shrink the binary. Depending on the configuration, gas can efficiently – or not – drive BHs inward (del Valle and Escala, 2012; Amaro-Seoane et al., 2016). However, recent simulations including accretion and AGNs (del Valle and Volonteri, 2018) show that, whatever the configuration, feedback can open a large enough cavity so that torques become inefficient to shrink the binary. This process, as the previous one, is still an active field of research. It is interesting to note, though, that they occur at similar scales, smaller than 1 pc.

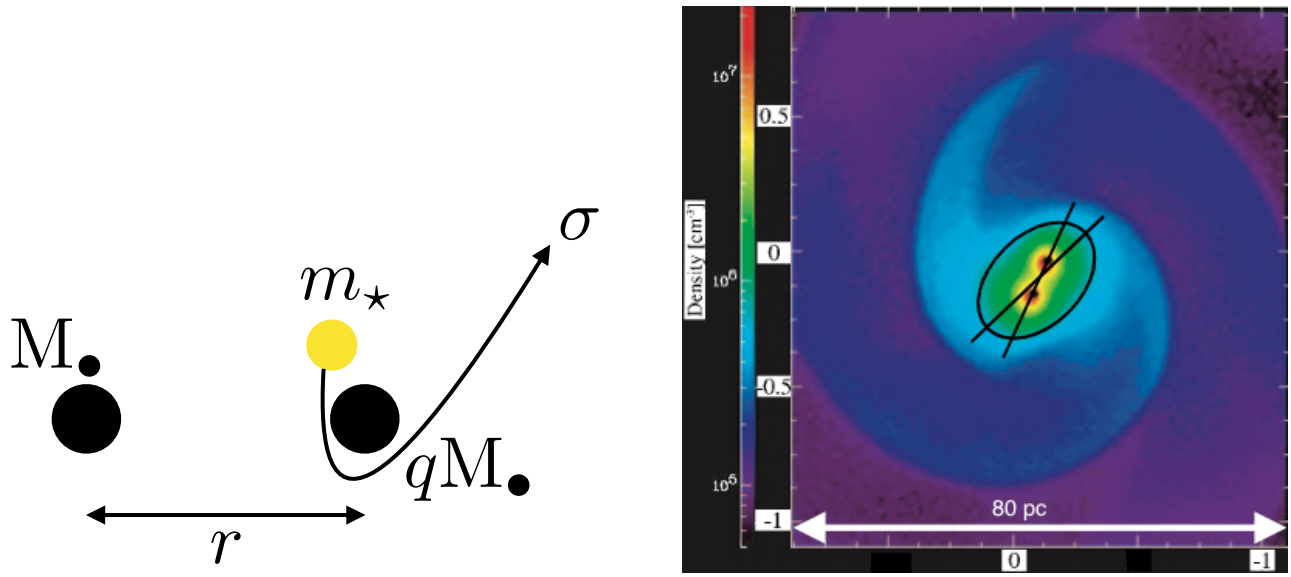


Figure 10: **Left:** Star being scattered by a massive BH binary. **Right:** 2D gas density projection showing two BHs embedded in a gas nucleus. Taken from Escala et al., 2005.

**Dynamical friction** This process will be extensively studied in Chapters 2 and 3. We just mention here that, if the secondary BH is massive enough, dynamical friction can efficiently drive the distance between BHs from tens/hundreds of kpc to pc, bridging almost from galaxy mergers to the formation of a bound binary at $\sim$ pc scale.

To conclude this Section, we recall the main questions discussed: **How can we detect supermassive BHs? How do binaries shrink from tens/hundreds of kpc separation following galaxy mergers to mpc separation, where the gravitational waves emission becomes efficient?** We also briefly introduced the last-parsec problem, saying that the processes driving BHs from pc to mpc (stellar scattering and gas torques) are still poorly understood (Souza Lima et al., 2016; Goicovic et al., 2016). From an observational perspective, the tightest binary candidate currently known is separated by about 7 pc (Rodriguez et al., 2006): **is there a still poorly understood process which quickly drives BHs inward, causing the number of low separation BHs to be small? or is it just an observational issue that close pairs cannot be disentangled?** The reason of this observational result is still debated.

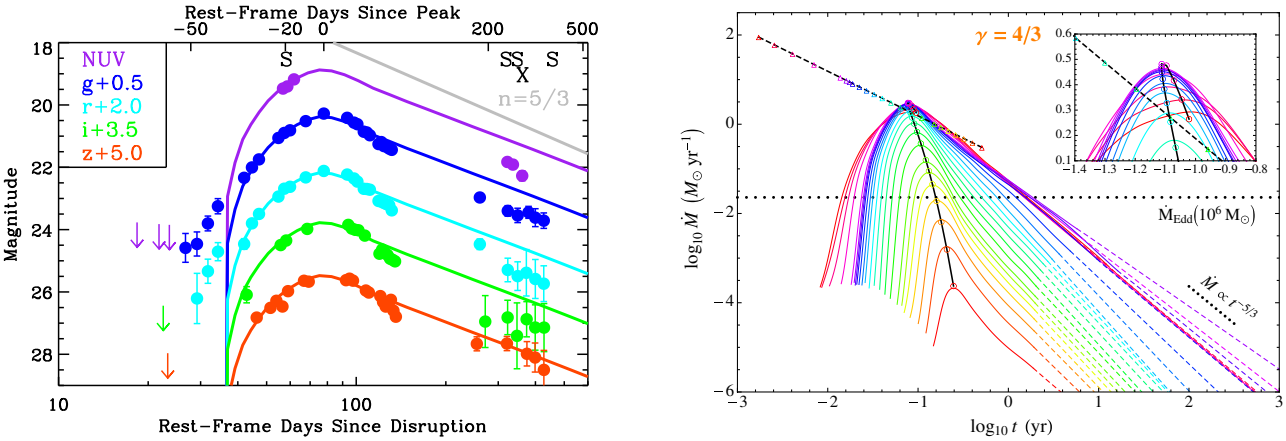


Figure 11: **Left:** Lighcurves at different wavelength of a TDE. Taken from Gezari et al., 2012. **Right:** Accretion rate as a function of time onto the BH from a numerical simulation. Taken from Guillochon and Ramirez-Ruiz, 2013.

## 1.4 TIDAL DISRUPTION EVENTS AND TRANSIENT SURVEYS

### 1.4.1 *Tidal disruption events as a mean to detect black holes*

When a star, with mass $m_\star$ and radius $r_\star$, passes at distance $r$ from a BH of mass $M_\bullet$, the star is subject to tidal forces in the field of the BH:

$$|\frac{\partial \mathbf{F}}{\partial r}|r_\star \sim \frac{G\,M_\bullet\,m_\star}{r^2}\frac{r_\star}{r}\,, \tag{38}$$

where F is the gravitational force exerted by the BH onto the star. If these tidal forces are stronger than the self–gravity of the star:

$$\frac{G\,M_\bullet\,m_\star}{r^2}\frac{r_\star}{r} > \frac{G\,m_\star^2}{r_\star^2} \tag{39}$$

$$\Leftrightarrow \quad r < r_t \equiv r_\star\left(\frac{M_\bullet}{m_\star}\right)^{1/3}\,, \tag{40}$$

where we define the TDE radius $r_t$, then the star is disrupted. If the disruption occurs outside the Schwarzschild radius:

$$r_t > r_s \tag{41}$$

$$\Leftrightarrow \quad M_\bullet < M_t \equiv \sqrt{\frac{r_\star^3 c^6}{G^3 m_\star}} = 3\times10^8\,M_\odot\left(\frac{r_\star}{R_\odot}\right)^{3/2}\left(\frac{m_\star}{M_\odot}\right)^{-1/2}\,, \tag{42}$$

then the disruption of the star occurs before it penetrates the Schwarzschild radius, and is not swallowed whole but is disrupted. This phenomenon is known as a TDE (Hills, 1975).

Under these conditions, a fraction of the star sinks onto the BH and is heated as it sinks to the BH and converts gravitational energy to internal energy, sourcing a bright flare (Rees, 1988) which we can observe. We show in Fig. 11 observational light-curves at different wavelengths (left) and the theoretical accretion rate onto a BH computed using numerical simulations (right). In both cases, a similar pattern is visible: there is a rapid rise of the accretion rate (and therefore of the luminosity) and, following the peak, a decay. While the early phases are highly non linear as modifications of the structure of the star in a relativistic regime must be evolved (Dai et al., 2018), a simple but elegant calculation can explain a -5/3 decay (Phinney, 1989): following the disruption of a star by a BH of mass $M_\bullet$, gas will shock and exchange energy so that the energy distribution $dM/de$ is fairly constant[6]. A gas patch at distance $r$ from the BH has an energy per unit mass $e = -G\,M_\bullet/r$, and a period $T = (G\,M_\bullet/r^3)^{1/2}$, therefore:

$$\frac{dM}{dT} = \frac{dM}{de}\frac{de}{dr}\frac{dr}{dT} \tag{43}$$

$$= \frac{dM}{de}\frac{1}{3}(G\,M_\bullet)^{2/3}\,T^{-5/3}\,. \tag{44}$$

Note the fairly good agreement with observations and numerical simulations (see Fig. 11) given the simplicity of the calculation.

More detailed models (Bogdanović et al., 2004; Guillochon and Ramirez-Ruiz, 2013) including the spin of the BH, but also properties of the disrupted star such as its mass, radius, density profile, initial eccentricity etc... show that the accretion at peak[7] can be written as (Eq. (A1) from Guillochon and Ramirez-Ruiz, 2013):

$$\dot{M}_{\rm peak} \sim 1\,M_\odot\ {\rm yr}^{-1}\left(\frac{M_\bullet}{10^6\,M_\odot}\right)^{-1/2}\left(\frac{m_\star}{M_\odot}\right)^{2}\left(\frac{r_\star}{R_\odot}\right)^{-3/2}\,. \tag{45}$$

All this shows that, although degenerate, the information about the physical properties of the system (orbit of the star, density profile of the star, mass of the BH, spin of the BH etc...) is encoded in the the lightcurve (Bogdanović, Cheng, and Amaro-Seoane, 2014; Mockler, Guillochon, and Ramirez-Ruiz, 2019). Using detailed models, we are now able to fit real observations to infer the mass of BHs, for instance, the lightcurves in Fig. 11 (left) are well fitted by models in which the mass of the BH is about 2 millions solar masses. In addition, as shown by Eq. (45), the accretion following a TDE, contrary to accretion of gas in a homogeneous medium (see Eq. (14)), scales as the inverse root of the mass of the BH, so the lighter the BH the easier it should be to detect TDEs. This suggests that TDEs are a promising method to detect intermediate mass BHs and, in fact, one of the lightest BH ever observed (a few $10^4\,M_\odot$) has been detected through a TDE (Lin et al., 2018).

6 This assumption is not verified in simulations of partial and relativistic disruptions.

7 Assuming a polytropic index of 5/3 for the star and an impact parameter $\beta = r_t/r_p > 1$, where $r_p$ is the pericentric distance of the star.

To summarize, TDEs are transient events, lasting from days to months depending on the specific orbital/stellar parameters, and with luminosity decaying as a power law. Therefore, transient surveys, observing the same patch of sky regularly, and covering a large area, are ideal for discovering and studying TDEs.

A significant fraction of the luminosity arising from a TDE falls in the soft X–rays and in optical/UV. In principle, X–rays represent a "cleaner" probe, since the X–ray luminosity of galaxies (integrated X–ray binary emission) is significantly less than the typical X–ray luminosity of TDEs, while in optical/UV, contribution from the galaxy light and the presence of dust can hamper detection. However, because of atmospheric absorption X–ray observations are not possible from the ground, and at the current time only relatively shallow observations with ROSAT (Voges et al., 1999) cover a large area with the repeated observations needed to detect transients, while XMM–Newton or CHANDRA can contribute through pointed observations (*e.g.* Maksym, Ulmer, and Eracleous, 2010). Transient optical/UV surveys have been the alternative source of TDE candidates and events (SDSS – van Velzen et al., 2011; Palomar Transient Factory – Law et al., 2009; Zwicky Transient Facility – Bellm et al., 2019). Note that some optically/UV detected TDEs are not observed in X-rays, Dai et al., 2018 suggested that the explanation is the increase of the observed ratio of optical to X–ray fluxes with increasing inclination angle. However, there is still no clear consensus about this (Wheeler et al., 2019).

We are now entering an era of large transient surveys, such as eROSITA (Merloni et al., 2012) in the X–rays or the Large Synoptic Survey Telescope (LSST, van Velzen et al., 2011) in the optical/UV, both having much higher sensitivity than current surveys, therefore the statistics on TDEs and their hosts will increase significantly in the near future, allowing for better characterization and comparison with theoretical models.

### 1.4.2 *Tidal disruption events to grow black holes*

In the previous Section, we considered TDEs as single events and assumed that a star was on a particular orbit so it is disrupted. In practice, an information one may want to know is **how frequently stars get close enough to BHs to be disrupted?** This has important consequences, as these stars could directly feed BHs, providing an additional source of material to grow.

From an observational perspective, the number of observed TDEs is still low (90 candidates today on the TDE database), and reliable statistics are hard to produce. A commonly used value is $10^{-4}$ event per galaxy per year (Syer and Ulmer, 1999; Wang and Merritt, 2004; Milosavljević, Merritt, and Ho, 2006; Stone and Metzger, 2016; Auchettl, Ramirez-Ruiz, and Guillochon, 2018) but could possibly depend on the type of galaxy (Law-Smith et al., 2017; Tadhunter et al., 2017; Graur et al., 2018) reaching values as high as $10^{-1}\mathrm{gal}^{-1}\,\mathrm{yr}^{-1}$.

From a theoretical point of view, the first calculations on rates were made by Lightman and Shapiro, 1977 who introduced the loss-cone theory, that we will detail in §4.1, and significant amount of work has been done since then (Syer and Ulmer, 1999; Wang and Merritt, 2004; Chen et al., 2009; Amaro-Seoane, Miller, and Kennedy, 2012; Zhong, Berczik, and Spurzem, 2014; Stone and Metzger, 2016; Stone and van Velzen, 2016; Alexander and Bar-Or, 2017), using either analytical techniques or N-body simulations, with results close to the mean observed TDE rate, but with large uncertainties.

In this Section we broadly described TDEs, explaining physically what they are and how they could be used to study BHs. We also pinpointed a debated question regarding TDEs we deepened in this Thesis (see Chapter 4): **What is the number of events per year per galaxy? How do these event depend on galaxy properties?**

# 2

# DYNAMICAL FRICTION

In this Chapter we detail the process of dynamical friction, which drives the dynamics of BHs from kpc to pc scales. We begin by deriving the analytical formulation for dynamical friction, then we discuss the different effects of dynamical friction. Finally, we present how dynamical friction, a crucial element for BH dynamics, can be included in numerical simulations.

This Chapter is based on the following papers:

1. Pfister et al., 2017
2. Pfister et al., 2019a

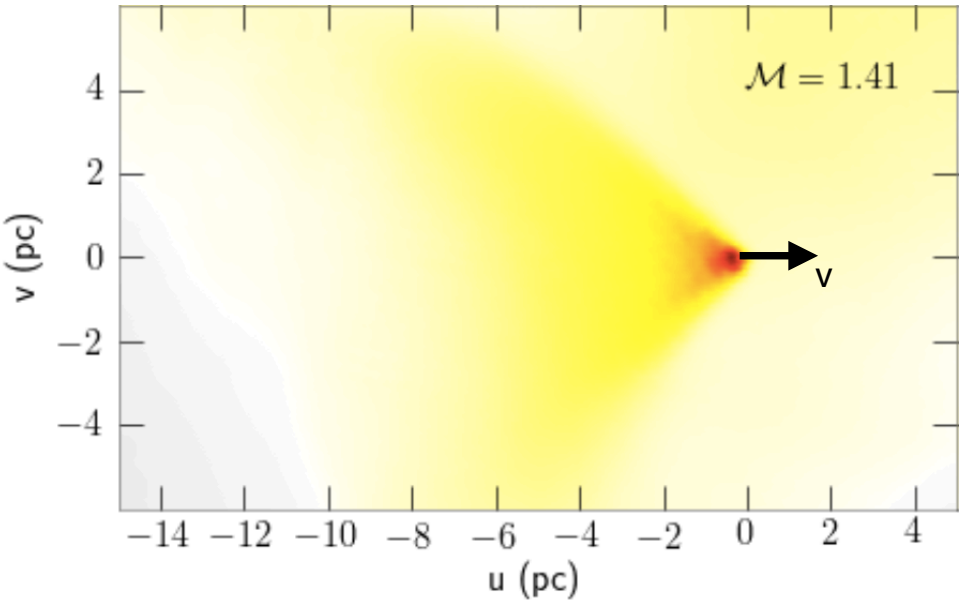


Figure 12: 2D projection of gas density of a simulation of a BH moving in a homogeneous medium. The overdensity behind the BH is pulling it backward: this is dynamical friction. Taken from Chapon, Mayer, and Teyssier, 2013.

## 2.1 WHAT IS DYNAMICAL FRICTION?

Dynamical friction has been theoretised by Chandrasekhar, 1943, and we shall detail the analytical calculation later in this Section, but it can be understood as following: consider a massive object (a BH, a globular cluster, a galaxy) moving in a homogeneous background, as in Fig. 12. As this object moves through this homogeneous medium, it attracts material, creating an over-density just behind it (see Fig. 12). This overdensity, at some point, will become massive enough to induce a back-reaction force, which will slow down the massive perturber: this is dynamical friction.

To get an analytical expression for dynamical friction (Chandrasekhar, 1943; Binney and Tremaine, 1987), let us consider a massive perturber, with a mass $M_\bullet$ and velocity $\mathbf{v}_\bullet$, moving in a homogeneous medium composed with particles of masses $m_\star$. Consider one particle from the surrounding, with initial impact parameter $b$ and velocity $\mathbf{v}_\star$ so that the initial velocity of the star with respect to the perturber is $\mathbf{V}$, as in Fig. 13. The variation of velocity of the perturber is derived in Appendix 7 (Eq. (213)) and equals:

$$\Delta\mathbf{v}_\bullet = \left[1 + \frac{b^2V^4}{G^2(M_\bullet + m_\star)^2}\right]^{-1} \frac{2m_\star V}{M_\bullet + m_\star}\left(\frac{bV^2}{G(M_\bullet + m_\star)}\mathbf{e_r} + \mathbf{e_z}\right), \tag{46}$$

If we consider that all particles in the medium have the same velocity $\mathbf{v}_\star$, taking into account all stars in the ring $[b, b + db]$, the $\mathbf{e_r}$ terms vanish whereas the $\mathbf{e_z}$ terms sum-up: the net variation of velocity is along the direction of $\mathbf{V}$. Note that, if the perturber moves

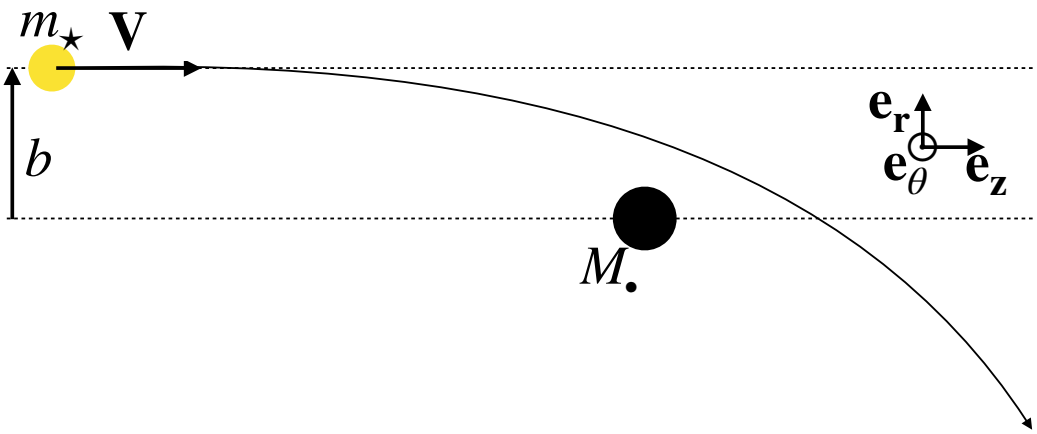


Figure 13: Sketch of a hyperbolic encounter, geometry used is cylindrical. Basis used is different than in Appendix 7.

with the medium ($V = 0$), its dynamics is not modified. As the perturber moves at velocity $\mathbf{V}$ with respect to stars, the encounter rate with impact parameters in $[b, b + db]$ is:

$$V \times 2\pi b db. \tag{47}$$

In practice, however, all particles do not move at the same velocity, the fraction of particles moving with a velocity in $[\mathbf{v}_\star, \mathbf{v}_\star + d\mathbf{v}_\star]$ is given by $f(\mathbf{v}_\star)d\mathbf{v}_\star$, where $f$ is the distribution function, so that the rate at which the perturber encounters particles that have velocities in $[\mathbf{v}_\star, \mathbf{v}_\star + d\mathbf{v}_\star]$ and impact parameters in $[b, b + db]$ is:

$$V \times 2\pi b db \times f(\mathbf{v}_\star)d\mathbf{v}_\star\,. \tag{48}$$

To get the rate at which the velocity of the perturber vary, $d\mathbf{v}_\bullet/dt$ , one should sum the contribution of all particles, that is performing the integral onto $b$ and $\mathbf{v}_\star$. The impact parameter range to consider should be in $[0, \infty]$, however, in real astrophysical systems,

the size of the surrounding medium has a finite size $b_{max}$[1], and one should only consider particles with $b < b_{max}$, this yields:

$$\frac{d\mathbf{v}_\bullet}{dt} = \int_{\mathbf{v}_\star} f(\mathbf{v}_\star) V d\mathbf{v}_\star \int_{b=0}^{b_{max}} 2\pi db \left[1 + \frac{b^2 V^4}{G^2 (M_\bullet + m_\star)^2}\right]^{-1} \frac{2m_\star \mathbf{V}}{M_\bullet + m_\star} \tag{49}$$

$$= 2\pi G^2 m_\star (M_\bullet + m_\star) \int_{\mathbf{v}_\star} f(\mathbf{v}_\star) d\mathbf{v}_\star \ln\left[1 + \left(\frac{b_{max} V^2}{G(M_\bullet + m_\star)}\right)^2\right] \frac{\mathbf{v}_\star - \mathbf{v}_\bullet}{V^3} \tag{50}$$

$$= -2\pi G^2 m_\star (M_\bullet + m_\star) \int_{\mathbf{u}} \tilde{f}(\mathbf{u}) d\mathbf{u} \ln\left[1 + \left(\frac{b_{max} V^2}{G(M_\bullet + m_\star)}\right)^2\right] \frac{\mathbf{v}_\bullet - \mathbf{v}_\star}{V^3} \tag{51}$$

$$= -2\pi G^2 m_\star (M_\bullet + m_\star) \int_{\mathbf{u}} \tilde{f}(\mathbf{u}) d\mathbf{u} \ln\left[1 + \left(\frac{b_{max} |\mathbf{v} - \mathbf{u}|^2}{G(M_\bullet + m_\star)}\right)^2\right] \frac{\mathbf{v} - \mathbf{u}}{|\mathbf{v} - \mathbf{u}|^3}, \tag{52}$$

where where $\langle . \rangle$ denote the spatial mean, $\mathbf{u} \equiv \mathbf{v}_\star - \langle \mathbf{v}_\star \rangle$ is the relative velocity of stars with respect to the background, $\mathbf{v} \equiv \mathbf{v}_\bullet - \langle \mathbf{v}_\star \rangle$ the relative velocity of the perturber with respect to the background and $\tilde{f}$ the distribution function of particles around the mean. Following Chandrasekhar, 1943, as:

- $b_{max} v / (G(M_\bullet + m_\star))(1 \pm u/v)^2$ is, most of the time in astrophysical systems, much larger than 1;
- $\mathbf{u}$ is usually isotropic, that is $\tilde{f}(\mathbf{u}) = \tilde{f}(u)$;
- $m_\star << M_\bullet$ as the perturber is massive with respect to the surrounding;

one can show that (Eq. (25) and Eq. (30) from Chandrasekhar, 1943):

$$\frac{d\mathbf{v}_\bullet}{dt} = -4\pi G^2 m_\star M_\bullet \frac{\mathbf{v}}{v^3} \int_{u=0}^{\infty} 4\pi u^2 \tilde{f}(u) \mathcal{H}(v, u) du \tag{53}$$

with:

$$\mathcal{H}(v, u) = \begin{cases} \ln\left(\frac{b_{max}(v^2 - u^2)}{G M_\bullet}\right) & \text{if } u < v \\ \ln\left(\frac{u+v}{u-v}\right) - 2\frac{v}{u} & \text{if } u > v. \end{cases} \tag{54}$$

1 Note that, although physically meaningful, the cutoff is needed as the integral on b diverges at infinity.

$\ln(1-(u/v)^2)$ terms for $u < v$ are usually dropped (second order $u/v$ correction), leading to:

$$\begin{aligned}\frac{d\mathbf{v}_\bullet}{dt} &= -4\pi G^2 m_\star M_\bullet \frac{\mathbf{v}}{v^3}\left\{\ln\left(\frac{b_{max}v^2}{G\,M_\bullet}\right)\int_{u=0}^{v} 4\pi u^2 \tilde{f}(u)du + \right. \qquad (55)\\ &\quad \left.\int_{u=v}^{\infty} 4\pi u^2 \tilde{f}(u)\left[\ln\left(\frac{u+v}{u-v}\right)-2\frac{v}{u}\right]du\right\}\\ &= -4\pi G^2 M_\bullet \frac{\mathbf{v}}{v^3}\left\{\ln(\Lambda)\, m_\star n_\star(<v) + \mathcal{F}(v,\tilde{f})\right\} \qquad (56)\end{aligned}$$

where we introduce the Coulomb logarithm:

$$\ln(\Lambda) = \ln\left(\frac{b_{max}v^2}{G\,M_\bullet}\right), \qquad (57)$$

the number of particles moving slower than the perturber in the frame of the background $n_\star(<v)$, and:

$$\mathcal{F}(v,\tilde{f}) = m_\star \int_{u=v}^{\infty} 4\pi u^2 \tilde{f}(u)\left[\ln\left(\frac{u+v}{u-v}\right)-2\frac{v}{u}\right]du\,. \qquad (58)$$

Following this long, but straightforward, calculation, we make a few comments about the final expression obtained:

- $d\mathbf{v}_\bullet/dt \propto \mathbf{v}$ therefore dynamical friction tends to make the perturber to move at the same velocity as the background, and vanishes when velocities become equal.
- $d\mathbf{v}_\bullet/dt \propto M_\bullet$ therefore dynamical friction is more effective on massive objects.
- The first term in the braces is proportional to $m_\star n_\star(<v) = \rho_\star(<v)$, where $\rho_\star(<v)$ is the density of particles moving slower than the perturber. Therefore, for two perturbers moving with the same velocity, the denser the medium the stronger dynamical friction.
- Although we had to introduce the size of the system, $b_{max}$, the final result depends on its value only logarithmically.

We found that the force slowing the perturber down is due to the cumulative effects of hyperbolic encounters, however, as mentioned at the beginning of this Section, dynamical friction can also be understood as caused by the lag behind the perturber. An issue with our calculation is that we did not consider the effect of the perturber onto the medium, which therefore unphysically remains homogeneous and isotropic. When the reaction of the medium is taken into account (Weinberg, 1986; Colpi and Pallavicini, 1998), this allows[2]

2 Assuming an isothermal sphere at equilibrium, *i.e.* with Maxwellian velocity dispersion.

to compute the overdensity around the perturber. If the mean density is $\rho_0$ with velocity dispersion $\sigma$, a perturber with mass $M_\bullet$ moving at $\mathbf{v}$ with respect to the background, creates, at position $\mathbf{r}$ from the perturber, an overdensity:

$$\delta\rho(\mathbf{r}) = \rho_0 \frac{\frac{G\,M_\bullet}{\sigma^2}}{r}\left[\mathrm{erf}\left(-\frac{\mathbf{v}\cdot\mathbf{r}}{\sqrt{2}\sigma r}\right)+1\right]\exp\left[\left(\frac{\mathbf{v}\cdot\mathbf{r}}{\sqrt{2}\sigma r}\right)^2-\left(\frac{v}{\sqrt{2}\sigma}\right)^2\right]. \tag{59}$$

From this, we can estimate the force $\delta F$ caused by matter between $r$ and $r+\delta r$ as:

$$|\delta F| \sim \int_r^{r+\delta r} \frac{G\,\rho(r')\,M_\bullet}{r'^2} 4\pi r'^2 dr' \tag{60}$$

$$\sim 4\pi G\,M_\bullet\,\rho_0 \frac{G\,M_\bullet}{\sigma^2}\ln(1+\frac{\delta r}{r})\,. \tag{61}$$

Therefore, most of dynamical friction is sourced by material close to the perturber and, in particular, as the only scale-length in the last expression is the influence radius of the perturber $r_{inf} \equiv G\,M_\bullet/\sigma^2$, most of the dynamical friction is sourced by material closer than $r_{inf}$.

In this Section, we neglected self–interactions between particles causing dynamical friction, this means we considered that the perturber moves in a collisionless system. When self–interactions become important, *e.g.* for a gaseous system, the system is collisional and more complex physics is involved (Ostriker, 1999). In the case of a gaseous background, one also have to consider that BHs can accrete and radiate, which affects the surrounding. Park and Bogdanović, 2017 using numerical simulations, and Gruzinov, Levin, and Matzner, 2019 using an analytical treatment, both found that, when AGN feedback is included, the wake lagging BHs can be disrupted rendering dynamical friction inefficient, and in some situations even leads to "dynamical propulsion". We do not consider this in this Thesis, although this process may be important in pairing BHs. In the following Sections, we study the effect of dynamical friction in driving BHs in the center of galaxies, where they can form a binary, and we will see how dynamical friction can be implemented in numerical simulations to better track the dynamics of BHs.

## 2.2 DYNAMICAL FRICTION TO FORM BLACK HOLE BINARIES

In this Section, we study the dynamics of BHs and detail the effects of dynamical friction using a zoomed simulation of a galaxy merger.

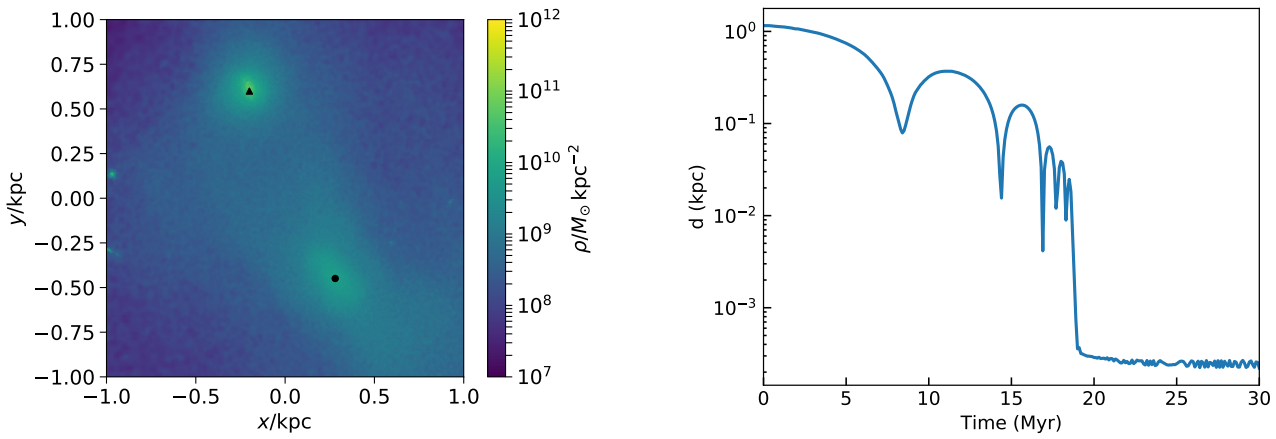


Figure 14: **Left:** 2D projection of stellar density of the initial conditions used for our simulation. The black dot is BH1 whereas the black triangle is BH2. **Right:** Distance between the two BHs in our simulation.

### 2.2.1 *Numerical set-up*

We zoom in on the high spatial (20 pc) and temporal (1 Myr) resolution simulations of galaxy mergers by Capelo et al., 2015, using the N-body smoothed particle hydrodynamics code `Gasoline` (Wadsley, Stadel, and Quinn, 2004), an extension of the pure gravity tree-code `Pkdgrav` (Stadel, 2001). The version we used includes explicit line cooling for atomic hydrogen and helium, and metals (Shen, Wadsley, and Stinson, 2010), a physically motivated prescription for star formation, supernova feedback, and stellar winds (Stinson et al., 2006), as well as BH accretion and feedback (Bellovary et al., 2010). The original resolution was 20 pc, we increase it to 1 pc by reducing the value of the softening length, $\epsilon$, of all particles (gas, BHs, stars, and DM).

We use the 1:4 coplanar, prograde–prograde merger of galaxies (namely Run 07 in Capelo et al. 2015, hereafter the "original simulation"). At the beginning of the original simulation, there are two coplanar galaxies, one being four times more massive than the other, both hosting in their centres a supermassive BH (BH1 and BH2), whose masses are proportional to the mass of the bulge of each host galaxy. We refer to Capelo et al., 2015 for a detailed description of the initial set up.

We chose this merger because the mass ratio 1:4 is usually chosen as the boundary between major and minor mergers. The merger time-scale in major mergers is shorter, as the dynamical friction deceleration scales as $M_{\rm Satellite}$ (see Eq. (56)), where $M_{\rm Satellite}$ is initially the mass of the lighter galaxy, then that of the stellar nucleus and, at the end, the mass of the orbiting BH. We expect therefore that forming a supermassive BH binary is easier in mergers of similar-mass galaxies. For instance, in simulations with small mass ratios, down to 1:10 in Capelo et al., 2015, the time needed for the two BHs to reach kpc separation (from an initial separation equal to the sum of the virial radii of the merging galaxies) is roughly

3 Gyr, much longer than the ~1 Gyr needed in the 1:4 simulation. As a consequence, we expect binaries resulting from minor mergers to be rarer. However, major mergers are less common than minor mergers (Fakhouri, Ma, and Boylan-Kolchin, 2010) and therefore do not comprise the bulk of the merging population. A mass ratio of 1:4 appears to be a reasonable compromise between the rarity of the galaxy merger itself and the duration of the merger process. Additionally, in this particular simulation, a nuclear coup occurs (Van Wassenhove et al., 2014): the nucleus of the primary galaxy is completely disrupted by tidal forces and BH1, which is more massive than BH2, becomes a satellite and orbits around BH2 and the nucleus of the secondary galaxy. A simple way to understand this counter intuitive result is that the secondary galaxy interacts with a much more massive galaxy, and is therefore greatly affected by the merger, triggering a starburst and enhancing the central density. At the opposite, the primary galaxy does not "feel" the secondary galaxy and is therefore not affected. Overall, the secondary nucleus becomes denser and disrupt the one of the primary. The result of this nuclear coup is that, since, as noted above, the dynamical friction force scales as $M_{Satellite}$, the orbital decay is faster when the orbiting BH is the most massive of the two.

We begin our zoom-in simulations at $t_0$, where $t_0$ corresponds to the time of the snapshot, in the original simulation, closest in time to that of the first apocentre, in the merger phase (see Capelo et al., 2015), when the distance between the two BHs is smaller than 1.2 kpc. In the original simulation, $t_0$ =1.20 Gyr after the beginning of the merger (see Capelo et al., 2015) but, from now, we denote by $t_0 = 0$, and evolve the system for 30 Myr in order to capture the formation of the supermassive BH binary. We show a snapshot of our initial conditions in Fig. 14 (left), where, clearly, BH2 (black triangle) is surrounded by a dense nucleus whereas the nucleus around BH1 (black dot) has been partially disrupted. In the right panel, we show the distance between the two BHs as a function of time.

### 2.2.2 *Effect of dynamical friction*

We show in this Section that dynamical friction is sufficient to explain the decay of the orbiting BH. We calculate how the specific angular momentum, $L = rv$ in the case of circular orbits, where $r$ is the distance between the two BHs and $v$ the relative velocity between the two BHs, varies with time. We assume that BH1 moves on circular orbits and feels dynamical friction from a uniform background with a density varying with time. This means that the specific angular momentum varies according to the following equation[3]:

$$\frac{dL}{dt} = -4\pi G^2 M_{BH_1} \frac{r(t)}{v(t)^2} \ln(\Lambda)\rho(t) \left[\mathrm{erf}(X) - \frac{2X}{\sqrt{\pi}} e^{-X^2}\right], \tag{62}$$

3 We assume the distribution function to be Maxwellian and consider only the slow moving particles from Eq. (56).

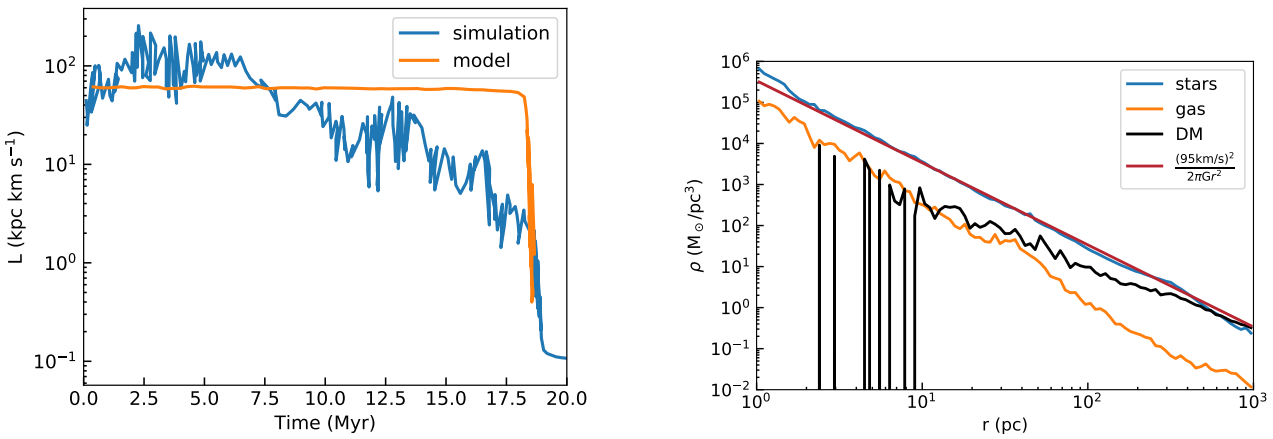


Figure 15: **Left:** Specific angular momentum as a function of time, both in the simulation (blue) and obtained through numerical integration of Eq. (62) (orange). **Right:** Density profile at $t = 10\,\text{Myr}$.

where $X = v/\sqrt{2}\sigma$ and $\sigma$ is the velocity dispersion around the orbiting object, set equal to $100\,\text{km s}^{-1}$ by fitting the density profile of the nucleus of the secondary galaxy with an isothermal sphere (Fig. 15, right). The orbiting BH does not accrete much material during the simulation and its mass, $M_{BH_1}$, varies by less than 10 per cent during the simulation, therefore $M_{BH_1}$ is set to its value at $t_0$, *i.e.* $6.5 \times 10^6\,M_\odot$. The quantities $v(t)$ and $r(t)$ are direct outputs from the simulation, whereas $\rho(t)$ is estimated from the spherical total density profile centred on BH2 (Fig. 15, right) at the position of BH1: $\rho(t) = \rho(r(t))$. The Coulomb Logarithm is set to $\ln(\Lambda) = \ln\left(b_{max}\sigma^2/G\,(M_{BH_1} + m)\right) \sim 10$, as $m \sim 5 \times 10^3\,M_\odot$ is the average mass of particles in the simulations and $b_{max} \sim 2\,\text{kpc}$, a rather arbitrary value which does not strongly impact the final result. Finally, for the initial conditions, we take the value of the specific angular momentum from the simulation at $t_0$.

In Fig. 15 (left), we show the value of the specific angular momentum as a function of time obtained through the numerical integration of Eq. (62) (orange line), together with the actual value in the simulation (blue line). We insist on the fact that dynamical friction is *not* implemented as such in the simulation, where the total force is computed using a multipole hierarchical method but where the resolution is such that we resolve the sphere of influence of the BH and the wake of material that dominates the dynamical friction force (see §2.3.1). Both in the model and in the simulation, we observe a sharp decay at $\sim 17\,\text{Myr}$, meaning that the loss of angular momentum through dynamical friction is sufficient to make the two bodies get close and form a binary. At this point, we stop the integration of Eq. (62) because our model is not valid anymore: when the binary is formed, the dynamics is mainly driven by single interactions between the two BHs (see §1.3) and not by dynamical friction. Of course there are differences between our model and the simulations but this is expected since the dynamics is not only driven by dynamical friction but also by local variations of the potential, however, overall the matching is acceptable and we can safely confirm that, in

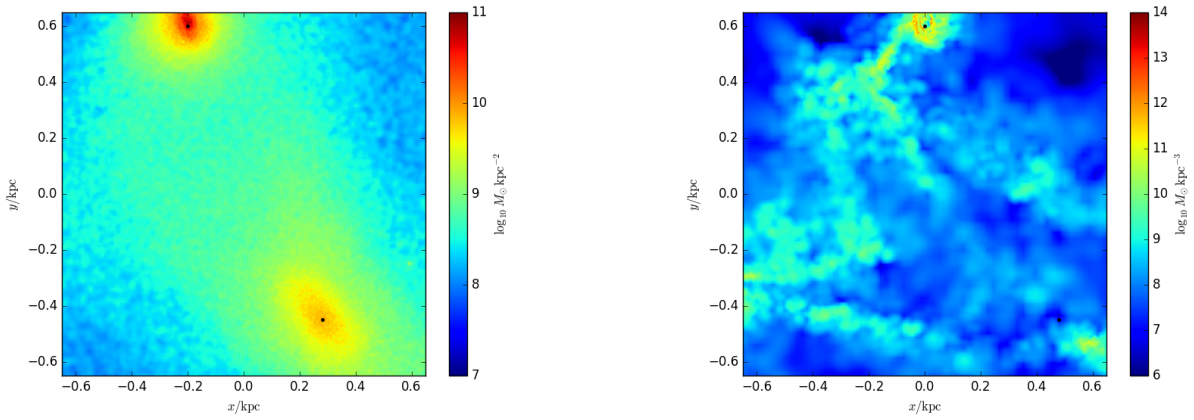


Figure 16: **Left:** 2D projection of the stellar density of the initial conditions used for our simulation. **Right:** 2D projection of the gas density of the initial conditions used for our simulation.

this situation at least, where the force resolution is of order the size of the wake, dynamical friction drives the dynamics of BHs from kpc to pc scales.

### 2.2.3 *Role of different components*

| Name | $\epsilon_{gas}$ pc | $\epsilon_{star}$ pc | $\epsilon_{BH}$ pc | Description |
|---|---|---|---|---|
| R1 | 1 | 0.5 | 0.25 | X |
| R2 | 2 | 1 | 0.5 | X |
| R2b | 2 | 1 | 0.5 | Begins at 12 Myr, BH1 shifted by 3 pc |
| R2c | 2 | 1 | 0.5 | Begins at 12 Myr, BH2 velocity increased by 20 per cent |
| R2d | 2 | 1 | 0.5 | Begins at 12 Myr, BH1 shifted by 16 pc |

Table 2: Simulations performed. We vary the softening length, $\epsilon$, and, in some cases make minor changes on the BH at 12 Myr.

In the previous Section, we have shown that dynamical friction drives the dynamics of BHs. In this Section, we answer which component between gas, stars and DM contribute the most to dynamical friction. As dynamical friction scales linearly with the density (see Eq.(56)) and, in the central region, within 10 pc, stars dominate in this merger remnant (see Fig. 15, right), it seems that stars should contribute to the bulk of dynamical friction. However, in contrast to the smooth stellar density, the gas density is clumpy (Fig. 16), therefore gas clumps could affect the dynamical evolution of BHs, sourcing random motions that can arise through BH-clump interactions (Fiacconi et al., 2013; Roškar et al., 2015; Souza Lima et al., 2016).

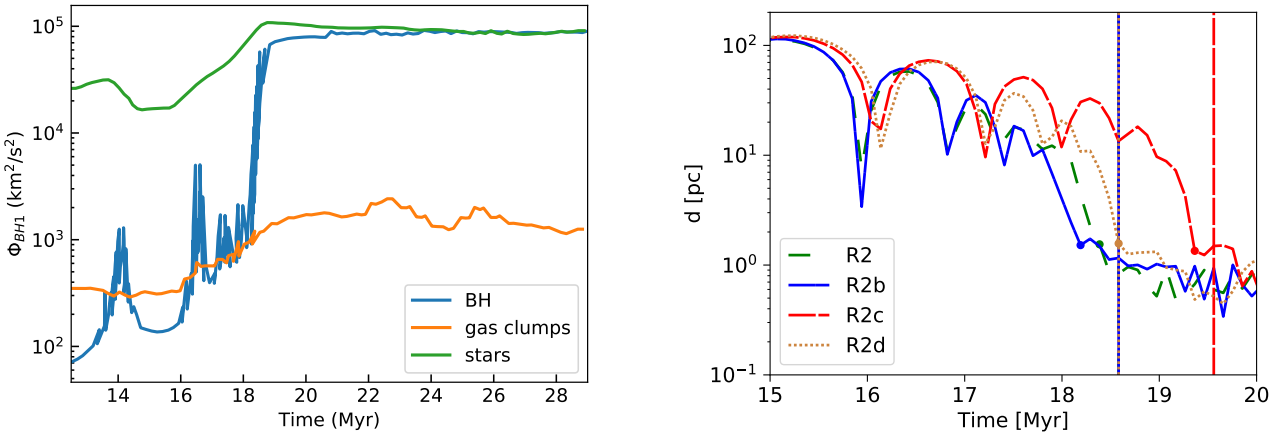


Figure 17: **Left:** Potential felt by BH1 from BH2 (blue line), from gas clumps (orange line) and from stars within 1 kpc (green line). **Right:** Distance betweem the two BHs as a function of time in our simulations.

As a first test to verify the role of gas, we use the clump finder `skid` (Stadel, 2001) to identify all the gas clumps within 1 kpc from BH1. Gas clumps have masses between a few times $10^4\,M_\odot$ and $10^6\,M_\odot$. The distribution of the mean density of clumps peaks at $\sim 10^2$ particles cm$^{-3}$, which is in very good agreement with the typical densities of giant molecular clouds (McKee, 1999), with a small tail at higher densities (the mass fraction in gas with density $> 10^4$ particles cm$^{-3}$ is $< 10\%$). We then estimate the potential felt by BH1 due to (i) stars within 1 kpc from BH1, (ii) gas clumps in the same region, (iii) BH2. We show our results in Fig. 17 (left). The potential generated by gas clumps remains at all times at least one order of magnitude below the stellar potential and we can therefore conclude that, in this situation at least, gas does not play an important role. We also see that, at around 17 Myr, the potential of BH2 becomes as important as all stars within 1 kpc: the binary has formed.

As a second test, we run the exact same simulation, but with a lower resolution (2 pc, see Table. 2 for details) and slightly changing the orbital parameters of BHs 12 Myr after our simulation has begun. Either the position of BH1 is shifted by 3 or 16 pc or, at fixed separation, the speed of BH2 is increased by 20 per cent. We show the distance between the two BHs in Fig. 17 (right). All cases are very similar, we conclude therefore that the BH trajectory is not significantly affected by gaseous discrete perturbers.

## 2.3 DYNAMICAL FRICTION IN NUMERICAL CODES

In the previous Sections, we have understood the physical origin of dynamical friction and its effects onto the dynamics of BHs. In this Section, we try to understand if and how dynamical friction can be included in numerical codes to better capture the dynamics of BHs.

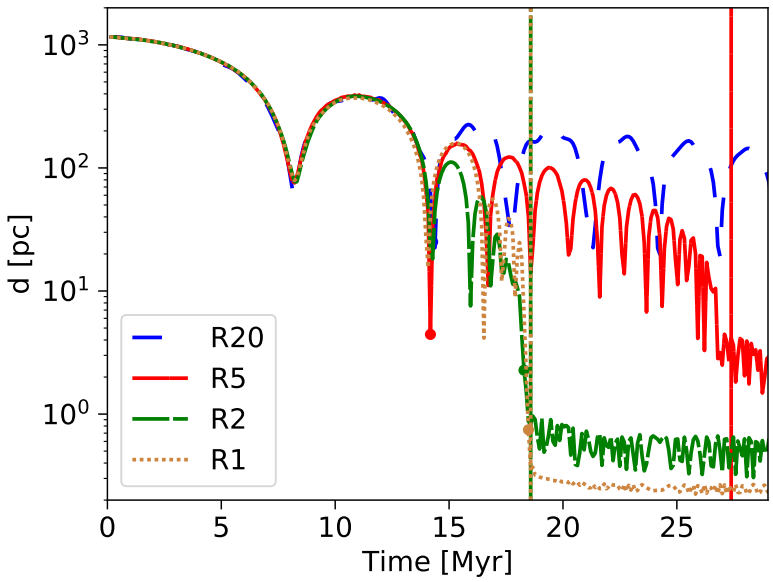


Figure 18: Distance between the two BHs as a function of time for the same simulation run at different resolutions.

### 2.3.1 *A minimum resolution required*

As discussed in §2.1, most of dynamical friction is sourced by material closer than the influence radius of the BH $r_{inf}$, therefore, in a numerical simulation, the resolution must be at least $r_{inf}$ if one wants to resolve the over-dense region, and therefore dynamical friction (Johansson, Naab, and Burkert, 2009; Chapon, Mayer, and Teyssier, 2013; Gabor and Bournaud, 2013).

To test this, we use the same initial conditions as described in §2.2, in which BH1 has a mass $M_\bullet = 6.5 \times 10^6\,M_\odot$ and moves in a medium with velocity dispersion $\sigma = 100\,\mathrm{km\ s^{-1}}$, so that the influence radius is $r_{inf} = 3\,\mathrm{pc}$. We run the same simulations with 4 different resolutions: 20, 5, 2 and 1 pc (namely R20, R5, R2 and R1).

We show in Fig. 18 the distance between the two BHs as a function of time in all four simulations. Simulations resolving the influence radius, and therefore the wake created by the lagging material, show similar results, proving the convergence of the results, whereas the ones with a resolution coarser than 3 pc show a different dynamics. This confirms that the minimum required resolution to resolve the dynamical friction phase in a numerical simulation is given by the influence radius.

### 2.3.2 *Implementation in Ramses*

In cosmological simulations, the typical resolution is $\sim 100\,\mathrm{pc} - 1\,\mathrm{kpc}$, much larger than the pc-scale needed to resolve $r_{inf}$ for a $10^7\,M_\odot$ BH in a Milky-Way like galaxy. Therefore,

we must remove by hand the momentum that a BH would lose through dynamical friction if we were able to resolve the phenomenon. In this Section we first describe how we implement unresolved dynamical friction in the adaptive mesh refinement code `Ramses` (Teyssier, 2002, described in Appendix 6) for collisionless particles (stars and dark matter); the code already includes a correction for dynamical friction from gas (Dubois et al., 2012, detailed in Appendix 6).

We follow an approach similar to Tremmel et al., 2015, although we include not only the contribution to dynamical friction from slow-moving particles (first term in Eq. (56)) but also from fast-moving particles (second term in Eq. (56)), which can play an important role when the density profile becomes shallow (Antonini and Merritt, 2012; Dosopoulou and Antonini, 2017). Note that Rantala et al., 2017 adopted another approach, instead of using a subgrid model, they massively refine around BHs to capture dynamical friction with the gravity solver. This is more accurate (and allows to include post newtonian terms) but is computationally more expensive and currently does not work with the hydrodynamics.

We measure all the quantities needed to estimate dynamical friction in a sphere $\mathcal{S}$ centered on the BH with a radius $4\Delta x$, where $\Delta x$ is corresponds to the minimum grid size. We chose $\mathcal{S}$ to be consistent with the already existing implementation for gas accretion, feedback and dynamical friction (see Appendix 6).

According to Eq. (56), the deceleration due to dynamical friction is:

$$\begin{aligned}\mathbf{a}_{\rm DF} = -4\pi G^2 M_\bullet \frac{\mathbf{v}}{v^3}(\ln(\Lambda)\int_0^v 4\pi u^2 \tilde{f}(u)du + \\ \int_v^\infty 4\pi u^2 \tilde{f}(u)\left[\ln\left(\frac{u+v}{u-v}\right) - 2\frac{v}{u}\right]du),\end{aligned} \tag{63}$$

where we denote as $M_\bullet$ the mass of the BH, as $\mathbf{v}$ (with magnitude $v$) the relative velocity of the BH with respect to the velocity of the background $\langle \mathbf{v}_\star \rangle$, defined below in Eq. (65); $\ln(\Lambda)$ is the Coulomb logarithm (expression is given in Eq. (66)); and $\tilde{f}$ is[4]:

$$4\pi u^2 \tilde{f}(u) = \frac{3}{256\pi\Delta x^3}\sum_{i\in\mathcal{S}} m_i \delta(|\mathbf{v}_i - \langle \mathbf{v}_\star \rangle| - u). \tag{64}$$

Here $\mathbf{v}_i$ (with magnitude $v_i$) is the velocity of particle $i$, $m_i$ is the mass of particle $i$ and $\delta$ is the Dirac function.

4 Note that, contrary to Eq. (56), we include $m_\star$ in $\tilde{f}$ as particles can have slightly different masses.

The velocity of the background, $\langle \mathbf{v}_\star \rangle$, is simply the mass-weighted velocity of all particles (except the BH) enclosed in $\mathcal{S}$:

$$\langle \mathbf{v}_\star \rangle = \frac{1}{M} \sum_{i \in \mathcal{S}} \mathbf{v}_i m_i \,, \tag{65}$$

where $M$ is the total mass enclosed in $\mathcal{S}$ (excluding BHs). We stress here that the background velocity is computed for stars and dark matter separately, the reason is that dynamical friction assumes particles with similar masses, which is a reasonable assumptions if we consider an ensemble of stars, or an ensemble of dark matter particles, but not if we consider stars and dark matter particles together. Therefore we compute the contribution from dark matter, $\mathbf{a}_{\mathrm{DF,DM}}$, and stars, $\mathbf{a}_{\mathrm{DF},\star}$ separately.

In our case, gravity is computed self-consistently by the code outside $\mathcal{S}$; therefore, the integration over $b$ (see §2.1) must be stopped at $b_{max} = 4\Delta x$ if we do not want to double-count dynamical friction. According to Eq. (57), this naturally leads to:

$$\ln(\Lambda) = \ln\left(\frac{v^2 4\Delta x}{G\, M_\bullet}\right) \tag{66}$$

$$= \ln\left(\frac{4\Delta x}{r_{def}}\right) \,, \tag{67}$$

where $r_{def} \equiv G\, M_\bullet / v^2$ is the deflection radius, corresponding to the impact parameter at which particles are deflected by 90° (see Appendix 7). Furthermore, as explained in Beckmann, Slyz, and Devriendt, 2018, using subgrid models when resolution is sufficient to account for dynamical friction can lead to incorrect results, therefore, if $4\Delta x \leqslant r_{inf}$ (see §2.3.1), $\mathbf{a}_{\mathrm{DF}}$ must be set to 0. In practice, as computing the velocity dispersion $\sigma$ (necessary to compute $r_{inf}$) is expensive, we assume $r_{inf} \sim r_{def}$ and the criterion used to set $\mathbf{a}_{\mathrm{DF}}$ to 0 is $4\Delta x \leqslant r_{def}$.

### 2.3.3 *Tests*

#### 2.3.3.1 *Isolated dark matter halo*

In order to compare the dynamical friction timescale with analytical estimates (Lacey and Cole, 1993; Colpi, Mayer, and Governato, 1999; Taffoni et al., 2003), we test our implementation on a BH moving in a dark matter halo.

The dark matter halo, initialized with `Dice` (Perret, 2016), follows a Navarro, Frenk and White (NFW, Navarro, Frenk, and White, 1997) profile with a total virial mass $M_{vir} = 2 \times 10^{11}\, M_\odot$, a concentration parameter of 4 and a virial radius $R_{vir} = 45\,\mathrm{kpc}$, typical of redshift 3. We set the total spin parameter to 0.04 consistent with the average spin parameter of cosmological dark matter halos (Bullock et al., 2001), which only mildly evolves between

$z = 3$ and today (Muñoz-Cuartas et al., 2011; Ahn et al., 2014). The BH mass is set to $10^8\,M_\odot$, it is initially 5 kpc away from the center with a tangential velocity of 57 km s$^{-1}$, corresponding to to 50% of the circular velocity.

As done in Tremmel et al., 2015, we can estimate the goodness of the method by comparing it to the analytical estimate of the "sinking time", $\tau_{DF}$, defined as the time it will take for a *satellite* to sink to a *target*, using Eq. (12) from Taffoni et al., 2003:

$$\tau_{DF} = 0.6\frac{r_c^2 v_c}{G M_s}\log^{-1}\left(1+\frac{M_{vir}}{M_s}\right)\left(\frac{J}{J_c}\right)^{\alpha} \tag{68}$$

$$\simeq 1.4\,\mathrm{Gyr}\left(\frac{r_c}{100\,\mathrm{pc}}\right)^2\left(\frac{v_c}{10\,\mathrm{km\ s^{-1}}}\right)\left(\frac{10^4\,M_\odot}{M_s}\right)\times \log^{-1}\left(1+\frac{M_{vir}}{M_s}\right)\left(\frac{J}{J_c}\right)^{\alpha}, \tag{69}$$

where $M_{vir}$ is the virial mass of the *target*, $v_c$ is the circular velocity at the virial radius, $G$ the gravitational constant, $r_c$ is the radius at which a test particle moving in the potential of the *target* has the same energy as the *satellite*, $M_s$ is the mass of the *satellite*, $J$ is the specific angular momentum of the *satellite* in the frame of the *target*, $J_c$ is the specific angular momentum of circular orbit at $r_c$ and $\alpha$ depends on $M_s$, $M_{vir}$, $R_{vir}$ and $r_c$ and is given by Eq. (15) from Taffoni et al., 2003. In this case, the target is the halo and the satellite is the BH. Using this approach, we find that the BH should sink in the potential well of the halo in 600 Myr.

We perform two simulations which only differ by the presence (`PD`), or not (`NoDrag`), of our subgrid model for dynamical friction on the BH. In both cases, the size of the box is 100 kpc, slightly larger than $2R_{vir}$ and we allow refinement from levels 7 to 11, leading to a maximum physical resolution of $\Delta x = 50$ pc, similar to what simulations reach in cosmological zooms (Dubois, Volonteri, and Silk, 2014). The deflection radius varies between 10 and 100 pc: it is at best resolved by 2 cell elements, therefore dynamics is generally not treated properly and dynamical friction must be added *ad hoc* with our subgrid model when necessary. Refinement is done using a quasi-Lagrangian criterion: a cell is refined if its mass exceeds $8\times m_{DM}$, where $m_{DM}$ is the mass of dark matter particles, and we refine at maximum level up to $4\Delta x$ around the BH. We set the mass of dark matter particles to $10^5\,M_\odot$, in good agreement with the value suggested by Power et al., 2003: $m_{DM} = M_{vir}\,(R_{vir}/\Delta x)^{-2} \sim 2\times 10^5\,M_\odot$.

We show in Fig. 19, for both simulations, the distance between the BH and the center of the halo; we also include for comparison the analytical estimate given by Eq. (69). The result is quite clear and in agreement with Tremmel et al., 2015: adding unresolved dynamical friction contributes to recover sinking times estimated analytically. In the following Section, we set up a more realistic problem where a BH sinks in a galaxy including not only dark mat-

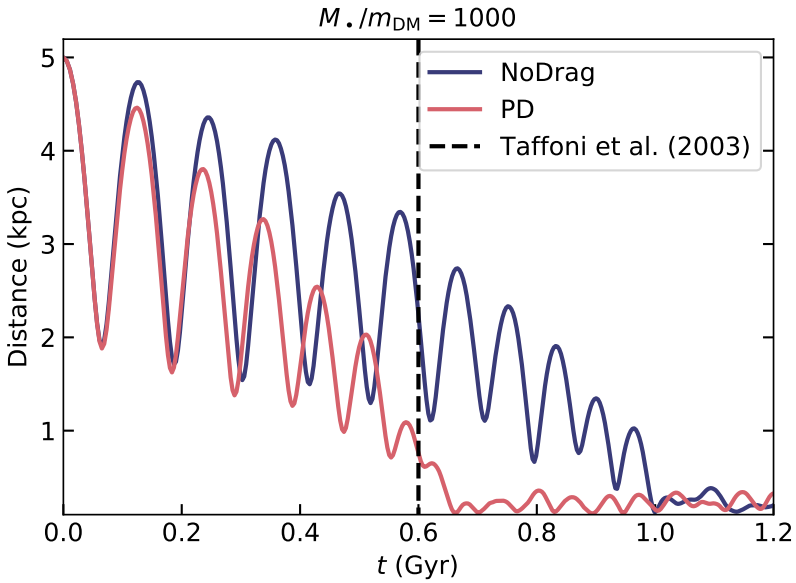


Figure 19: Distance of the BH to the center of the halo as a function of time. The vertical dashed line is the analytical estimate of the total sinking time from Taffoni et al., 2003. With our prescription, the sinking time is much shorter than without and in very good agreement with the analytical estimate. The resolution in these simulations is 50 pc and the BH to dark matter mass particle ratio set equal to 1000.

ter but also gas, stars and many associated processes (cooling, star formation, supernovae feedback; see Appendix 6).

#### 2.3.3.2 *Isolated galaxy*

We run a suite of simulations (see Table 3) of a BH sinking in the potential well of an idealized isolated galaxy. Our suite contains low-resolution ($\Delta x = 50\,\mathrm{pc}$) simulations, similar to what high-resolution zoomed cosmological simulations can reach today. Thus it is a good test to see how our implementation will act in this context. Contrary to the dark matter halo case, we do not have analytical estimates to provide a benchmark. To overcome this issue, we run a high resolution test ($\Delta x = 1\,\mathrm{pc}$) to perform the comparison. The setup is chosen such that, with 50 pc resolution, during the sinking, the deflection radius, is not always resolved (see Fig. 20). In this case, dynamics is not properly treated and dynamical friction must be added *ad hoc* with our subgrid model. Conversely, with 1 pc resolution the deflection radius is always resolved during the sinking and dynamical friction is well captured by the gravity solver of `Ramses`, thus providing the correct dynamics.

We initialize with `Dice` an ideal galaxy at redshift 3 with a total virial mass of $2 \times 10^{11}\,\mathrm{M}_\odot$ and a spin parameter of 0.04. The galaxy is composed of four components.

| Name | Dynamical friction | $\Delta x$ pc |
|---|---|---|
| `NoDrag` | none | 50 |
| `GnB_nPD` | gas | 50 |
| `GnB_PD` | gas+stars+dark matter | 50 |
| `HR` | none | 0.76 |

Table 3: Different simulations performed for the isolated galaxy test, with their name and the use, or not, of our new model, and resolution of the simulation.

- A dark matter halo with a mass of $1.95 \times 10^{11}\,M_\odot$, slightly lighter than in §2.3.3.1. It has a virial radius of 45 kpc and the density follows a NFW profile with a concentration parameter of 4.
- A gas disk with a total mass of $2.4 \times 10^9\,M_\odot$. The density follows an exponential disk + sech-z profile with a scale radius of 1.28 kpc and an aspect ratio of 1:10 (Spitzer, 1942). We impose an initial constant absolute metallicity and temperature of $10^{-3}$ and $10^5$ K, respectively.
- A stellar disk with a total mass of $1.6 \times 10^9\,M_\odot$. The density follows an exponential disk + sech-z profile with a scale radius of 1.28 kpc and an aspect ratio of 1:10. We impose an initial constant absolute metallicity of $10^{-3}$. Additionally, to avoid unphysical initial starbursts regularly found in ideal simulations (Capelo et al., 2015), we give an age distribution to stellar particles to mimic a 5 $M_\odot\ yr^{-1}$ star formation rate.
- A stellar bulge with a total mass of $8 \times 10^8\,M_\odot$. The density follows a Hernquist profile (Hernquist, 1990) with a scale radius of 0.128 kpc. We impose a constant absolute metallicity of $2 \times 10^{-4}$ (5 times smaller than in the disk to mimic the older age of stars in the bulge). Similarly, we give an age to stellar particles to mimic a 0.5 $M_\odot\ yr^{-1}$ star formation rate.

In the low-resolution simulations (50 pc), the mass of dark matter particles is set to $10^6\ M_\odot$ and that of star particles to $2 \times 10^4\,M_\odot$. In the high resolution simulations (1 pc) the mass of dark matter particles is set to $5 \times 10^4\,M_\odot$ and that of star particles to $2 \times 10^3\,M_\odot$. In both cases the size of the box is 100 kpc and we allow for refinement from levels 7 to 11 in the low resolution simulations and from 7 to 17 in the high resolution one, refining the mesh when $M_{DM}^{cell} + 10M_b^{cell} \geqslant 8m_{DM}$, where $M_{DM}^{cell}$ and $M_b^{cell}$ are, respectively, the mass of dark matter and baryons in the cell. Maximum refinement is enforced within $4\Delta x$ around the BH.

After initializing this galaxy, we switch on cooling, star formation, supernovae feedback (see Appendix 6) and let the galaxy relax for 100 Myr. At that point, a BH with mass $10^7\,M_\odot$

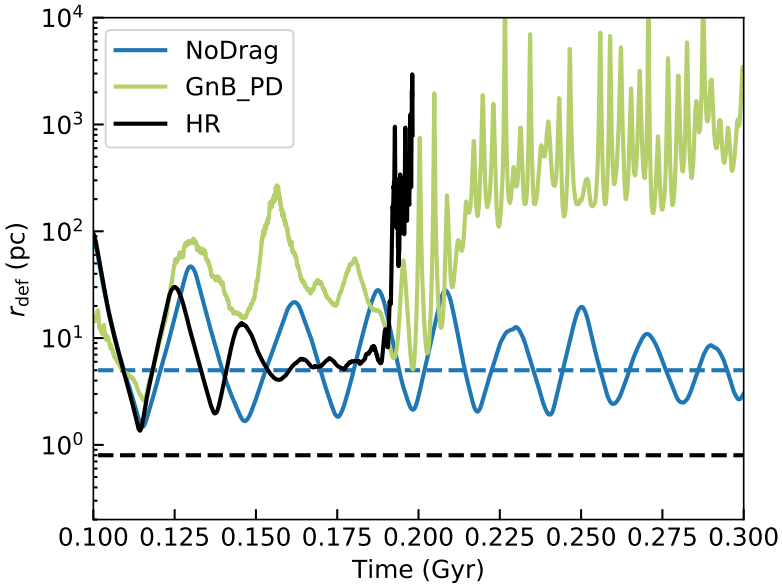


Figure 20: Deflection radius (solid line) and resolution of the different simulations (dashed lines) of idealized isolated galaxies. In the low-resolution case (blue and green lines) the deflection radius is not always resolved, leading to incorrect dynamics of the BH and the need to add unresolved dynamical friction. In the high resolution run (black line) the deflection radius is always resolved and dynamical friction is self-consistently captured by the gravity solver. All quantities shown as a function of time.

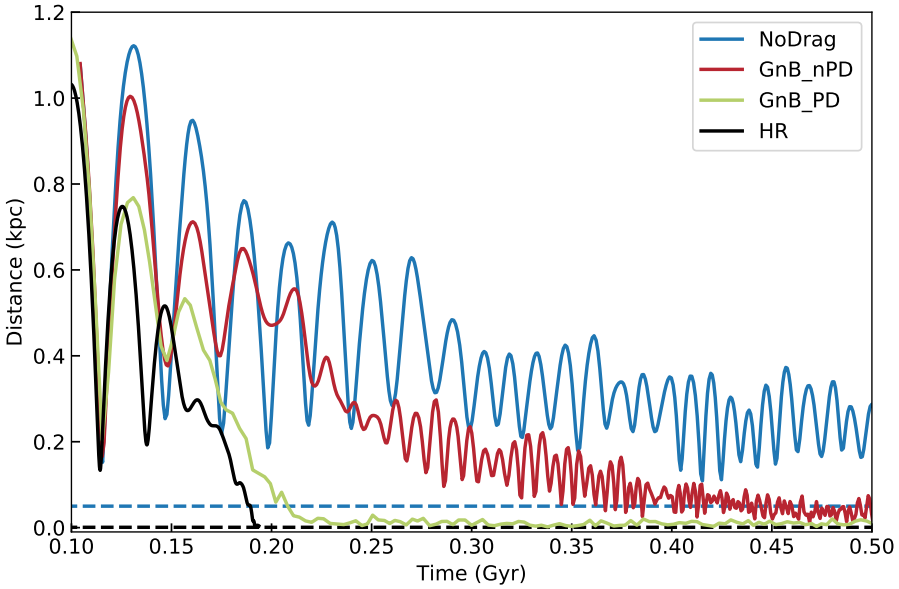


Figure 21: Distance of the BH to the center of the galaxy as a function of time and resolutions of the different simulations (dashed lines). The good behavior of our model is confirmed by the agreement between the solid green curve (low resolution, use of our model) and the solid black one (high resolution).

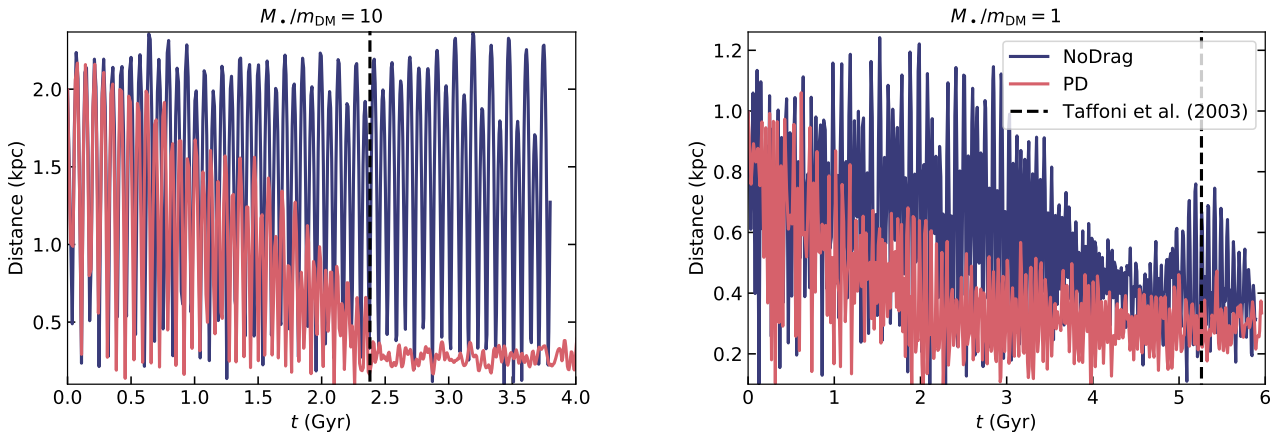


Figure 22: Different simulations performed to test the effect of reducing the mass ratio between the BH and dark matter particles. We indicate the use (`PD`) or not (`NoDrag`) of our prescription for dynamical friction. If the BH mass is similar to the dark matter particle mass, the efficacy of the model becomes limited.

is placed in the $z = 0$ plane, 1 kpc from the center and with a tangential velocity of 21 km/s, corresponding to 30% of the circular velocity. Accretion and feedback from the BH are not included in order to keep the BH mass constant and isolate the effects of dynamical friction. We include dynamical friction with different implementations: from collisionless particles and gas, or only from gas. The simulation properties and set-up are summarized in Table 3.

We show in Fig. 21, for all our simulations, the distance between the BH and the center of the galaxy as a function of time. We first stress the difference between low resolution simulations with gravity only, *i.e.* without including the dynamical friction model (`NoDrag`, blue line), and the simulations at high resolution where the deflection radius is resolved (`HR`, black line). In agreement with the results of Pfister et al., 2017, resolving at least the deflection radius is mandatory to properly capture the dynamics of the BH in the dynamical friction phase. The use of gas dynamical friction as it was already implemented in `Ramses` (`GnB_nPD`, red line), helps in driving BHs toward the center but is clearly not enough.

The simulation where the influence radius is not always resolved, but in which we include sub-grid dynamical friction from gas, stars and dark matter following our implementation (`GnB_PD`, green line), is in excellent agreement with the high resolution simulation (`HR`, black line), confirming the good behavior of our model in a realistic, although idealized, galaxy.

#### 2.3.3.3 *Limits of the model: low mass black holes*

In this Section we explore the limits of our implementation when a BH has a mass so low that two-body interactions with star and dark matter particles significantly perturb its dynamics (see §4.1.3).

| $M_\bullet/m_{DM}$ | $d_0$ kpc | $v_0$ km s$^{-1}$ | $\tau_{DF}$ Gyr |
|---|---|---|---|
| 10 | 2 | 8.2 | 2.38 |
| 1 | 1 | 6 | 5.26 |

Table 4: Different simulations we perform to test the limits of our model in terms of particle mass ratio. We indicate the different mass ratio between the BH and dark matter particles, the initial distance of the BH from the center of the halo, the initial velocity of the BH and the analytical estimate for the time the BH should take to reach the center of the halo from Taffoni et al., 2003. In all cases, we run a simulation with (`PD`) and without (`NoDrag`) our model.

We run simulations similar to those described in §2.3.3.1 but decreasing the mass of the BH down to the mass of dark matter particles ($m_{DM} = 10^5\,M_\odot$). To contain computational costs, we also change the orbital parameters of the BH such as the analytical estimates from Taffoni et al., 2003, $\tau_{DF}$, remains a few Gyrs. We list the parameters of the simulations in Table 4.

We show in Fig. 22 the distance of the BH to the center of the halo as a function of time. It is clear that our model works very well when BHs have a mass larger than 10 times the mass of particles causing dynamical friction. If the mass of the BH is similar to that of particles causing dynamical friction, however, it is scattered through two-body interactions and the model becomes less reliable, as also noted by Tremmel et al., 2015.

Here is a summary of the results presented in this Chapter:

- We presented dynamical friction and detailed the analytical calculations to obtain the resulting deceleration of BHs surrounded by stars and dark matter.
- We showed that this process is the main driver of the dynamics of BHs from kpc to pc scales.
- We showed that in order to capture dynamical friction in numerical simulations, the influence radius of BHs have to be resolved. As this is usually not the case in cosmological simulations, we presented a subgrid model for the code `Ramses` which corrects the dynamics of BHs by adding unresolved dynamical friction.

# 3

# FROM GALAXY PAIRS TO BLACK HOLE MERGERS

In this Chapter we follow the dynamics of BHs initially in galaxies separated by hundreds of kpc, until a binary BH forms. This binary may merge, or not, emitting detectable gravitational waves. A noted in §1.3, this journey to cross these 8 orders of magnitude in separation can be very long, and is still poorly understood. We first study this problem from an observational perspective: what is the probability that two galaxies observed as neighbours in the sky merge? This is important as a galaxy merger is the first step before the formation of a binary BH. We then proceed with a high-resolution cosmological simulation zoom, in which we follow BHs in a cosmological context down to redshift 4.

This Chapter is based on the following papers:

1. Pfister and Dotti, in prep
2. Pfister et al., 2019a

## 3.1 A CATALOG TO UNDERSTAND PROPERTIES OF MERGING PAIRS

Mergers of massive galaxies are the natural path to the formation of massive BH pairs and binaries (see §1.3). They have been explored thoroughly from a theoretical point of view, both analyzing and post–processing the outcomes of coarse but large cosmological simulations (Steinborn et al., 2016; Volonteri et al., 2016), as well as higher resolution isolated mergers starting from idealized initial conditions (Capelo et al., 2015).

On the observational side, samples of galaxy pairs and dual AGNs have been compiled starting from a variety of data at different wavelengths. A widely used technique to select two galaxies as a physical pair if their relative projected distance (d) and redshift difference ($\Delta z$) are smaller than given thresholds $d_{th}$ and $\Delta z_{th}$. As an example of the results obtained, a net increase in single and dual AGNs activity has been found at decreasing projected separations between galaxy pairs (Kocevski et al., 2012; Goulding et al., 2018). A fraction of the selected pairs, however, could have very large real 3D separations so that the two galaxies in the pair are actually in isolation, and will not merge, nor interact, within a Hubble time. Vice versa, some real bound galaxies, that are fated to merge within 10 Gyr could be excluded from the sample, lying just outside the thresholds $d_{th}$ and $\Delta z_{th}$.

We take full advantage of the results of the `HorizonAGN` cosmological simulation (Dubois et al., 2014) to build mock catalogues of galaxy pairs and determine the best values of $d_{th}$ and $\Delta z_{th}$ to select galaxies which will merge.

### 3.1.1 *Simulated data*

We use the data from the `HorizonAGN` simulation (Dubois et al., 2014). This is one of the largest hydrodynamical cosmological simulation available, it is about 140 Mpc side at $z = 0$. It has been run with the cosmological code `Ramses` and it contains galaxy formation subgrid physics (star formation, supernovae, BH accretion and feedback, cooling; see Appendix 6). This simulation reproduces many properties of real galaxies (Laigle et al., 2017; Kaviraj et al., 2017), therefore we can use it to produce mock catalogs, from which we can obtain realistic thresholds observers could use to better post-process observations.

#### 3.1.1.1 *Galaxies in the lightcone*

A lightcone has been produced while the simulation was running, from this cone mock images can be produced (Fig. 23). The lightcone is produced using the method from Pichon et al., 2010 sketched in Fig. 24 (left). Laigle et al., 2017 extracted galaxies from this lightcone and produced a catalog containing the following information for each galaxy:

- stellar mass M;
- star formation rate SFR;

Figure 23: Simulated composite image from the HorizonAGN simulation made using the lightcone. Taken from Kaviraj et al., 2017.

- location on the sky with right ascension and declination;
- true redshift, $z_{\text{true}}$, corresponding to the time at which the galaxy exists, *i.e.* the time of the snapshot in which the galaxy is. This is directly measured in the simulation;
- observed redshift, $z$, corresponding to the redshift an observer would measure, which takes into account the doppler shift and the Hubble flow. From now on, we drop the "observed", simply referring to "the redshift".

#### 3.1.1.2 *Galaxies in the box*

Galaxies in the box have been identified with AdaptaHOP (Aubert, Pichon, and Colombi, 2004). The algorithm detects gravitationally bound structures containing at least 50 stellar particles, therefore having a minimum mass of $10^8$ $M_\odot$. Using again the sketch in Fig. 24 (left), the blue, red, green, grey and yellow dots (galaxies) are now identified both in the box and in the lightcone. However, initially, galaxies in the lightcone and in snapshots are not matched. This matching is important because, for galaxies in the lightcone, similarly to galaxies in the sky, we have only an image at one particular time. Galaxies in the box are instead evolved from $z = 100$ down to $z = 0$, therefore we know their history. Laigle et al., 2017 associated each galaxy that can be observed in the lightcone to a galaxy in the box, connecting the "observational view" to how a galaxy actually evolves over cosmic time.

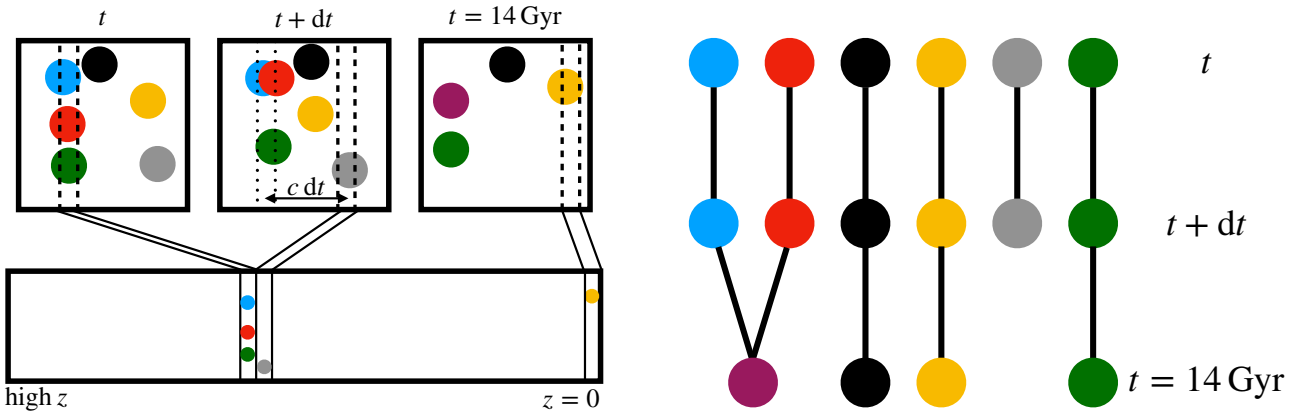


Figure 24: **Left:** Sketch of the construction of a lightcone. Squares on the top panel represent the simulated box, which is evolved in time (see Appendix 6). Slices of the box are stored at each timestep and are then stacked to form the lightcone (bottom panel). Note that some galaxies are present at all time in the box, but not in the lightcone, and that some galaxies (the black one here) can be in the box without being in the lightcone. **Right:** Merger tree associated with the simulation sketched, some galaxies merge (blue-red pair), some remain isolated for a long time (yellow, black and green) and some "dissolve" as they have no child identified (grey).

#### 3.1.1.3 *Merger tree*

The merger tree of galaxies in the box has been produced with `TreeMaker` (Tweed et al., 2009), galaxies containing particles with the same ID at different times are matched to form the history of each galaxy. With this we can follow galaxies from their birth down to $z = 0$, as sketched in Fig. 24 (right).

### 3.1.2 *Building the catalog*

With all the data presented in the previous Sections, for a pair of galaxies in the lightcone, we have a pair of galaxies in the box, which we can follow down to $z = 0$ with the merger tree to see if they merge, or not, and how long it takes if it is actually the case. We select all the pairs (in the cone) fulfilling the following criteria:

- For the two galaxies, $0.05 < z < 1$;
- For the primary galaxy (the most massive in the pair), $10^9 < M_{pri} / M_\odot < 10^{11}$;
- For the mass ratio between the two galaxies, q, *i.e.*, the ratio between the mass of the secondary galaxy (the less massive in the pair) and the mass of the primary, $1/10 < q < 1$;

- For the projected distance between the two galaxies, $d$, measured at the redshift of the primary galaxy assuming a $\Lambda$CDM cosmology with *Planck* parameters (Planck Collaboration et al., 2016), $d < 5\,\mathrm{Mpc}$;
- For the redshift difference between the two galaxies, $\Delta z < 0.05$.

We end up with $4.3 \times 10^8$ pairs of galaxies, for which we know the following observational quantities: the mass of the primary and mass ratio, $M_{pri}$ and $q$, the redshift difference, $\Delta z$, the projected distance, $d$, and their SFR, $SFR_{pri}$ and $SFR_{sec}$. We also know the associated pair in the snapshots, which we can follow in the merger tree. We use the sketch in Fig. 24 (right) to list the possible cases:

1. The two galaxies live at the same time, *i.e.* they are in the same snapshot. We can then follow their history thanks to the merger tree and see if the two galaxies merge, and how long it takes ($\tau_{merger}$). For instance, the blue-red pair merges, while the blue-green pair has not merged by $z = 0$.
2. The two galaxies do not live at the same time, *i.e.* they are not in the same snapshot. We then follow the history of the the galaxy with higher redshift until the two galaxies are at the same snapshot, and then apply case 1. For instance we would trace the blue galaxy in the blue-grey pair until time $t + dt$ and then apply case 1. In this particular example, an additional feature happens: the grey galaxy "dissolves", this can happen if the galaxy looses enough stars, or is so perturbed, that it is not recognized by `AdaptaHOP` in one snapshot. As it is difficult to differentiate between a numerical and a physical disruption, pairs in which a galaxy "dissolves" are discarded.

### 3.1.3 *Validating the catalog*

To confirm that our catalog is coherent with previous studies, we perform a similar analysis as done for Fig. 2 in Snyder et al., 2017: at a given redshift $z_{pri}$ for the primary, we estimate how many pairs fulfill the criterion observers use to define a merger, *i.e.* $\Delta z < 0.02(1 + z_{pri}) = \Delta z_{th}$ and $d < 75\,\mathrm{kpc} = d_{th}$. Given this selection process, we can count how many selected pairs actually merge (true positive TP) and how many selected pairs actually do not merge by $z = 0$ (false positive FP). From this, we compute the purity $P$ in $[0, 1]$, corresponding to the fraction of selected pairs that actually merge:

$$P = \frac{TP}{TP + FP}\,. \tag{70}$$

We show our results in Fig. 25. Similarly to Snyder et al., 2017, we find that, for $z_{pri} < 1$, about 50% of the pairs selected with $\Delta z < 0.02(1 + z_{pri}) = \Delta z_{th}$ and $d < 75\,\mathrm{kpc} = d_{th}$ will not have merged by $z = 0$. This confirms the robustness of this results, the goodness of

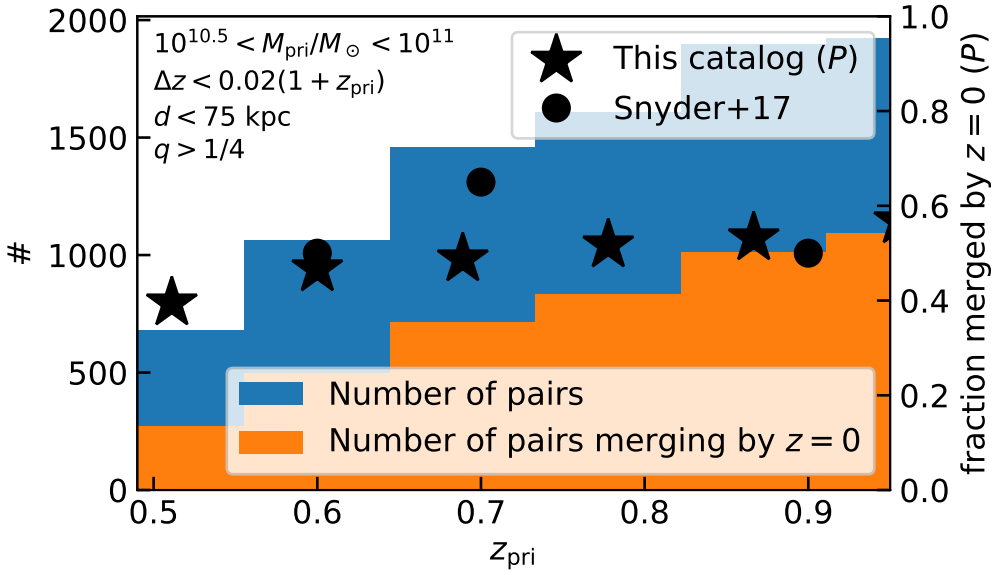


Figure 25: **Left axis, histograms**: Total number of seletected pairs (blue) and number of pairs actually merging by $z = 0$ (orange). We show in the top left corner the criterion to define a pair. **Right axis, markers**: purity of the selection in our catalog and in Snyder et al., 2017.

our catalog, and at the same time, shows that there is room from improvement in detecting true mergers from galaxy pairs (Cibinel et al., 2015; Snyder et al., 2017).

## 3.2 OPTIMAL PARAMETERS FOR DETECTING MERGERS

In this Section, we study how to obtain the best thresholds to use to detect real mergers in galaxy catalogs. From now on, we will not consider the "number of pairs which have merged by $z = 0$", since it is not representative of the instantaneous merger rate, we consider instead the "number of pairs which merge within 3 Gyr", meaning that $\tau_{merger} < 3\,\mathrm{Gyr}$. Note that for pairs with $z < 0.25$, the time left before $z = 0$ is less than 3 Gyr, in that case we consider indeed "pairs which have merged by $z = 0$". This value of 3 Gyr is rather arbitrary but is in agreement with typical merger timescales obtained in numerical simulations (Capelo et al., 2015).

### 3.2.1 *Two extreme cases*

We first begin by showing in Table 5 two specific examples from our catalog, two pairs, with, in both cases, two galaxies very close in redshift space ($\Delta z \lesssim 10^{-3}$) but, in one case, the two galaxies are far given the projected threshold usually used (projected distance d is 380 kpc) and, in the other case, they are close (37 kpc). Nonetheless, given our definition of "merger", the close pair does not merge whereas the distant one does. The reason is the

| Pair ID | $z_{pri}$ | $M_{pri}$ $10^{10}$ $M_\odot$ | $M_{sec}$ $10^{10}$ $M_\odot$ | d kpc | $\Delta z$ $10^{-4}$ | $\tau_{merger}$ Gyr |
|---|---|---|---|---|---|---|
| 6609818 | 0.6994 | 1.245 | 0.966 | 380 | 4 | 0.491 |
| 8353489 | 0.7542 | 1.554 | 0.503 | 37 | 2 | 6.427 |

Table 5: Two "extreme" pairs, 6609818 which merges rapidly and 8353489 which merges slowly given their properties.

following. Assuming that the secondary galaxy is on a circular orbit at distance $r$, it should sink in the potential well of the primary galaxy in a time given by Eq. (69), this yields:

$$\tau_{merger} \propto \frac{r^2 v_{c,pri}}{M_{sec}} \tag{71}$$

where $v_{c,pri}$ is the circular velocity at the radius of the primary galaxy. We also have the classical mass ($M_{pri}$) – radius ($R_{pri}$) and velocity – enclosed mass – radius relations:

$$M_{pri} = \frac{4}{3}\pi R_{pri}^3 \tilde{\rho} \tag{72}$$

$$v_{c,pri} = \sqrt{\frac{G\, M_{pri}}{R_{pri}}}, \tag{73}$$

where $\tilde{\rho}$ is the mean density in the galaxy. Combining all the equations above, we find:

$$\tau_{merger} \propto {M_{pri}}^{1/3} {M_{sec}}^{-1} r^2 . \tag{74}$$

Consequently, using simple thresholds on projected distance and redshift difference cannot be 100% accurate, other quantities, such as the masses, should be used (see §3.2.4).

### 3.2.2 *Goodness of the detection method*

To compare two selection methods, and judge which one is the best, we need a metric. In §3.1.3 we defined the true positive (TP), the true negative (TN) and the purity (P) which gives the fraction of selected pairs which merge. Despite appearances, purity only is not a good metric, as a very restrictive threshold (very small $d_{th}$ and $\Delta z_{th}$) would result in a purity of 100%, but would miss many true mergers. This is why we also consider the completeness C in $[0, 1]$ corresponding to the fraction of true mergers not selected:

$$C = \frac{TP}{TP + FN}, \tag{75}$$

where FN (false negative) corresponds to the number of true mergers not selected.

Clearly, purity and completeness vary in opposite directions: if the thresholds are very restrictive, as we already said, purity will be high, but completeness will be low. Conversely, if the thresholds are loose, completeness will be high and purity low. For this reason, we need a combination of P and C or, similarly, of TP, TN, FN and TN, where TN (true negative) corresponds to the number of non mergers non selected. For this purpose, we use both the *Matthews correlation coefficient*[1], MCC (Matthews, 1975), and the F1 score, defined as:

$$2\mathrm{MCC} - 1 = \frac{\mathrm{TP}\times\mathrm{TN} - \mathrm{FP}\times\mathrm{FN}}{\sqrt{(\mathrm{TP}+\mathrm{FP})(\mathrm{TP}+\mathrm{FN})(\mathrm{TN}+\mathrm{FP})(\mathrm{TN}+\mathrm{FN})}} \tag{76}$$

$$\tag{77}$$

$$\mathrm{F1} = 2\frac{\mathrm{P}\times\mathrm{C}}{\mathrm{P}+\mathrm{C}}. \tag{78}$$

The values of MCC and F1 are in the range $[0, 1]$, 1 meaning that the algorithm gives perfect predictions.

### 3.2.3 *Dependence on* $d_{th}$ *and* $\Delta z_{th}$

In this section, we vary $\Delta z_{th}$ and $d_{th}$ and, for each value, we compute the purity, the completeness, the MCC and the F1 score. We show our results in Fig. 26.

In the top panels, we show the MCC and the F1 score given the thresholds used. We marked with a dashed-black line when those metrics are at maximum. Results are similar for both cases: $\Delta z_{th} = 10^{-3}$ and $d_{th} = 100\,\mathrm{kpc}$. Interestingly, the value of 100 kpc is similar to the threshold used by observers, and it is of the order of magnitude expected: galaxies separated by 10 kpc are very likely to undergo a merging process (we remind that the radius of the disc of the Milky-Way is 10 kpc); similarly, 1000 kpc would correspond to very distant, probably non interacting, pairs. The value of $10^{-3}$ for the redshift difference, achievable with current photometric redshift (Pasquet et al., 2019), is however about one order of magnitude lower than the threshold usually chosen, typically $10^{-2}(1 + z_{pri})$. Note that, the best thresholds gives $\mathrm{F1} \sim \mathrm{MCC} = 0.6$, $\mathrm{P} = 0.54$ and $\mathrm{C} = 0.7$. This confirms our first guess of §3.2.1: using only d and $\Delta z$ is too degenerate to properly distinguish between mergers and non mergers.

For various reasons (bad weather conditions, small field of view, outdated instrument etc...), a galaxy catalog made with real observations could not achieve the optimal thresholds for projected distance or redshift difference. In this situation, it can be interesting, given the limiting thresholds in redshift difference and projected distance of the catalog, to statistically correct the number of pairs which will merge, in order to infer the merger rate for instance. It is with this goal in mind that we produced the two bottom panels in Fig. 26, showing purity (P) and completeness (C) for different $\Delta z_{th}$ and $d_{th}$. For a number $N_{obs}$ of

1 We slightly modify the definition so that MCC is in the range $[0, 1]$.

pairs selected with the thresholds $\Delta z_{th}$ and $d_{th}$, the number of true mergers (TP) should be:

$$TP = P(d_{th}, \Delta z_{th}) N_{obs} \,. \tag{79}$$

Similarly, given the corrected number of true mergers, one can use the completeness to obtain the total number of mergers:

$$\begin{aligned} N_{mergers} &= \frac{TP}{C(d_{th}, \Delta z_{th})} && (80)\\ &= \frac{P(d_{th}, \Delta z_{th}) N_{obs}}{C(d_{th}, \Delta z_{th})} \,. && (81) \end{aligned}$$

We stress here that the corrections suggested here are statistical corrections. An immediate caveat of the method is that we still do not know, for a given pair, if it will merge or not, as $d$ and $\Delta z$ do not contain enough informations. In the following Section we also consider the mass of the primary, with the idea that adding this information will help in getting more accurate results.

### 3.2.4 *Dependence on* $M_{pri}$

As explained in §3.2.1, the time needed for a merger of two galaxies of mass $M_{pri}$ and $M_{sec}$, scales with the two masses as:

$$\begin{aligned} \tau_{merger} &\propto {M_{pri}}^{1/3} {M_{sec}}^{-1} r^2 && (82)\\ &\propto {M_{pri}}^{-2/3} q^{-1} r^2 \,, && (83) \end{aligned}$$

where we introduce the mass ratio $q = M_{sec} / M_{pri}$. In our catalog, $q$ is in the interval $[0.1, 1]$ at all $M_{pri}$, therefore, at fixed distance between two galaxies, we expect a dependence of P and C with $M_{pri}$.

We select pairs with $\Delta z < 10^{-3} = \Delta z_{th}$ (our best estimate from §3.2.3) and with $M_{min} < M_{pri} < 10^{11}\ M_\odot$, $M_{min}$ varying between $10^9$ and $10^{10.5}\ M_\odot$. We then compute the purity and completeness as a function of the maximum projected distance $d_{th}$. We show an example in Fig. 27 (left). Given the simplicity of the curves, we fit them with sigmoid-like functions:

$$\begin{aligned} P(d, M_{min}) &= \frac{P_0(M_{min})}{2} \left[ \tanh\left( -\alpha_P(M_{min}) \log_{10}\left( \frac{d}{d_{0,P}(M_{min})} \right) \right) + 1 \right] && (84)\\ C(d, M_{min}) &= \frac{C_\infty(M_{min})}{2} \left[ \tanh\left( \alpha_C(M_{min}) \log_{10}\left( \frac{d}{d_{0,C}(M_{min})} \right) \right) + 1 \right] , && (85) \end{aligned}$$

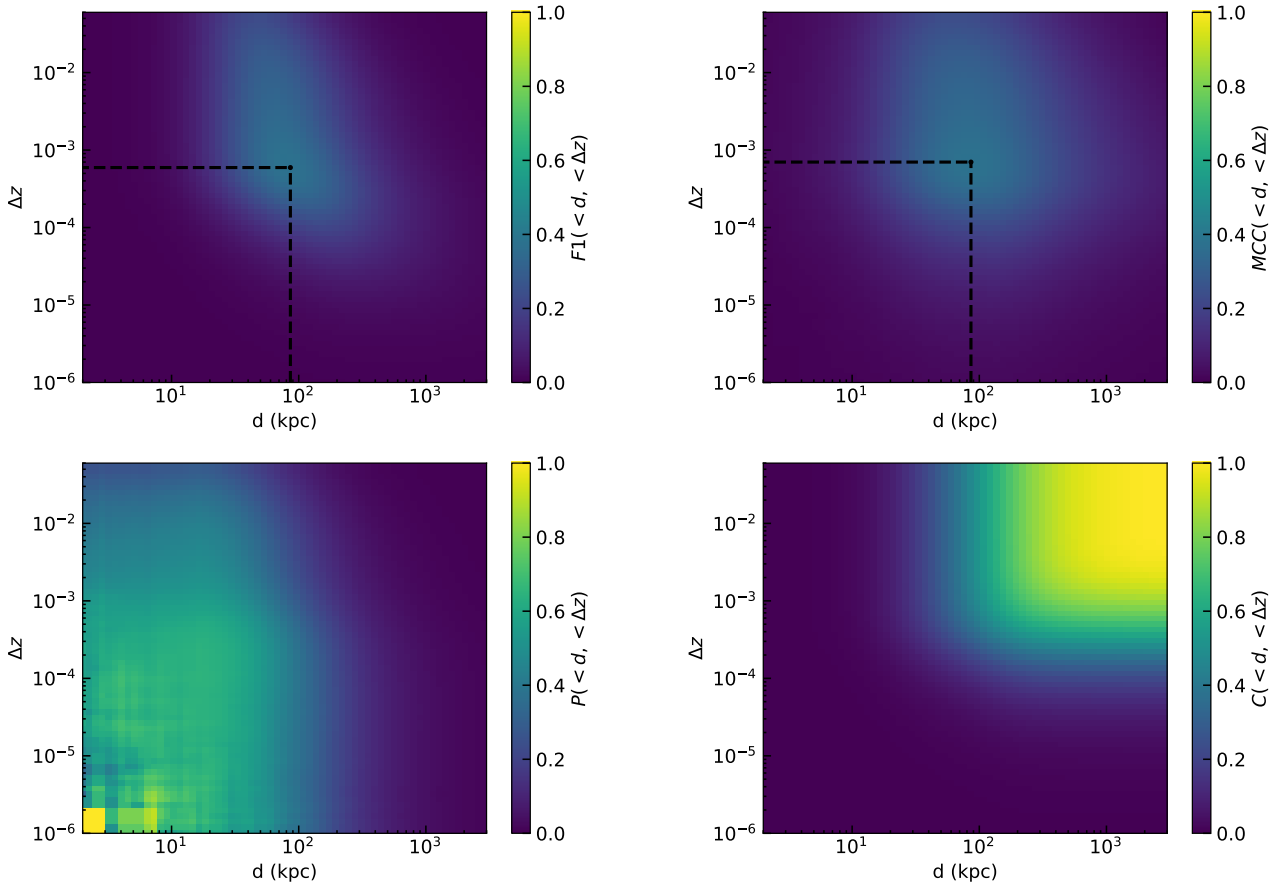


Figure 26: Effects of the cuts on redshift difference $\Delta z$ and projected distance d for estimating the fraction of pairs merging within 3 Gyr. **Top left:** F1 score. **Top right:** MCC. **Bottom left:** Purity. **Bottom right:** Completeness.

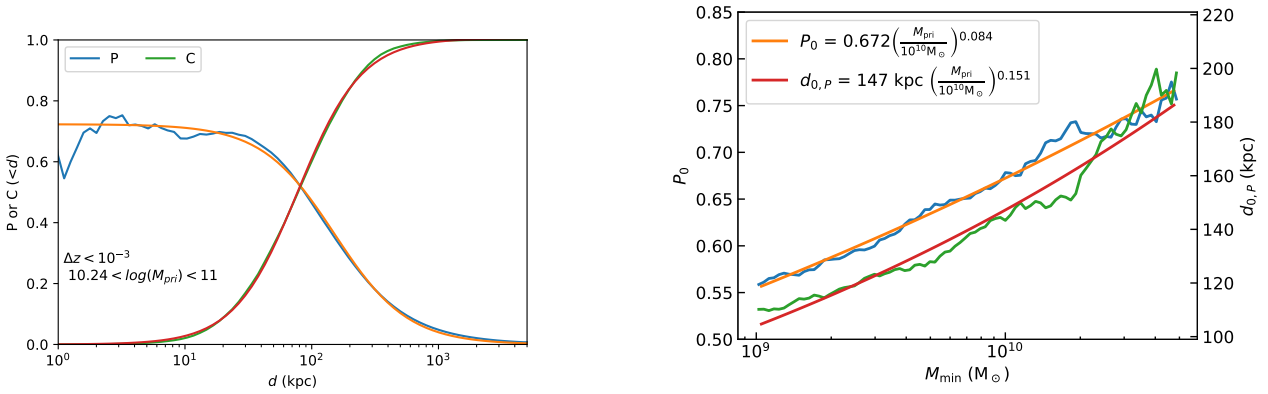


Figure 27: **Left:** Fraction of selected (P, blue line) and fraction of detected (C, green line) pairs which merge. A pair is selected if the redshift difference is lower than $10^{-3}$, if $10^{10.24}\,M_\odot < M_{pri} < 10^{11}\,M_\odot$ and if the projected distance is smaller than d. The orange and red lines are fits of the results from the simulation using Eq. (85). **Right:** Evolution of $C_0$ and $d_{0,P}$ with $M_{min}$.

all fitting coefficients being positive. As these curves are flat both at infinite and null d, $d_{0,P}$ and $d_{0,C}$ can be interpreted as the typical projected distance at which the variation between these two plateau occurs; $\alpha_P$ and $\alpha_C$ can be interpreted as the steepness of this variation (the larger the closer to a step function); $P_0$ can be interpreted as the purity when the distance is much smaller as $d_{0,P}$ and $C_\infty$ as the completeness when the distance is much greater than $d_{0,C}$.

Regarding the completeness, the values of $(C_\infty, \alpha_C, d_{0,C})$ are rather independent of $M_{min}$, with variation of less than 4%, and $(C_\infty, \alpha_C, d_{0,C}) \sim (1, 2, 78\,\mathrm{kpc})$. Regarding the purity, while $\alpha_P$ varies by only 4% ($\alpha_P \sim 1.88$), $P_0$ and $d_{0,P}$ vary respectively by 9 and 17%. We report in Fig. 27 (right) $P_0$ and $d_{0,P}$ as a function of $M_{min}$ and fit these quantities with a power law. Similarly to what presented in §3.2.3, these numbers can be used to statistically correct the number of true mergers in galaxy pairs catalogs.

In §3.1 and §3.2, we determined the fate of two distant galaxies observed in the sky. We determined the best thresholds to use to detect galaxies which will merge, and provided numbers to statistically correct the results of catalogs of real galaxies. Once the two galaxies have merged, as explained in Chapter 1, the two central BHs may find themselves in the center and form a binary. In the following we use numerical simulations to study the dynamics of BHs during and following galaxy mergers.

## 3.3 DYNAMICS OF BLACK HOLES IN A COSMOLOGICAL CONTEXT

### 3.3.1 *Numerical set-up*

We run a suite of cosmological simulations, with the code `Ramses`. Instead of running an entire box, we select a halo and put all our computational effort on this halo, this allows to obtain a reasonably good resolution, with a cosmological context and an affordable computing time, this is called a "zoom". As we are interested in understanding the evolution of BHs in typical galaxies, we chose a halo with a minor/major merger rate comparable with the typical minor/major merger rate of halos in the mass range obtained by Fakhouri, Ma, and Boylan-Kolchin, 2010 (see §3.3.1.1). The physics included in these simulations is described in Appendix 6, and we include or not our prescription for dynamical friction described in §2.3.2. Regarding the refinement strategy, we refine if $M_{DM}^{cell} + (\Omega_m/\Omega_b - 1)M_b^{cell} \geqslant 8m_{DM}$, where $M_{DM}$ and $M_b^{cell}$ are, respectively, the mass of dark matter and baryons in the cell, and $\Omega_m$ and $\Omega_b$ are the total matter and baryon density. The minimum cell size, $\Delta x$ is kept roughly constant in proper physical size with redshift: an additional level of refinement is added every time the expansion factor, $a_{exp}$, decreases by a factor of two, such that the maximum level, $l_{max}$, is reached at $a_{exp} = 0.8$. For simplicity, we further assume that

| Name | Particle dynamical friction | $\Delta x$ pc | $\Delta x_{DM}$ pc | $m_\star$ $M_\odot$ | $m_{DM}$ $M_\odot$ | $M_\bullet$ $M_\odot$ |
|---|---|---|---|---|---|---|
| LR_PD_BH1e4 | ✓ | 72 | 2300 | $2 \times 10^4$ | $2 \times 10^6$ | $10^4$ |
| MR_PD_BH1e4 | ✓ | 36 | 2300 | $2 \times 10^4$ | $2 \times 10^6$ | $10^4$ |
| HR_PD_BH1e4 | ✓ | 9 | 572 | $2 \times 10^3$ | $2 \times 10^5$ | $10^4$ |
| HR_nPD_BH1e4 | ✗ | 9 | 572 | $2 \times 10^3$ | $2 \times 10^5$ | $10^4$ |
| HR_PD_BH1e5 | ✓ | 9 | 572 | $2 \times 10^3$ | $2 \times 10^5$ | $10^5$ |
| HR_nPD_BH1e5 | ✗ | 9 | 572 | $2 \times 10^3$ | $2 \times 10^5$ | $10^5$ |

Table 6: Properties of the suite of cosmological simulations performed with the use, or not, of our model for dynamical friction described in §2.3.2. Spatial/mass resolution of the simulation. Initial mass of BHs.

$\Delta x = L_{box}/2^{l_{max}}$, where $L_{box}$ is the size of the box at redshift $z = 0$. The specifications of each simulations are described in Table 6.

#### 3.3.1.1 *Initial conditions*

We assume a ΛCDM cosmology with total matter density $\Omega_m = 0.3089$, baryon density $\Omega_b = 0.0486$, dark energy density $\Omega_\Lambda = 0.6911$, amplitude of the matter power spectrum $\sigma_8 = 0.8159$, $n_s = 0.9667$ spectral index and Hubble constant $H_0 = 67.74\,\mathrm{km\,s^{-1}\,Mpc^{-1}}$ consistent with the Planck data (Planck Collaboration et al., 2016). The initial conditions are produced with `Music` (Hahn and Abel, 2013). The box size of the simulations is $L_{box} = 73.8\,\mathrm{Mpc}$, with a coarse grid of $256^3$ dark matter particles corresponding to a dark matter mass resolution of $m_{DM,coarse} = 3 \times 10^9\,M_\odot$. A high-resolution region is defined around a halo of $M_{vir} = 10^{12}\,M_\odot$ at $z = 2$ that contains only high-resolution dark matter particles (see Table 6 for the mass of high-resolution dark matter particles in each simulation) within $2 \times r_{vir}$ ($r_{vir} = 100\,\mathrm{kpc}$). The halo is a progenitor of a group of galaxies whose mass is $M_{vir} = 7 \times 10^{12}\,M_\odot$ at $z = 0$.

#### 3.3.1.2 *Finding halos and galaxies*

We construct catalogues of haloes and galaxies using the `AdaptaHOP` halo finder (Aubert, Pichon, and Colombi, 2004), which uses an SPH-like kernel to compute densities at the location of each particle and partitions the ensemble of particles into sub-haloes based on saddle points in the density field. Haloes contain at least 200 dark matter particles. Galaxies are identified in the same way, and contain at least 200 stellar particles. We then construct a merger tree for halos and galaxies with `TreeMaker` (Tweed et al., 2009).

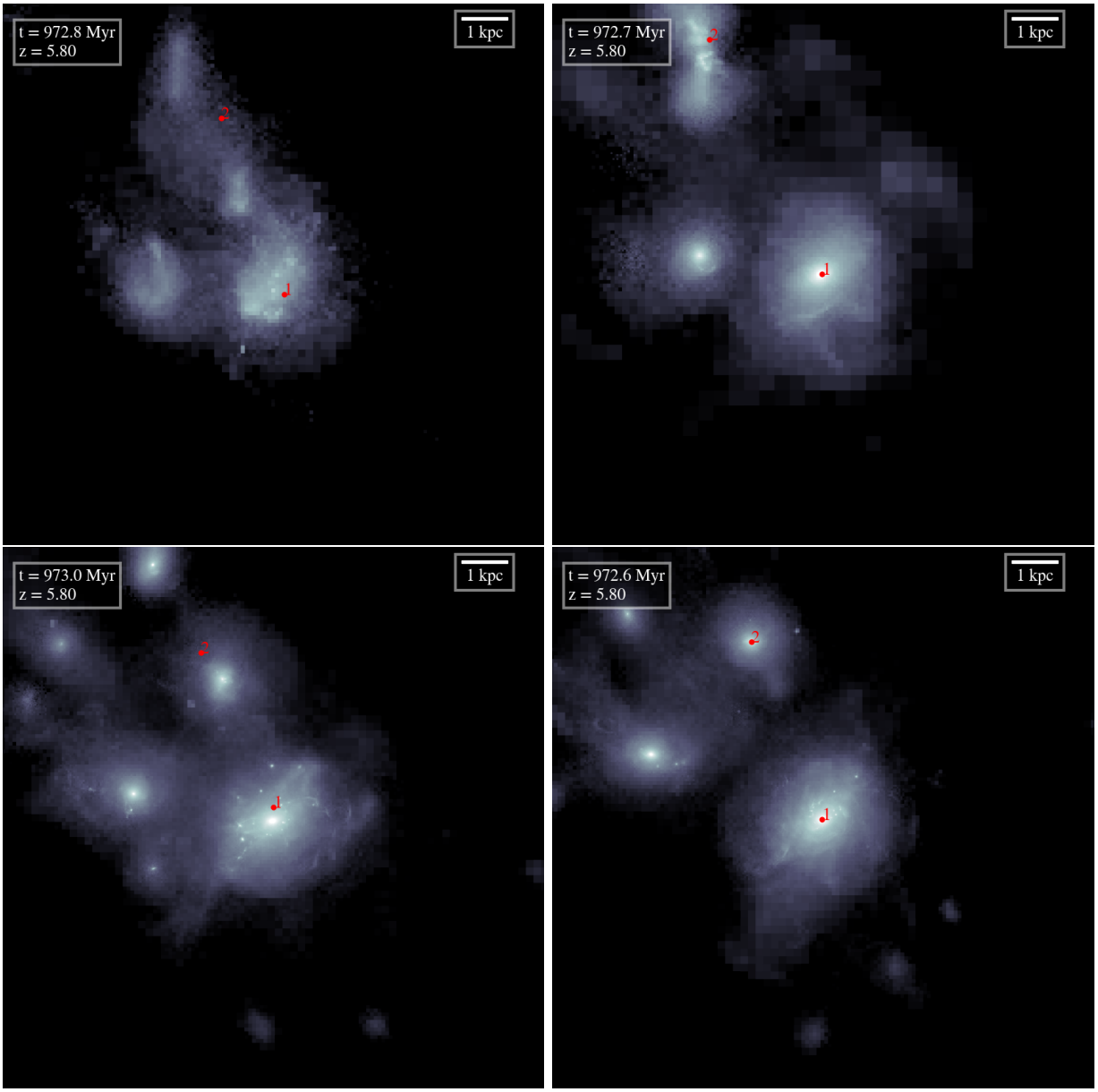


Figure 28: **Top left:** stellar density (black: $10^{-4}\,M_\odot\ pc^{-3}$, white: $1\,M_\odot\ pc^{-3}$), centered on the main galaxy with a 80 comoving kpc box size, of `LR_PD_BH1e4`. **Top right:** `MR_PD_BH1e4`. **Bottom left:** `HR_PD_BH1e4`. **Bottom right:** `HR_PD_BH1e5`. The panels show the exact same galaxy at the same time to highlight the effects of resolution. In section 3.3.2 we discuss the dynamics of a BH in the satellite galaxy on the top-left corner of each panel (the BH is highlighted in red and its ID is 2 in the four panels). In section 3.3.3 we discuss instead the interaction between this BH and the main BH in the central galaxy (also highlighted in red, and its ID is 1 in the four panels).

#### 3.3.1.3 *Estimate of the sinking time*

As done in §2.3.3.1, we consider the "sinking time", $\tau_{DF}$, defined as the time it takes for a *satellite* to sink to a *target*, using Eq. (69). To compute $\tau_{DF}$ for a BH in its own galaxy (§3.3.2), we consider that the *satellite* is the BH, for which we have the dynamical properties, and we consider that the *target* is the galaxy, for which we compute the different properties with the halo finder.

To compute $\tau_{DF}$ for a BH during a galaxy merger (§3.3.3), we have to take into account that $M_s$ evolves. Initially, the BH is surrounded by its own galaxy, which is itself surrounded by a halo, and it is the system BH+galaxy+halo that undergoes dynamical friction. Therefore, we must match BHs to galaxies and galaxies to halos to have the corrected *satellite* mass, i.e. $M_s$ is similar to the mass of the halo.

In a second phase, the dark matter halo and outer stellar layers of the secondary galaxy disperse into that of the primary, and the BH remains surrounded only by a fraction of the initial stellar mass, and we identify the evolving $M_s$ via the halo finder. Finally, the BH remains naked, and $M_s$ is the BH mass. To give an order of magnitude for this final phase, in the early universe, where galaxies have velocity dispersion as small as tens of $\mathrm{km\ s^{-1}}$, unless the BH is very massive ($\gtrsim 10^5\,M_\odot$), or surrounded by a bound dense stellar cluster, acting as if $M_{\mathrm{Satellite}}$ is larger, the sinking time is longer than Gyr if the distance to the center if larger than $\sim 100\,\mathrm{pc}$, which is likely to be the case if the BH is scattered due to anisotropies of the galaxy, either when it is in isolation or during mergers.

### 3.3.2 *Dynamics of a seed black hole in its own galaxy*

We focus on a satellite galaxy which merges with the main galaxy when the age of the Universe is about 1 Gyr. In Fig. 28 we show snapshots at the beginning of the interaction between the main galaxy, on which the figure is centered, and the satellite, to the top left of the main galaxy. This satellite hosts a BH and we study its dynamics while the galaxy is in relative isolation. This case is interesting because it explores the prospects for a seed BH to remain surrounded by dense cold gas available for growing the BH and make it observable as a faint AGN.

We start by studying how the different sources of friction (dark matter, stars and gas) contribute to the dynamical evolution. Fig. 29 presents the density in gas and stars around the BH (we do not include dark matter since its contribution is negligible). Gas is more chaotic than stars, but stars themselves do not provide a constant acceleration because they are also irregularly distributed. Beyond the sheer inhomogeneity, gas can shock, cool, inflow and outflow making its dynamical friction contribution unpredictable *a priori*. The presence of satellites also perturbs the BH orbit when it is far from the center, see Fig. 28: in a typical high-redshift environment a BH feels acceleration coming from different directions.

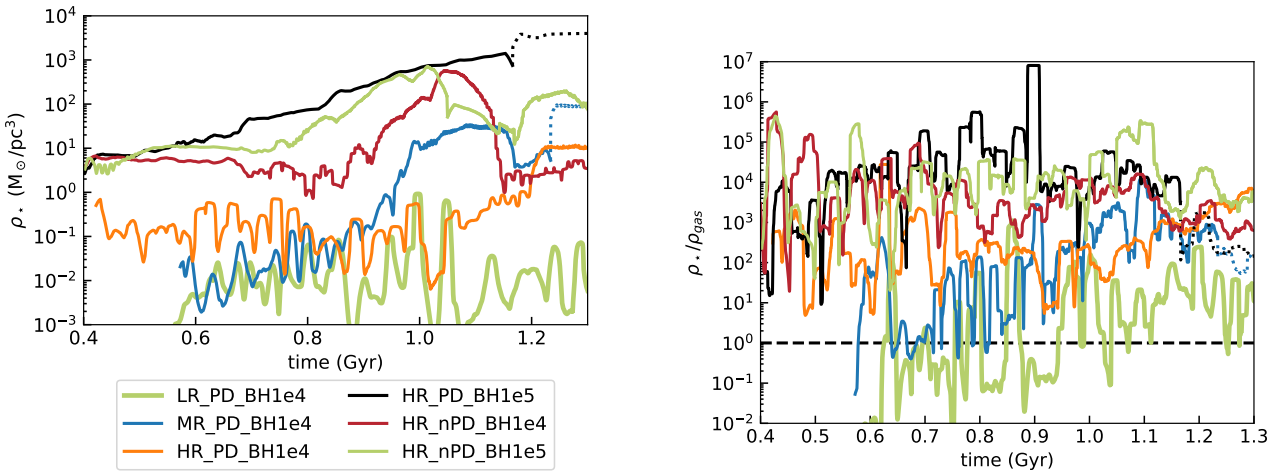


Figure 29: **Left:** mean stellar density within $4\Delta x$ around the BH in the satellite galaxy, as a function of time for a subset of the simulations listed in Table 6, as noted in the inset. **Right:** ratio of the stellar density and gas density within $4\Delta x$ around the satellite BH, as a function of time.

Moving to how this affects the BH's orbits, we show $\tau_{DF}$ as a function of time in the right panel of Fig. 30, computed for the different simulations, using the method described in §3.3.1.3. We also show in the left panel of Fig. 30 the distance of the BH to the center of its host galaxy.

Firstly, we find that, as long as the seeding mass of the BH is $10^4\,M_\odot$, all the simulations, independently of the resolution and the different models used for the BH dynamics, show a similar trend: the sinking time is, at least, 1-10 Gyr. Since in all cases $v_c$ slowly increases from 7 to 30 km s$^{-1}$ and $M_\bullet$ remains close to the BH seed mass, the reason of this large $\tau_{DF}$ is the dependency of the sinking time with the distance of the center of the galaxy, which is shown in the left panel of Fig. 30. Even in `HR_PD_BH1e4` and `HR_nPD_BH1e4`, where the BH is 5 times heavier than the star particles (those mostly contributing to the dynamical friction here) and forms at $\sim 70$ pc from the centre, it is rapidly ejected and remains hundreds of pc away from the centre. Clumps and anisotropies are observed both in the stellar and gas central distributions. Due to such irregularities in the underlying galaxy, the BH undergoes a physically-motivated random walk out of the centre of the potential well, as it also happens in lower redshift dwarfs (Bellovary et al., 2019). When the BH is more massive, $10^5\,M_\odot$, it remains in the center of its host, with a sinking time less than 100 Myr. $10^5\,M_\odot$ seems therefore to be the minimum requirement to imagine that a BH is well stabilized in the center of its host. BHs with masses lower than $10^5\,M_\odot$ are scattered within the galaxy due to irregularities of the gas/stellar potential and oscillate around the center of their host galaxies, remaining far from the dense gas regions, therefore we expect them to have low accretion rates (Smith et al., 2018) and be difficult to observe.

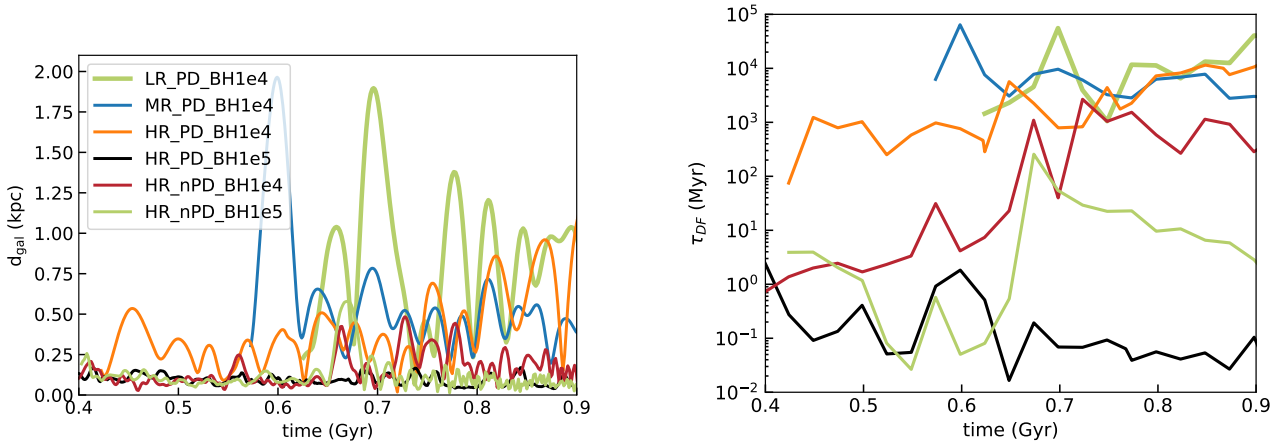


Figure 30: **Left:** distance of the BH from the center of its host galaxy, before interaction with another larger galaxy, as a function of time for all simulations listed in Table 6. **Right:** sinking time $\tau_{DF}$ for the secondary BH with respect to its host galaxy, computed using Eq. (69) (replacing $M_s$ by the mass of the BH in this equation), as a function of time.

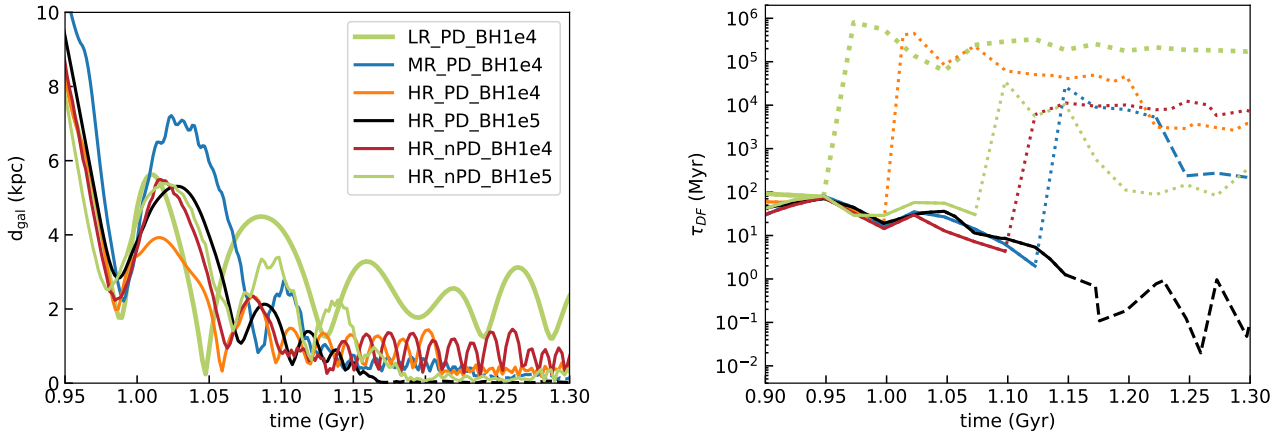


Figure 31: **Left:** distance of the BH originally in the satellite galaxy from the center of the main galaxy as a function of time for a subset of the simulations listed in Table 6, as noted in the inset. If the BH in the satellite galaxy merges with the BH of the central galaxy, we show its subsequent evolution with dashed lines. **Right:** sinking time $\tau_{DF}$, computed using Eq. (69), as a function of time. We show the different phases: when the BH is still surrounded by material (solid line), when the BH is naked (dotted line; note the rapid increase in the sinking time because of the drop in $M_s$ in Eq. (69)) and when the BH has merged with the BH of the central galaxy (dashed line).

### 3.3.3 *Formation of a black hole binary in a high-redshift galaxy merger*

We now focus on the same satellite galaxy, and follow the dynamical evolution of its BH during and after its host infalls into the halo of the larger galaxy. It is typically after this kind of event, when the galaxy remnant has settled and the massive BHs have sunk to the center of the potential well, that massive BH binaries form.

We show in Fig. 31 $\tau_{DF}$ as a function of time, for all the simulations (right panel). We see that, initially, when the BH is still embedded in the satellite galaxy (solid line), its dynamics is the same for all simulations: the large scale dynamics is independent of the subgrid model we use. However, what happens following the disruption of the satellite galaxy (dotted line) differs significantly from one simulation to the other: in some cases, the satellite BH sinks toward the center and "merges" (BHs are allowed to merge when they are separated by less than $4\Delta x$ and the kinetic energy of the binary is lower than the gravitational energy, but the real merger happens below our resolution) with the central BH of the main galaxy (the subsequent evolution is shown as a dashed line), in other cases, the BH stalls hundreds of pc away from the center. We also show in the left panel of Fig. 31 the distance of the satellite BH to the central galaxy it is sinking in.

We first compare the simulations `HR_PD_BH1e5` - `HR_nPD_BH1e5`, and `HR_PD_BH1e4` - `HR_nPD_BH1e4`, which differ only by the use or not of our subgrid model for dynamical friction from stars and dark matter. Fig. 30 shows that the model does not help in keeping BHs in the center, as discussed in §3.3.2: the galaxy is so chaotic that BHs wander no matter the implementation. When the galaxy is more settled, however, as it is the case when the satellite BH falls into the main galaxy, we see the effects of our model (see Fig. 31). When our prescription is used, the BH remains closer to the center; nonetheless the BHs do not merge as would happen if the BHs were artificially repositioned at the center of mass of the halo, as is sometimes done in cosmological simulations (*e.g.* Vogelsberger et al., 2013; Schaye et al., 2015).

We now focus on simulations with $10^4\,M_\odot$ seeds. After its stellar and gaseous envelope has been dispersed (dotted line), the BH should take 1-100 Gyr to sink toward the center of the galaxy, and indeed, it stalls at $\sim$ hundreds of pc. This is in agreement with our understanding of dynamical friction: it is a very long process if the mass of the BH is low. The presence of a nuclear star cluster could speed-up the process (Biernacki, Teyssier, and Bleuler, 2017), increasing the mass experiencing dynamical friction, but due to our limited resolution, such compact structures of typical size of a few pc to $\sim$ ten of pc are not captured here (Georgiev et al., 2016), and the envelope of the BH is rapidly stripped (dotted line). In the medium resolution case (`MR_PD_BH1e4`) the BH in the larger galaxy has also been scattered, similarly to what happened for the case studied in section 3.3.2. Accidentally, the two BHs merge while they are both off-center and the remnant of this merger remains hundreds of pc away from the center. If we admit that this merger is

physical, it is interesting to note that mergers of light seeds BHs are possible, though the dynamics is highly erratic. Multiple BHs in galaxies, each inherited from a different merger, are generically expected (*e.g.* Governato, Colpi, and Maraschi, 1994; Schneider et al., 2002; Volonteri and Perna, 2005; Bonetti et al., 2018; Tremmel et al., 2018).

Finally, we compare `HR_PD_BH1e5` and `HR_PD_BH1e4` which differ only by the seed mass of the BH. In `HR_PD_BH1e5`, the BH being more massive, it remains surrounded by a dense stellar concentration which does not disrupt (no dotted line), increasing even more the effective $M_{\text{Satellite}}$ and resulting in a smooth decay to the center of the main galaxy and a BH merger.

These experiments makes us believe that $< 10^4\,M_\odot$ seed BHs are less likely to contribute to the merging population observable by LISA than larger mass seed BHs. This does not exclude that these low-mass BHs may eventually sink in the center of galaxies and contribute to the massive BH population, but the presence of a dense stellar cluster or of bound gas on scales not resolved in this study, which would make the effective $M_{\text{Satellite}}$ larger, appears to be crucial (*e.g.* Callegari et al., 2009).

Here is a summary of the results presented in this Chapter:

- Combining different tools (mock galaxy-pair catalog extracted from a lightcone, galaxy merger tree) we obtained the best thresholds in projected distance and redshift difference to select pairs which are undergoing a merger. We found $d_{th} = 100\,\mathrm{kpc}$ and $\Delta z_{th} = 10^{-3}$. If other thresholds are used, we computed a method to correct the results and obtain the true number of mergers.

- Using a suite of cosmological zoom simulations of a $10^{12}\,M_\odot$ halo at redshift 2, we studied the dynamics of BHs in isolated galaxies, and during (following) mergers. We found that BHs with masses of the order of $10^4\,M_\odot$ are subject to the fluctuations of the underlying stellar gravitational potential, which leads to a random walk-type of trajectory. This appears to be unique of a high-z environment in which sub-structures undergo rapid evolution. If BHs were to be seeded in nuclear star clusters, or had masses of $10^5\,M_\odot$ or higher, they would be well stabilized in galaxy centres. Consequently it is unlikely that $\sim 10^4\,M_\odot$ BHs participate in the merging population unless they are embedded in dense bound stellar or gaseous envelopes. If seed BHs have larger masses ($10^5\,M_\odot$), or lighter seeds have massive bound envelopes, they can more easily reach the center of the larger galaxy and merge with the companion BH.

# 4

# TIDAL DISRUPTION EVENTS IN GALAXY MERGERS

In this Chapter we discuss how the Tidal Disruption Event (TDE) rate around BHs (see §1.4) evolves during a galaxy merger. We test the idea that galaxy mergers trigger nuclear star formation, which therefore lead to higher stellar densities near BHs and more available stars to be disrupted. We first introduce the analytical framework allowing to estimate the TDE rate from stellar density profiles. We then use a numerical simulation, where we can apply the analytical framework to obtain the TDE rate as a function of time.

This Chapter is based on the following paper:

1. Pfister et al., 2019b

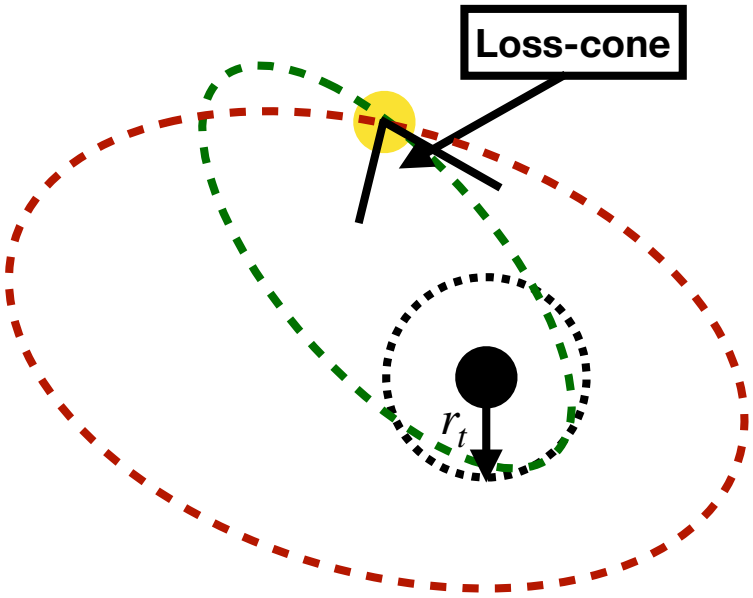


Figure 32: If the velocity vector of a star lies in the loss cone, the star will be disrupted.

## 4.1 LOSS CONE THEORY

If a star gets closer to a BH than the TDE radius $r_t$ (see Eq. (40)), it will be disrupted by tidal forces. Today, we have 90 TDE candidates (see the TDE database) while we know millions of galaxies. It is therefore natural to estimate how frequently stars penetrate this TDE radius to understand how many TDEs occur per galaxy per year and interpret this observational result.

The system we study is sketched in Fig. 32: a star orbits in a potential $\phi$, at a distance $\mathbf{r}$ and velocity $\mathbf{v}$ from the center, where a BH is located. If $\phi$ is spherically symmetric, that is, if $\phi(\mathbf{r}) = \phi(r)$, the orbit of stars is entirely defined by two orbital constants (Binney and Tremaine, 1987), the energy[1] $E$ and the angular momentum $L$:

$$E = \frac{1}{2}v^2 + \phi(\mathbf{r}) \tag{86}$$

$$L = r v_\perp , \tag{87}$$

where $v_\perp$ is the tangential velocity (see Fig. 34). If two orbits have the same energy, the angular momentum indicates how "radial" is the orbit, see Fig. 32 for two orbits with higher/lower angular momentum, and therefore more/less radial. Consequently, at fixed energy, there is a maximum angular momentum $L_{lc}$ (see §4.1.1 for the expression of $L_{lc}$) that stars can have to be disrupted, and their velocity vector has to lie in a cone (the "loss cone"). This justifies the name of the analytical framework that we will develop here: the loss cone theory.

1 We use the energy and angular momentum per unit mass as done by dynamicists.

Assume for a moment that we are able to estimate how many stars $N_{lc}(E)dE$ have an energy $E$ in $[E, E+dE]$ and an angular momentum $L < L_{lc}$ (see §4.1.2). In this situation, all stars will be disrupted after an orbital period[2] $P(E)$. If we assume that these stars are replaced instantaneously after being disrupted by the BH, the loss cone is always full: this is the full loss cone regime. In this situation, the rate at which stars with energy in $[E, E+dE]$ are disrupted is:

$$\mathcal{F}_{\rm full}(E)dE = \frac{N_{lc}(E)}{P(E)}dE\,, \tag{88}$$

where we introduce the TDE rate flux coming from the full loss cone regime $\mathcal{F}_{\rm full}$.

This regime clearly breaks down if the timescale for replacing stars is much longer than the orbital period, in this situation the loss cone is always empty: this is the empty loss cone regime. A way to repopulate the loss cone is through 2–body encounters (see Appendix 7), which deviate stars from one orbit to the other, varying the angular momentum dispersion of stars by $\Delta(L^2) \sim L^2$ on a relaxation timescale $T_r$ (see §4.1.3). If we denote the number of stars with energy in $[E, E+dE]$ by $N(E)dE$, as on a relaxation timescale the angular momentum varies by $\sim L$, the condition $L < L_{lc}$ is no longer needed and the TDE rate at which stars with energy in $[E, E+dE]$ are disrupted is:

$$\mathcal{F}_{\rm empty}(E)dE = \frac{N(E)}{T_r(E)}dE\,, \tag{89}$$

where we introduce the TDE rate flux coming from the empty loss cone regime $\mathcal{F}_{\rm empty}$.

The total TDE rate $\Gamma$ is given by the contribution of both the empty and full loss cone regimes:

$$\Gamma = \int \mathcal{F}_{\rm empty}(E)dE + \int \mathcal{F}_{\rm full}(E)dE \tag{90}$$

$$= \Gamma_{\rm empty} + \Gamma_{\rm full}\,. \tag{91}$$

In the following we obtain the analytical expression of $L_{lc}$, $N(E)$, $N_{lc}$, $T_r$ to compute the TDE rate both in the empty and full loss cone regime, $\Gamma_{\rm empty}$ and $\Gamma_{\rm full}$.

### 4.1.1 *Expression of the maximal angular momentum*

From Eq. (86) and using that $\phi$ vanishes at $r = +\infty$, we find the classical result that if $E < 0$ then the orbit cannot go to infinity: it is bound. We will focus on these orbits from now on, as galaxies form gravitationally bound systems. We define the pericenter (apocenter) $r_\pm(E, L)$ as the minimum (maximum) distance of the star to the BH, they depend on the

2 We neglect here the dependence on $L$ of the orbital period. We discuss this in §4.1.2.

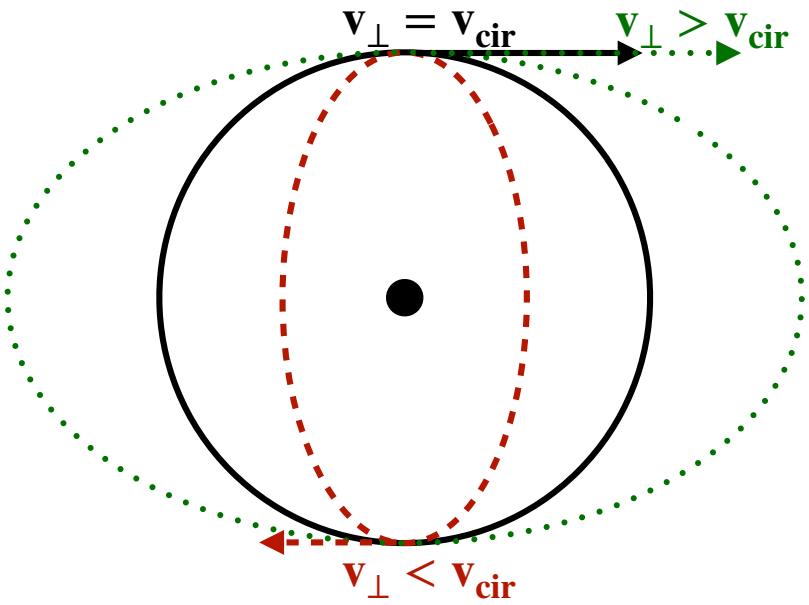


Figure 33: Three orbits in a spherically symmetric potential with, at the center, a BH. If $v_\perp < v_{cir}$ (red orbit) the pericenter of the orbit is closer to the center than the radius of the circular orbit (black orbit), and vice versa. Consequently, at pericenter we necessarily have $v_\perp \geqslant v_{cir}$.

orbit, therefore depend on $E$ and $L$. At these radii the radial velocity vanishes and we obtain the following equations:

$$E = \frac{1}{2}v_\perp^2 + \phi(r_\pm(E,L)) \tag{92}$$

$$E = \frac{L^2}{2r_\pm^2(E,L)} + \phi(r_\pm(E,L)) \tag{93}$$

$$\Leftrightarrow \quad L^2 = 2r_\pm^2(E,L)\left(E - \phi(r_\pm(E,L))\right) . \tag{94}$$

Instead of considering constant $E$ and $L$, we can equivalently consider constant $E$ and $r_-$. We have that:

$$L^2(r_-,E) \;=\; 2r_-^2(E-\phi(r_-)) . \tag{95}$$

To obtain the variations of $L$ with $r_-$, we compute:

$$2L\frac{dL}{dr_-} \;=\; 4r_-(E-\phi(r_-)) - 2r_-^2\frac{d\phi}{dr_-} \tag{96}$$

$$\;=\; \frac{2L^2}{r_-}\left(1-\left(\frac{v_{cir}(r_-)}{v_\perp(r_-)}\right)^2\right) , \tag{97}$$

where $v_{cir}(r_-) = (r_-\phi'(r_-))^{1/2}$ is the speed of a circular orbit at $r_-$. Clearly, at pericenter, $v_\perp \geqslant v_{cir}$ (see Fig. 33). Consequently, $L$ is an increasing function of $r_-$ and, at fixed energy,

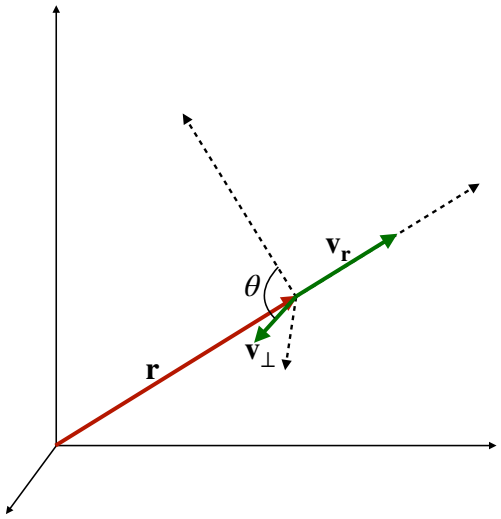


Figure 34: Convention used to define the velocity vector. $\mathbf{v_r}$ is in the same direction as $\mathbf{r}$ and $\mathbf{v}_\perp$ is orthogonal to $\mathbf{r}$.

we can define a critical angular momentum $L_{lc}(E)$ so that if $L < L_{lc}$, then $r_- < r_t$ and the star is disrupted. $L_{lc}(E)$ is obtained when the orbit skims the TDE radius and $r_- = r_t$, that is:

$$L_{lc}^2 = 2r_t^2(E - \phi(r_t)) \tag{98}$$

$$\sim 2G\, M_\bullet\, r_t\,, \tag{99}$$

where we have assumed for the last equality that the potential at $r_t$ is dominated by the BH (we recall that $r_t$ is 100 solar radii for a $10^6\,M_\odot$ BH, much smaller than galaxy scales), and that the energy of the orbit is negligible against $\phi(r_t)$, that is, the star is marginally bound.

### 4.1.2 *Number of stars per orbits*

To compute the number of stars with energy in $[E, E + dE]$, we further assume that the distribution function is ergodic and therefore can be expressed only as a function of $E$. The number of stars in $[\mathbf{r}, \mathbf{r} + d\mathbf{r}]$ and $[\mathbf{v}, \mathbf{v} + d\mathbf{v}]$ is:

$$f(E)d\mathbf{r} \times d\mathbf{v}\,. \tag{100}$$

By first integrating onto the polar and azimuth angle in position, we classically find:

$$f(E)4\pi r^2 dr \times d\mathbf{v}\,. \tag{101}$$

Using the notations defined in Fig. 34, we have[3]:

$$f(E)4\pi r^2 dr \times v_\perp \sin(\theta) d\theta dv_\perp dv_r \,, \tag{102}$$

which can be integrated over $\theta$ to obtain:

$$f(E)4\pi r^2 dr \times 2\pi v_\perp dv_\perp dv_r \tag{103}$$

$$= \quad f(E)8\pi^2 r^2 v_\perp \times dr dv_\perp dv_r \,. \tag{104}$$

We now perform the variable change $(r, v_r, v_\perp) \mapsto (r, E, L)$, for which the Jacobian is $rv_r$, leading to:

$$f(E)8\pi^2 r^2 v_\perp \times \frac{dr dE dL}{r v_r} \tag{105}$$

$$= \quad f(E)8\pi^2 L dE dL \times \frac{dr}{v_r} \,, \tag{106}$$

which can be integrated[4] over $r$ to obtain:

$$f(E)8\pi^2 L dE dL \times \int_{r_-}^{r_+} \frac{dr}{v_r} \tag{107}$$

$$= \quad f(E)8\pi^2 L dE dL \times P(E, L) \,, \tag{108}$$

where we introduce the radial period, corresponding to the time needed to go from $r_+$ to $r_-$ or, symmetrically, from $r_-$ to $r_+$. For the isochrone density profile (Binney and Tremaine, 1987), $P$ does not depend on $L$. As this profiles is fairly close to that of giant galaxies, we shall neglect the dependence of $P$ on $L$.

Eq. (108) can be integrated over $L$ to obtain the energy density function $N$, for which $N(E)dE$ corresponds to the number of stars with energy in $[E, E + dE]$. Given that the maximal angular momentum[5] at fixed $E$ is $L_{cir}$, the circular angular momentum at $r_{cir}$, where $r_{cir}$ is solution to:

$$E = \frac{r_{cir}(E)}{2} \frac{d\phi}{dr}(r_{cir}(E)) + \phi(r_{cir}(E)) \,, \tag{109}$$

we have that:

$$N(E) \quad = \quad f(E)8\pi^2 P(E) \int_0^{L_{cir}(E)} L dL \tag{110}$$

$$= \quad f(E)4\pi^2 L_{cir}^2(E) P(E) \,. \tag{111}$$

3 $\theta$ is not the angle in position space, but in the velocity space.

4 For fixed $E$ and $L$, $r$ varies between pericenter and apocenter $r_\pm$.

5 This comes from the fact that $L$ increases with $r_-$, but decreases with $r_+$ (see Eq. (97) and Fig. 33). As $r_+ \geqslant r_-$, the angular momentum is maximum when the two radii are equal, *i.e.* the orbit is circular.

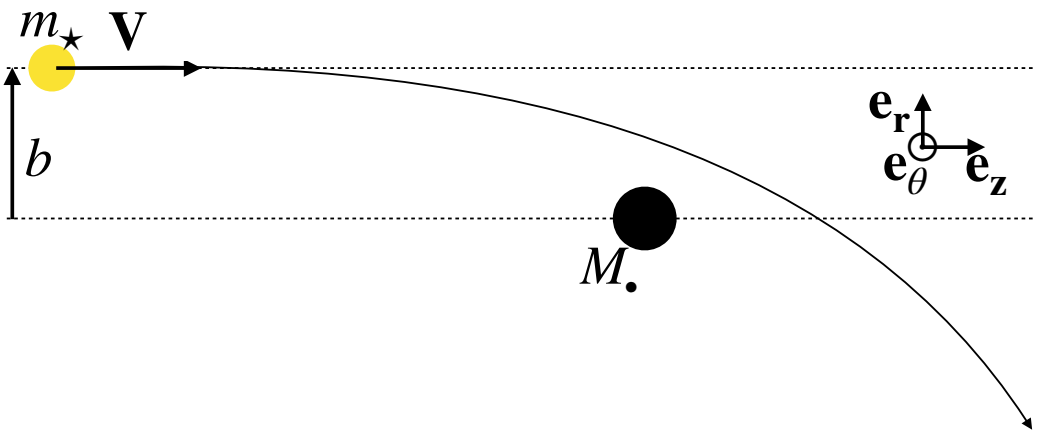


Figure 35: Sketch of a hyperbolic encounter, geometry used is cylindrical.

Similarly, the number of stars[6] with $L < L_{lc}$ and energy in $[E, E + dE]$ is:

$$N_{lc}(E) = f(E) 4\pi^2 L_{lc}^2 P(E) dE \,. \tag{112}$$

### 4.1.3 *Relaxation time*

As the potential is in reality not smooth on all scales, two-body interactions, as discussed in Appendix 7 can greatly affect the trajectory. If two stars with the same mass $m_\star$, one moving with velocity $\mathbf{v}_\bullet$ and the other with velocity $\mathbf{v}_\star$, suffer a hyperbolic encounter with impact parameter $b$ and initial relative velocity $\mathbf{V} \equiv \mathbf{v}_\star - \mathbf{v}_\bullet$ (See Fig. 35), the change in $\mathbf{v}_\bullet$ is given by Eq. (213):

$$\Delta \mathbf{v}_\bullet = \left[1 + \frac{b^2 V^4}{4 G^2 m_\star^2}\right]^{-1} V \left(\frac{b V^2}{2 G m_\star} \mathbf{e_r} + \mathbf{e_z}\right) \,. \tag{113}$$

In §2.1 we discussed the effects of many encounters and showed how they lead to dynamical friction, we further mentioned that, for symmetry reasons, on average, the net effect on the $\mathbf{e_r}$ axis is zero. However, we can easily imagine that the distribution will broaden due to many encounters, and we instead look at $\langle (\Delta v_{\bullet,\perp})^2 \rangle$, the rate at which $(\Delta \mathbf{v} \cdot \mathbf{e_r})^2$ vary. For a constant number density $n$, the encounter rate with impact parameters in $[b, b + db]$

6 We consider here orbits with $L_{cir} > L_{lc}$, i.e., for which the orbit's apocenter is outside the TDE radius which, we recall, is very small on galactic scales.

is $nV \times 2\pi b db$ so that the total effect, considering all stars with $b < b_{max}$ (the size of the system) is:

$$\langle (\Delta v_{\bullet,\perp})^2 \rangle = \int_0^{b_{max}} \left[ \left[ 1 + \frac{b^2 V^4}{4 G^2 m_\star^2} \right]^{-1} V \frac{b V^2}{2 G m_\star} \right]^2 n V 2\pi b db \tag{114}$$

$$= \frac{4\pi G^2 m_\star^2 n}{V} \left[ -1 + \frac{1}{1 + \left( \frac{b_{max} V^2}{2 G m_\star} \right)^2} + \ln \left[ 1 + \left( \frac{b_{max} V^2}{2 G m_\star} \right)^2 \right] \right] . \tag{115}$$

For stars with masses $m_\star = M_\odot$ in a system with size $b_{max} = 1\,\mathrm{kpc}$, $b_{max} V^2/(G m_\star) > 100$ if $V > 20\,\mathrm{m\,s^{-1}}$, which is likely to be the case. We can therefore Taylor expand in $b_{max} V^2/(G m_\star)$, this yields:

$$\langle (\Delta v_{\bullet,\perp})^2 \rangle \sim \frac{8\pi G^2 m_\star^2 n}{V} \ln \left( \frac{b_{max} V^2}{G m_\star} \right) . \tag{116}$$

The timescale $T_r$ needed to vary $(\Delta \mathbf{v}_\bullet \cdot \mathbf{e_r})^2$, which equals the velocity dispersion $\sigma^2$, by order unity is:

$$T_r = \frac{\sigma^2}{\langle (\Delta v_{\bullet,\perp})^2 \rangle} \tag{117}$$

$$= \frac{\sigma^3}{8\pi G^2 m_\star^2 n} \ln^{-1} \left( \frac{b_{max} V^2}{G m_\star} \right) \tag{118}$$

$$= 50\,\mathrm{Gyr} \left( \frac{\sigma}{200\,\mathrm{km\,s^{-1}}} \right)^3 \left( \frac{m_\star}{M_\odot} \right)^{-2} \left( \frac{n}{\mathrm{pc^{-3}}} \right)^3 \ln^{-1} \left( \frac{b_{max} V^2}{G m_\star} \right) . \tag{119}$$

This time corresponds to the time needed for two-body encounters to alter significantly the initial orbit so that memory of the initial conditions is erased, in other words, to move from one orbit to another orbit: this is the non-resonant relaxation timescale. This time can be much longer than a Hubble time in galaxies where the typical density is less than 1 star per cubic pc (justifying the use of the mean field approach in this case), however, in very dense regions such as in the nuclei of galaxies or in globular clusters, two-body interactions become extremely important.

Note that other effects modify the dynamics of stars in the nucleus of galaxies: the relativistic precession of the periastron due to the central BH, or resonant relaxation caused by the cumulative torque due to other stars (Rauch and Tremaine, 1996; Merritt, 2013). Rauch and Ingalls, 1998 studied the effects of these processes and found that, in the optimal situation, the loss cone is refilled twice faster, *i.e.* the TDE rate is twice larger, than in the situation including non-resonant relaxation. They also found that, given the observed properties of galactic nuclei, this optimal situation is rarely reached. For this reason we do not consider these processes for the rest of this Thesis.

### 4.1.4 *Empty/full loss cone regime and toward a better estimate of the tidal disruption event rate*

The framework developed in the previous section leads to an estimate of the TDE rate fluxes and integrating over the energy we obtain the TDE rate. From Eq. (88), Eq. (89), Eq. (111), Eq. (112) and Eq. (118), we have:

$$\mathcal{F}_{\rm empty}(E) = f(E) 4\pi^2 L_{\rm cir}^2 \frac{P(E)}{T_r(E)} \tag{120}$$

$$\mathcal{F}_{\rm full}(E) = f(E) 4\pi^2 L_{\rm lc}^2 \,, \tag{121}$$

and the critical energy (radius) $E_c = \phi(r_c)$ at which the two regimes match is when their contribution to the TDE rate flux is the same, *i.e.* $\mathcal{F}_{\rm empty} = \mathcal{F}_{\rm full}$. This yields[7]:

$$\frac{1}{3} r_\star \left(\frac{M_\bullet}{m_\star}\right)^{4/3} = \frac{G M(r_c)}{\sigma(r_c)^2} \,, \tag{122}$$

where we dropped the logarithmic term for the relaxation timescale (see Eq. (118)) which is usually $< 10$, assumed $L = r\sigma$, $P = r/\sigma$ and defined $M(r) = 4/3\pi r^3 m_\star n(r)$ the enclosed mass within $r$.

The TDE rate coming from the empty loss cone regime, *e.g.* Wang and Merritt, 2004, is:

$$\Gamma_{\rm empty} = \int_{-\infty}^{E_c = \phi(r_c)} \mathcal{F}_{\rm empty}(E) dE \tag{123}$$

$$\sim \frac{M(r_c)}{T_r(r_c) m_\star} \,, \tag{124}$$

7 The equation for $r_c$ is slightly different than Eq.(6) from Pfister et al., 2019b as we use the relaxation timescale we derived in §4.1.3 instead of the one obtained through the diffusion coefficients (Spitzer and Harm, 1958).

and from the full loss cone regime, *e.g.* Pfister et al., 2019b:

$$\begin{aligned}
\Gamma_{\rm full} &= \int_{E_c}^{\infty} \mathcal{F}_{\rm full}(E)dE && (125)\\
&= \int_{E_c}^{\infty} f(E)4\pi^2 L_{\rm lc}^2 dE && (126)\\
&= 4\pi^2 L_{\rm lc}^2 \int_{E_c}^{\infty} f(E)\nu\frac{dE}{\nu} && (127)\\
&= 4\pi^2 L_{\rm lc}^2 \int_{0}^{\infty} f\left(\frac{v^2}{2}+E_c\right)\nu dv && (128)\\
&= 4\pi^2 L_{\rm lc}^2 \int_{0}^{\infty} f\left(r_c,v\right)\nu dv && (129)\\
&= \pi L_{\rm lc}^2 \int_{0}^{\infty} f\left(r_c,v\right)\nu^{-1}4\pi v^2 dv && (130)\\
&= \pi L_{\rm lc}^2 \int f\left(r_c,v\right)\nu^{-1} d\mathbf{v} && (131)\\
&= \pi L_{\rm lc}^2 \langle \nu^{-1}\rangle(r_c)\rho(r_c)m_\star^{-1} && (132)\\
&\sim \sqrt{8\pi}\,G\,r_\star \left(\frac{M_\bullet}{m_\star}\right)^{4/3} \sigma(r_c)^{-1}\rho(r_c) && (133)
\end{aligned}$$

where $\langle . \rangle$ is the mean over velocity and we have used Eq. (40), Eq. (99) and $\langle \nu^{-1}\rangle \sim \sqrt{2/\pi}\sigma^{-1}$.

More details works (Cohn and Kulsrud, 1978; Wang and Merritt, 2004; Merritt, 2013; Stone and Metzger, 2016; Vasiliev, 2017), resolving the Fokker-Planck equation in particular regimes and fitting N-body simulations, provide a more accurate estimate of the total TDE rate per unit energy:

$$\mathcal{F}(E) = \frac{N(E)}{P(E)} \frac{q(E)L_{\rm lc}^2/L_{\rm cir}^2}{(q(E)^2+q(E)^4)^{1/4}+\ln(L_{\rm cir}^2/L_{\rm lc}^2)}\,. \tag{134}$$

$q$ is the loss cone filling factor defined as:

$$q(E) = P(E)D(E)L_{\rm cir}^2/L_{\rm lc}^2\,, \tag{135}$$

and $D$ is the orbit average diffusion coefficient in angular momentum defined as:

$$D(E) = \frac{1}{P(E)L_{\rm cir}^2}\int_0^{r_{\rm max}(E)} \frac{dr}{v_r}\langle(\Delta L)^2\rangle\,, \tag{136}$$

where $\langle(\Delta L)^2\rangle = \langle(\Delta(r v_\perp))^2\rangle = r^2\langle(\Delta v_\perp)^2\rangle$ corresponds to the rate at which $L^2$ vary (similar as §4.1.3, see Appendix C from Bar-Or and Alexander, 2016), and $r_{\rm max}$ is defined as $\phi(r_{\rm max}(E)) = E$.

## 4.2 TIDAL DISRUPTION EVENTS IN POST STARBURST GALAXIES

### 4.2.1 *Observations*

While the number of TDE candidates is still fairly low (90 currently reported in the TDE database), various authors have attempted to study the properties of the host galaxies of TDEs.

We show in Fig. 36 (left) a density map of galaxies (blue for star forming and red for quiescent) in the plane "Current SFR–past SFR" and indicate galaxies hosting TDEs with white markers. Galaxies are selected from the $12^{\text{th}}$ data release of the SDSS, which consists of $\sim 9 \times 10^5$ galaxies observed over $\sim 10^4 \text{deg}^2$ to a limiting magnitude of 17.77. Additional quality cuts are made: redshift range in $[0.01, 0.2]$, good H$\alpha$ fit, good velocity dispersion measurement, good stellar mass measurement, good diameter measurement and no evidence of AGN resulting in a sample of 443 023 galaxies (see details in Graur et al., 2018). TDEs included are both optically/UV (Arcavi et al., 2014) or X-rays (Auchettl, Guillochon, and Ramirez-Ruiz, 2017) selected.

In this sample, 22 out of 35 (63%) of TDEs are hosted in red quiescent galaxies with a low ($< 3$Å) H$\alpha$ EW emission. To be more precise, Law-Smith et al., 2017 finds that TDE hosts usually fall within 1 dex below the main sequence of star-forming galaxies (Peng et al., 2010), but *"recognize that there could be a bias against TDE identification in star–forming galaxies"* as large column densities of gas and dust could prevent the observation of the central region of blue star forming galaxies (Blain et al., 1999). Whether this is an observational bias or a physical result is still debated and will become clearer when more observations are available.

Galaxies in the dark–grey bottom right hand are E+A galaxies, have no current star formation and undergone a starburst within 1 Gyr (see Fig. 36, right). They represent 0.3% of the galaxy sample but 6/35 (17%) of TDE hosts fall in this region, implying an overrepresentation of more than a factor of 50. Stone and van Velzen, 2016 performed a modeling of an E+A galaxies observed with exquisite resolution with the Hubble Space Telescope. They applied the loss cone formalism, which we broadly described in §4.1, to infer the TDE rate, and found about $10^{-3}\,\text{yr}^{-1}$: one or two orders of magnitude larger than in typical galaxies (Auchettl, Ramirez-Ruiz, and Guillochon, 2018). This enhancement is due to an anomalously high central stellar density (see Eq. (133)) caused by the recent starburst. This result is to a certain degree confirmed statistically: Graur et al., 2018 find a global enhancement of the TDE rate with the stellar surface mass density, and Law-Smith et al., 2017 find higher Sersic indices and bulge–to–total–light ratios, *i.e.* steeper and denser profiles, in galaxies hosting TDEs.

Galaxy mergers are a natural way to trigger nuclear starbursts through gas inflows due to tidal forces and ram-pressure shocks (Mihos and Hernquist, 1996; Bournaud, 2011). Differ-

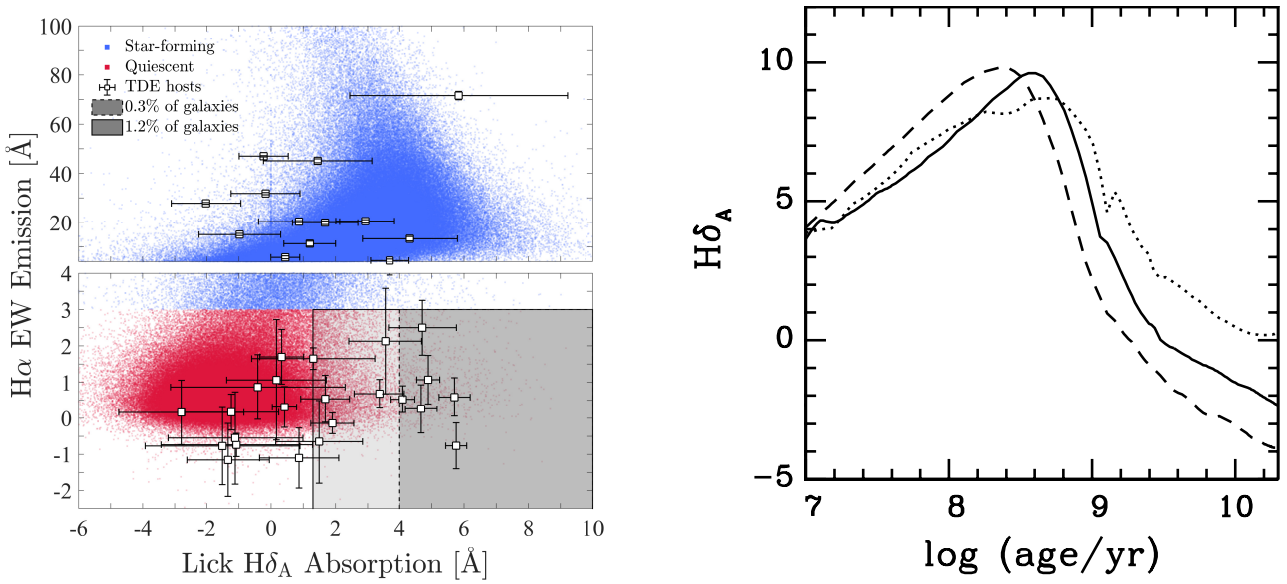


Figure 36: **Left:** Galaxies in the plane "Current SFR–past SFR" (blue for star forming and red for quiescent) and galaxies hosting a TDE (white squares). Most galaxies have a current low SFR and there is an over-representation of E+A galaxies with no current SFR but with a recent starburst. Taken from Graur et al., 2018. **Right:** Evolution of $H\delta_A$ following a starburst with three different metallicities. E+A galaxies have undergone a starburst within 1 Gyr. Taken from Kauffmann et al., 2003.

ent groups with different codes (Di Matteo et al., 2008; Van Wassenhove et al., 2014; Capelo et al., 2015) performed suites of ideal simulations of galaxy mergers, and they found that multiple starbursts lasting 10-100 Myr occur during the mergers and can enhance the central stellar density by orders of magnitude. Yang et al., 2008 analyzed a sample of E+A galaxies and found that at least 55% of them show dramatic tidal features indicative of mergers. More recently, Baron et al., 2018 found interacting pairs in which the larger galaxy is of E+A type. This suggests that, in the final stages of a galaxy merger, it is possible that one of the two galaxies, or the merger remnant, are of E+A type with a TDE rate enhanced by few orders of magnitude. For this reason, we study in the following the evolution of the TDE rate during a galaxy merger.

### 4.2.2 *Comparison with a simulation*

#### 4.2.2.1 *Numerical set-up*

**Simulation** We perform a zoom re-simulation of the 1:4 coplanar, prograde–prograde galaxy merger from Capelo et al., 2015, which was shown to have a strong burst of nuclear star formation (see also Van Wassenhove et al., 2014), and is adopted here as a reference merger to highlight the various physical processes responsible for the evolution of the nucleus. Similar bursts were also observed in mergers with mass ratio 1:2 (coplanar and

inclined orbital configurations), whereas lower mass-ratio mergers had weaker (1:6 case) or negligible (1:10) nuclear starbursts. Initially BH1, with a mass of $3.53 \times 10^6\,M_\odot$, is in the main galaxy, whereas BH2, with a mass of $0.88 \times 10^6\,M_\odot$, is in the secondary galaxy.

We re-simulate the merger phase (see Capelo et al., 2015), which begins at the second pericentre, at $t \sim 1\,\mathrm{Gyr}$, and lasts until the binary BH has formed, 300 Myr later. It is during this phase that the starburst occurs and we expect variations in the density and, consequently, in the TDE rate.

This re-simulation (`Resim0`) is performed with the public code `Ramses` (Teyssier, 2002 and described in Appendix 6)

The mass of DM particles ($m_{DM} = 1.1 \times 10^5\,M_\odot$) and stellar particles ($3.3 \times 10^3\,M_\odot$) is kept similar to that in Capelo et al., 2015 but we allow for better spatial resolution (down to $\Delta x = 0.76\,\mathrm{pc}$), refining the mesh where $M_{DM}^{cell} + 10M_b^{cell} \geqslant 8m_{DM}$, where $M_{DM}$ and $M_b^{cell}$ are, respectively, the mass of DM and baryons in the cell. Maximum refinement is enforced within $4\Delta x$ around the BHs.

**TDE rate** We measure the stellar density profiles around BHs for each snapshot in our simulation and fit them with a double power-low profile $\rho(r) = \rho_0 r^\gamma (1 + r/r_0)^{\beta-\gamma}$. We then pass these density profiles to the `PhaseFlow` code (included in `Agama`; Vasiliev 2017; Vasiliev 2019) which computes the distribution function $f(E)$ from the density profile (through the Eddington inversion, see Binney and Tremaine, 1987) and the loss cone filling factor $q(E)$ (see Eq. (135)). The `PhaseFlow` code is conceived to solve the time dependent Fokker-Planck equation, but we only use it to estimate $f$ and $q$ at each timestep corresponding to a snapshot of the simulation.

We then use Eq. (134) to compute the TDE rate per unit energy, which can be integrated to obtain the TDE rate $\Gamma$, defined as number of events per galaxy per year. In Fig. 37, we show an example of TDE rate per unit radius ($\partial\Gamma/\partial r = \partial\Gamma/\partial E \times \partial E/\partial r = \mathcal{F} \times \partial E/\partial r$) as estimated from `PhaseFlow` (solid black line). We also show the two approximated fluxes in the full and empty loss cone regime (blue and purple lines) as computed with Eq. (88) and Eq. (89), and their harmonic mean (red dashed line). Note how the harmonic mean gives excellent results given the simplicity of the calculation. We did not explore this much, though it could be an accurate and fast method to compute the TDE rate.

We can also estimate the critical radius/energy solution to $\mathcal{F}_{full} = \mathcal{F}_{empty}$ (vertical dashed black line in Fig. 37), and show its evolution in Fig. 38. It is about 20 pc at all times for BH1, and is initially 13 pc for BH2, but drops to 4-5 pc after the starburst (see §4.2.2.2).

#### 4.2.2.2 *Results*

**Nuclear starburst** In Fig. 39, we show stellar density maps of our simulation. In Fig. 40, we show the enclosed stellar mass around each BH as a function of time, for different radii in the re-simulation. It is clear from Fig. 40 that the primary galaxy is not affected by the

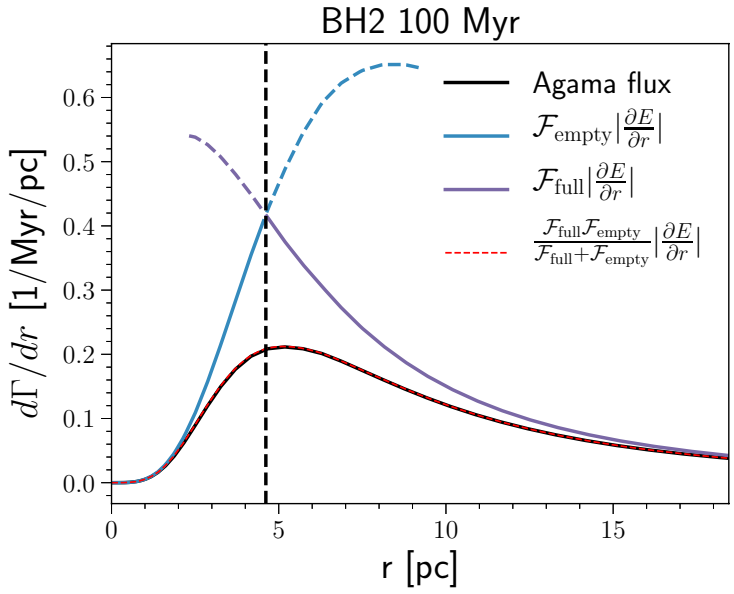


Figure 37: TDE rate per unit radius as estimated from `PhaseFlow` (black solid line), in the full and empty loss cone regimes (blue and purple lines), and the harmonic mean between the full and empty loss cone regimes (red dashed line). We also show when the full and empty loss cone rates match, *i.e.* the critical radius $r_c$ (vertical black dashed line).

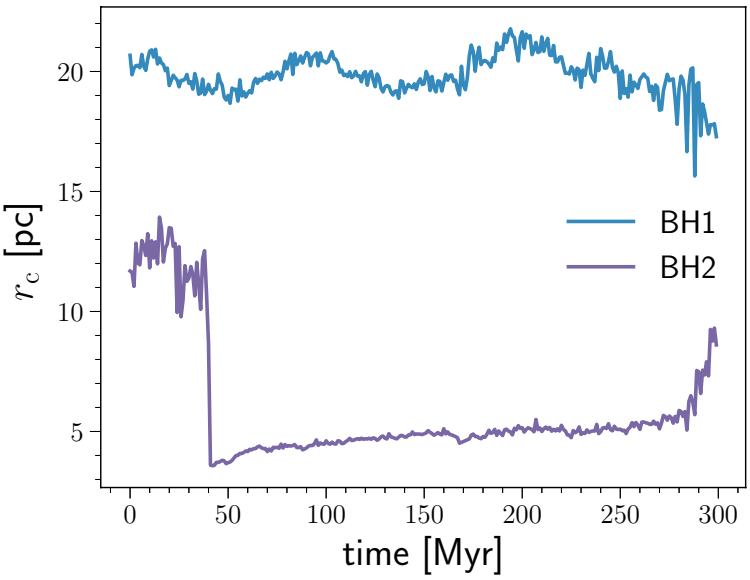


Figure 38: Evolution of the critical radius with time for the two BHs in our simulation.

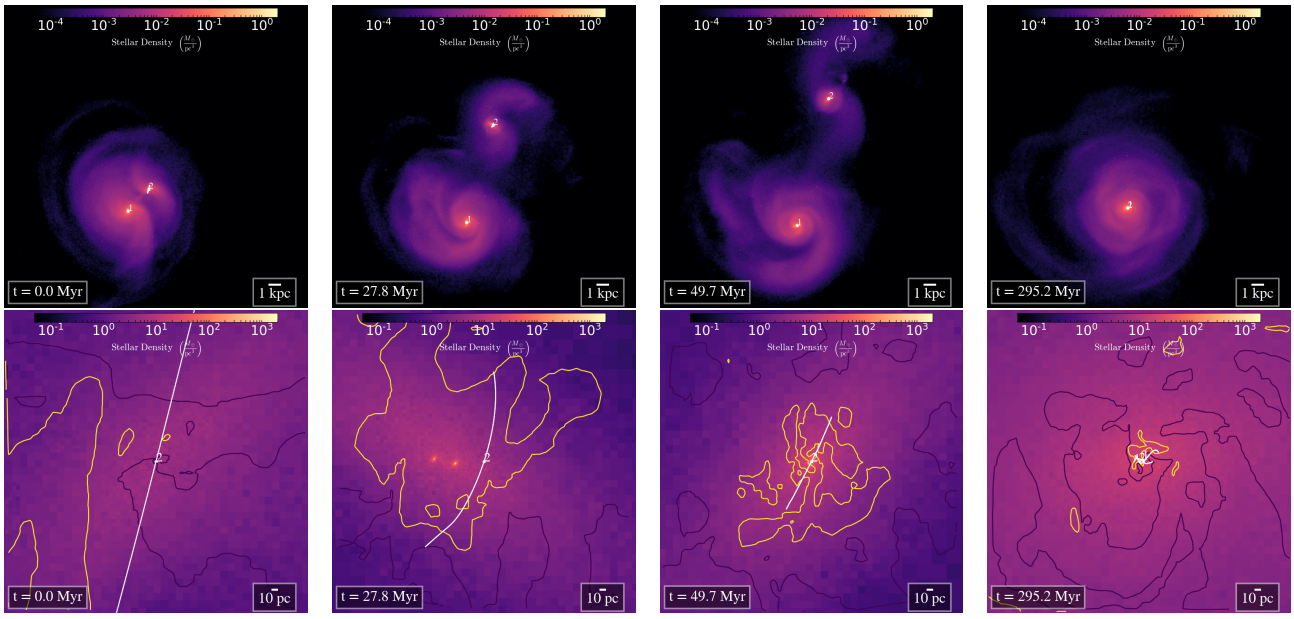


Figure 39: Stellar density maps of the two galaxies (top row) and centred on the secondary BH (bottom row). Initially, the BH proceeds on a smooth trajectory (first column); then, some stellar clumps formed during the starburst deviate the BH from its smooth trajectory (second column). At some point those clumps merge and the BH is captured in the resulting larger clump (third column); finally, the BH binary forms (fourth column). The white line in the bottom images represents the position of the BHs within $\pm 1\,\mathrm{Myr}$. In order to show how irregular the gas density is compared to that of stars, we indicate the iso-$\rho_{\mathrm{gas}}$ contours of 1 (10) a.m.u. $\mathrm{cm}^{-3}$ with purple (yellow) lines.

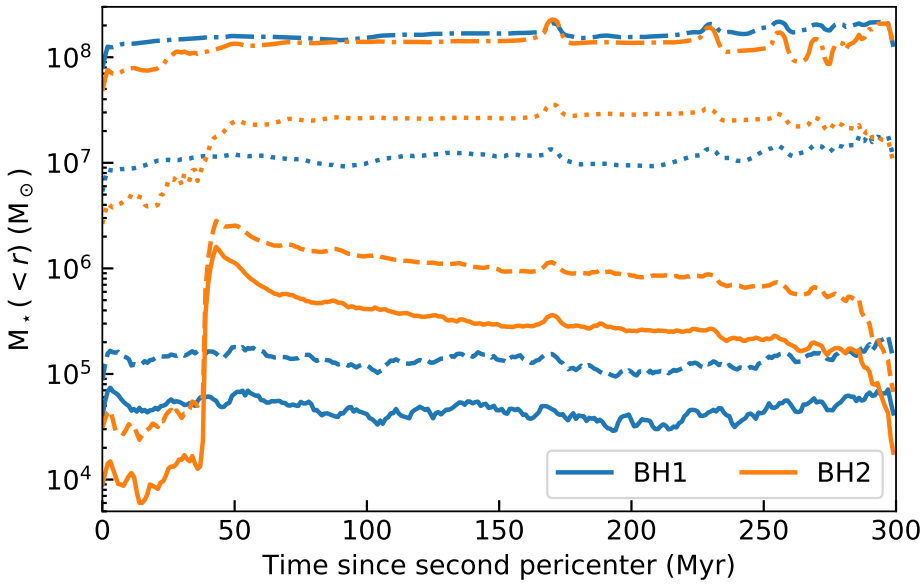


Figure 40: Enclosed stellar mass within 3 (solid), 5 (dashed), 30 (dotted), and 100 (dash-dotted) pc around each BH, as a function of time elapsed since the second pericentre, *i.e.* the time when the high-resolution resimulation starts.

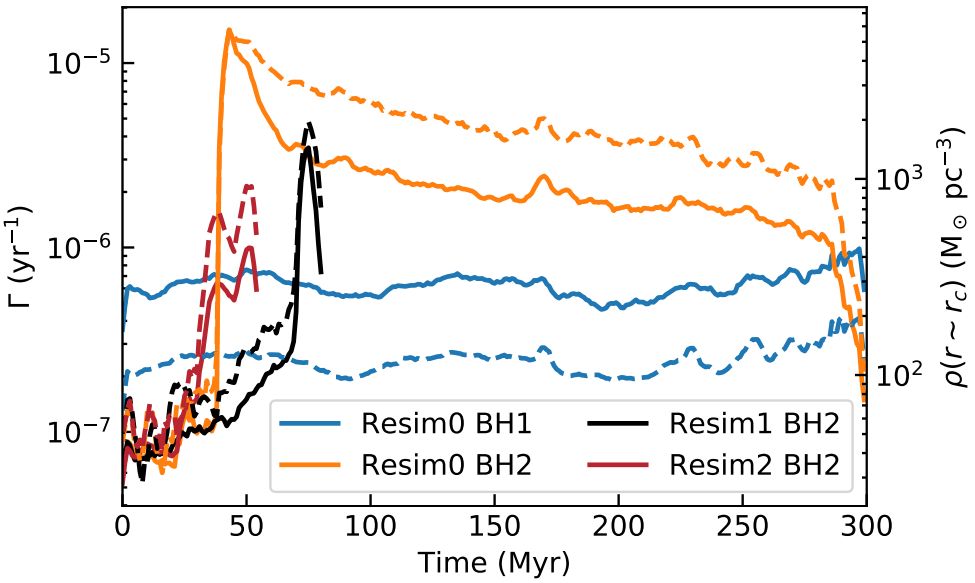


Figure 41: TDE rate around each BH (solid line) and stellar density at the critical radius (dashed line). $r_c$ is estimated from Eq. (137) for BH masses of $4.4 \times 10^6\,M_\odot$ and $1.4 \times 10^6\,M_\odot$ resulting in $r_c$ of 14 pc and 3 pc. We show the same quantities for BH2 in the other re-simulations, which are run for a shorter time as we are only interested in the enhancement of the stellar density following the first starburst. All quantities are shown as a function of time.

merger: during the 300 Myr of the simulation, very few stars form around the primary BH, in agreement with the lower-resolution run (Capelo et al., 2015). Therefore, we expect the TDE rate to remain roughly constant.

The secondary galaxy, instead, undergoes a major starburst just after the second pericentre, lasting 50 Myr. As the gas is perturbed by tidal torques and ram-pressure shocks, it loses angular momentum and falls towards the centre, triggering nuclear star formation, forming stellar clumps as shown in the second column of Fig. 39. These clumps are fairly small (few pc size) but can be very massive, up to a few $10^6\,M_\odot$, similar to the mass of BH2 ($\sim 1.4 \times 10^6\,M_\odot$). This leads to interactions that scatter the BH. Consequently, the density "seen" by the BH is highly dependent on local stochastic processes. The enclosed mass within 5 pc from BH2 (orange dashed line in Fig. 40) is almost constant, until it increases abruptly as the clumps merge and capture the BH at about 50 Myr. This is clear both from the third column of Fig. 39 and from Fig. 40. After this rise in density, the enclosed mass within 5 pc does not vary until the binary forms, whereas the enclosed mass within 3 pc decreases. This is contrary to the expectations of the evolution of a mass distribution around a BH, which normally contracts (Bahcall and Wolf, 1976; Quinlan, Hernquist, and Sigurdsson, 1995). However, at difference with the assumptions in classic approaches, which look at equilibrium, steady-state solutions or BHs growing slowly within the stellar distribution, the BH enters rapidly the stellar clump, and the mass of the clump and the BH are similar. The effect we observe can be explained assuming system BH-clumps suffers a series of

high-speed encounters (Binney and Tremaine, 1987), bringing enough energy to start the disruption of the clump, although we cannot rule out that the effect is numerical. When the binary forms, *i.e.* BHs are separated by about 1 pc, the enclosed mass decreases again. This might be due to heating: when the binary shrinks, it releases energy in the nucleus. Since the simulation cannot resolve scatterings between stars and the binary, we are unable to rigorously confirm if this effect is physical or a numerical artifact, although N-body simulations show similar results (*e.g.* Milosavljević and Merritt, 2001).

Note also that the mass within $r_c$, about 30 (5) pc for BH1 (BH2), is similar to that of the mass of the BH. Therefore, we can assume that $M(r_c) \sim M_\bullet$ and, as $\sigma^2(r) \sim G(M_\bullet + M(r))/r$, Eq. (122) can be approximately solved as:

$$r_c \sim 3\,\mathrm{pc} \left(\frac{M_\bullet/m_\star}{10^6}\right)^{4/3} \left(\frac{r_\star}{R_\odot}\right), \tag{137}$$

from which we find that $r_c$ is 14 (3) pc for BH1 (BH2), in excellent agreement with the results of Fig. 38 given the simplicity of the expression. We will therefore further use this approximation.

In summary, the amount of stars around BH2 changes significantly during the merger, and thus we expect large variations of its TDE rate. However, the exact enhancement may depend on the position of the BH, which can be chaotic due to three-body interactions with stellar clumps. The amount of stars around BH1 remains fairly constant and we do not expect much change in the TDE rate until it binds with BH2 and it is embedded in the same stellar environment.

**TDE rate** Using the techniques described in Section 4.2.2.1, we estimate the TDE rate as a function of time in the simulations. Note that here we have taken the conservative assumption of not including an inner cusp around the BHs (Bahcall and Wolf, 1976), hence the estimated TDE rate is a lower bound.

We show in Fig. 41, as a function of time, the TDE rate around each BH (solid line) and the density at the critical radius (dashed line) as defined in Eq. (137). Note the remarkable agreement between the TDE rate measured with the `PhaseFlow` code and the stellar density at $r_c$.

The initial TDE rate is very small ($\sim 10^{-7}\,\mathrm{yr}^{-1}$ for both BHs), because the density around each BH is very low: we find, for the two BHs, a stellar density of $\sim 10^2\,M_\odot\ \mathrm{pc}^{-3}$, which is one to two orders of magnitude lower than in local galaxies (Faber et al., 1997). The reason is that the analytical initial conditions of the merging galaxies (Capelo et al., 2015) assume that the stellar bulge is described by a spherical Hernquist profile (Hernquist, 1990) with inner logarithmic slope $\gamma = -1$, whereas local galaxies exhibit a range of inner density slopes going from $\gamma \sim 0$ to $\gamma = -2$ (Faber et al., 1997; Lauer et al., 2007), up to $\gamma = -4$ in the presence of nuclear star clusters, common in low-mass galaxies (Glass et al., 2011). In

addition, before the beginning of the merger simulation, galaxies are relaxed for 100 Myr and, during this time, the velocity distribution near the resolution limit (10 pc) is not well sampled because of the limited number of stars, leading to an even shallower profile than the initial Hernquist profile.

The TDE rate around BH1 is fairly constant, irrespective of the dynamical phase of the merger: since the stellar density profile around BH1 is not affected by the merger, the amount of stars available to be disrupted is constant and so is the TDE rate. The TDE rate around BH2 is instead increased by a factor of about 30 during the 250 Myr following the burst, with a short peak of more than two orders of magnitude enhancement. During the first 200 Myr of this enhancement, the two galaxies can be separated by more than 1 kpc, up to 10 kpc. While the maximum value of $\sim 10^{-5}\,\mathrm{yr}^{-1}$ may seem surprising low, we recall that the initial density profile, after relaxing the initial conditions, was shallow and we do not include the possibility of a stellar cusp due to unresolved stellar dynamics, which would increase the initial TDE rate and, perhaps, decrease the relative enhancement caused by merger-driven nuclear star formation.

The central density and the TDE rate drop once the binary is formed. However, to calculate the TDE rate we assumed a single BH surrounded by a spherical density distribution, which is not valid any longer after formation of the binary. Other techniques for binary BHs have been used (*e.g.* Lezhnin and Vasiliev, 2019), often resulting in an increased rate, at least for a short time (*e.g.* Chen et al., 2009; Li et al., 2017).

**Effect of stochasticity** We rerun the exact same simulation, but changing the random seed used in the stochastic sampling of star formation (`Resim1` and `Resim2`), and perform the same analysis. This test is done for three main reasons: firstly, reproducibility of our results; secondly, the small number of particles around the BH in the early phase before the starburst, about $10^4\,\mathrm{M}_\odot$ within 3 pc corresponding to 10 stellar particles, see Fig. 40, might affects our results; thirdly, because reaching pc-resolution is a double-edged sword. On the one hand, we resolve the gas flows and star formation very close to the BH. On the other hand, the stochasticity of very local processes becomes important. The exact position and mass of the forming stellar clumps have strong effects on both the orbits of BHs and on the density around them.

We show in Fig. 41 the TDE rate and density at the critical radius around BH2. In all cases, the same common trends appear: there is a starburst, which results in an enhancement of the density at the critical radius, causing an increase of the TDE rate around BH2, followed by a decay on Myr scales. However, the exact moment when the density increases, and its exact peak value, depend on the simulation, showing how small changes (the random seed and therefore the exact location of star formation) in this chaotic system can affect the TDE rate in galaxies. We note that, since the galaxy hosting BH1 is not experiencing strong star

formation, the results for BH1 are the same in all three re-simulations. Overall, the mean maximal enhancement of the TDE around BH2 in the three simulations is about 140.

Here is a summary of the results presented in this Chapter:

- We introduced the loss cone theory and two extreme regimes: the full loss cone regime in which the relaxation timescale is much shorter than the radial period, and the empty loss cone regime in the opposite situation. We also presented an analytical calculation for the full loss cone regime, which allows to estimate the TDE rate given stellar properties around the BH (velocity dispersion, density etc...).
- We briefly summarized observations of TDE host galaxies. In particular how TDE hosts usually have a lower current SFR than main sequence galaxies and that E+A galaxies are over-represented by about 50.
- Using a zoom-simulation of a galaxy merger, we studied the evolution of the surrounding stellar density and computed the evolution of the TDE rate. The nuclear starburst produces stellar clumps that scatter the BH and modulate the stellar density in its vicinity. The enhancement of the TDE rate and its duration can therefore vary significantly in different realizations of the same process. However, in all our simulations, the environment and TDE rate around the BH in the most massive galaxy are rather unaffected by the merger, while the TDE rate in the secondary galaxy is always enhanced. This suggests that the TDE rate is larger in galaxies in the final phases of mergers or the immediate post-merger phase, lasting a few hundreds of Myr, than in galaxies in isolation.

# 5

# CONCLUSIONS

## 5.1 A THREE YEARS SUMMARY

In this Thesis, I mainly tackled from a theoretical perspective two different topics: dynamics of BHs and dynamics of stars in the vicinity of BHs. Many groups and researchers work on these subjects, using different techniques, making them extremely interesting and stimulating. In addition, from an observational perspective, facilities are currently being built: LISA will detect gravitational waves from binary supermassive BHs, JWST will observe the first BHs, eROSITA and the LSST will detect hundreds (thousands?) of TDEs. This justifies the need for theoretical work to help interpreting and understanding future observations.

The dynamics of BHs is a vast topic, the questions I tried to answer are: what fraction of galaxy mergers end up in binary BHs? what are the properties (masses only at the moment, but further studies will expand to spins, eccentricity etc...) of binary BHs? The final goal is to predict the BH merger rate we will detect with LISA and the properties of these mergers. To study this, I first studied the effects of dynamical friction (see Chapter 2). I confirmed (Pfister et al., 2017), using zoom simulations of galaxy mergers, that this process is able to drive BHs down to pc scales and form a binary for $\sim 10^6\,M_\odot$ BHs. However, to be able to resolve (and therefore include) this process in numerical simulations, the influence radius (the radius at which gravity is dominated by the BH) must be resolved. I insist that this puts strong constrains on resolution as the influence radius is $\sim 1\,pc$ for $10^7\,M_\odot$ BHs, far below what can be resolved in a cosmological context with current computing power (resolution is generally at best $\sim 100\,pc$). This means we are not in conditions to obtain good statistics on the processes studied, *e.g.* the merger rate. To overcome this issue, I developed (Pfister et al., 2019a) a physically motivated model to remove to BHs momentum due to unresolved dynamical friction from stars and dark matter. To date, `Ramses` is the only code available with a physically motivated model for unresolved dynamical friction from gas, stars and dark matter. I performed cosmological zooms of a $10^{12}\,M_\odot$ halo at redshift 2 to understand how BHs behave in galaxies in isolation and following mergers (see §3.3). I found that, due to anisotropies in galaxies, or violent events, such as mergers, affecting the shape of galaxies, BHs with masses as low as $10^4\,M_\odot$ are easily scattered from the center of their host and follow a physically motivated random walk. On the contrary, slightly more

massive BHs ($10^5\,M_\odot$) remain in the potential well of their host galaxy. From this, I expect that it is unlikely that $\sim 10^4\,M_\odot$ BHs participate in the merging population, unless they are embedded in dense bound stellar or gaseous envelopes, slightly more massive BHs mergers ($10^5\,M_\odot$) remain possible. In addition, I expect that if we ever observe intermediate mass BHs with masses as low as $10^4\,M_\odot$, at high redshift when galaxies are not well settled, they will be off-centered.

The second main topic I investigated is the dynamics of stars in the vicinity of BHs. In particular, I got interested in the following questions: how many TDEs per year per galaxy do we expect? is this rate enhanced during mergers? should E+A galaxies, with no current star formation rate and a recent starburst, have a larger TDE rate on average, as observed? Different groups started to investigate the two first questions more than 20 years ago, but so far, people mostly performed analytical calculations or N-body simulations in the vicinity of BHs where the number of stars entering the TDE radius can be directly measured. Analytical calculations through the loss cone formalism have the advantage to be extremely fast and allow to study a wide range of parameters, but lack the time evolution. N-body simulations are more expensive, but the time evolution of the TDE rate can be obtained, however, only stars (and the BH) are included, missing all the subtleties of galaxies: gas, cooling, star formation, stellar feedback, BH accretion and AGN feedback etc... I was the first, in Pfister et al., 2019b, to apply the loss cone formalism to realistic density profile obtained from an hydrodynamical (in contrast to N-body) simulation of galaxy merger including state–of–the–art subgrid physics. With this simulation, I estimated the evolution of TDE rate during the merger (see Chapter 4), where a nuclear starburst triggered by torques and ram pressure increases the stellar density in the vicinity of the BH. In the specific case studied here, the increased stellar density causes an enhancement of the TDE rate by $\sim 30$, with a peak of more than two orders of magnitude enhancement. I stress here that I only performed this analysis for one particular merger, therefore this should be considered as a qualitative result and more studies are needed before a fair comparison with observations can be done.

Finally, I briefly worked on the dynamics of interacting galaxies, understanding how likely it is that two galaxies observed near to each other in the sky, *i.e.* close in projected and redshift distances, merge (see §3.2). For this study I used part of the machinery that comes with the `HorizonAGN` simulation: the galaxy catalog extracted from the lightcone and the merger tree. I found (Pfister and Dotti, in prep) that the best thresholds to select galaxies that will effectively merge within a reasonable time (3 Gyr), given the mass range/ratio used, are $\Delta d \sim 100\,\mathrm{kpc}$ and $\Delta z \sim 10^{-3}$. $\Delta d \sim 100\,\mathrm{kpc}$ is commonly used by observers but they usually used $\Delta z \sim 10^{-2}$ while today's facilities allow for redshift precision of order $\sim 10^{-3}$. This will allow for better estimates of the merger rate in large surveys, or allow to better understand the role of mergers in triggering starburst or AGNs for instance.

## 5.2 A THREE YEARS PERSPECTIVE

It is with great pleasure that I will work for one year at the DARK center (Copenhagen, Denmark), followed by two years at the University of Hong-Kong (China), as a Sophie and Tycho Brahe Fellow, to collaborate with Enrico Ramirez-Ruiz and Jane Dai. Interacting with new persons in a new environment will necessarily seed new interests, however, given the expertise that I acquired during this PhD, I will still work on the topics described above.

In order to determine more realistically the BH merger rate in the redshift/mass band of LISA, I will run the first cosmological simulation using all the subgrid physics available in `Ramses`, and in particular the new physically motivated model for dynamical friction from gas, stars and dark matter. To contain computational costs, this simulation will have a small volume ($\sim 15\,\mathrm{Mpc}$ side while `HorizonAGN` is $\sim 140\,\mathrm{Mpc}$ side) and will be run down to $z \sim 2$. The spatial resolution will be $\sim 10\,\mathrm{pc}$ and stellar mass resolution $\sim 2 \times 10^3\,\mathrm{M}_\odot$, for a minimum BH mass of a few $10^4\,\mathrm{M}_\odot$. Although the box will be too small to be cosmic–variance independent, it will be the first study with this kind of resolution and volume. Note that I already successfully applied for 2.5 million cpu–hours computing time on Occigen (french supercomputer) for this project, and that the simulation should start as soon as possible.

I will also implement, for the first time in a simulation, TDEs around BHs as a subgrid model using the estimates from the loss cone theory. This is feasible, the quantities to measure are similar to those I already measure for calculating dynamical friction: stellar density, stellar velocity dispersion etc... The applications of such a model are numerous: measuring the evolution of the TDE rate with redshift, measuring the amount of BH mass coming from gas or stars, predict the TDE rate of intermediate mass BHs etc... I am particularly interesteded in probing typical properties of galaxies hosting TDEs, and test if, indeed, E+A and low star-forming galaxies have a larger TDE rate, as observed. I have already started to collaborate with Ben Bar-Or (Princeton University, USA) and Nick Stone (Columbia Univesity, New-York, USA) on this topic. Another possible extension, which I have started to discuss with Jane Dai, is to study the effects of the possible super-Eddington accretion usually coming with TDEs. This would be eased by the current work of our group at IAP, who is implementing super-Eddington accretion in `Ramses`.

Finally, regarding the fraction of galaxy pairs ending up in mergers, I have recently attended a lecture about neural network and deep learning. I would like to use mock images of the `HorizonAGN` simulation, produced by Clothilde Laigle (IAP) to provide better tracers of galaxy mergers than projected and redshift distances.

# 6

# THE RAMSES CODE

In this Thesis, we mostly studied dynamics: of BHs following galaxy mergers, of stars around BHs... While all the analytical calculations performed in a newtonian regime are crucial to understand the physics and relevant parameters to our problems, they lack all the subtleties of real galaxies: gas, star formation, cooling, supernovae, BH accretion, AGN feedback etc... For this reason, we decided to study dynamical problems with numerical hydrodynamical simulations. The main tool we used is the Adaptive Mesh Refinement (AMR) code `Ramses` (Teyssier, 2002), and a deep understanding of how it works is mandatory to properly use it and do good research. In this Appendix we detail the numerics and physics of the code.

## 6.1 ASTROPHYSICAL FLUIDS

### 6.1.1 *Hydrodynamics*

To study galaxies we need to track gas which will form stars observed in the sky. We present here the different equations describing this fluid and the way we solve them numerically in `Ramses`.

#### 6.1.1.1 *Euler equation*

The gas follows the Euler equations, expressing the conservation of mass, momentum and energy and which can be written as:

$$\frac{\partial}{\partial t}\begin{pmatrix}\rho\\ \rho\mathbf{v}\\ e\end{pmatrix}+\nabla\cdot\begin{pmatrix}\rho\mathbf{v}\\ \rho\mathbf{v}\mathbf{v}^{\mathbf{T}}+P\mathbb{1}\\ \mathbf{v}(e+P)\end{pmatrix}=\begin{pmatrix}0\\ -\rho\nabla\phi\\ -\rho\mathbf{v}\cdot\nabla\phi+\rho^2\Lambda+\mathcal{H}\end{pmatrix} \tag{138}$$

$$\Leftrightarrow \frac{\partial \mathbf{U}}{\partial t}+\nabla\cdot(f(\mathbf{U}))=S(\mathbf{U})\,, \tag{139}$$

where $\rho$ is the fluid density, $\mathbf{v}$ its velocity, $e$ its total energy per units volume, $P$ its pressure, $\phi$ the gravitational potential calculated as explained in §6.1.2 and $\Lambda$ and $\mathcal{H}$ are respectively the cooling and heating function discussed in §6.3.1. To solve this system with 5 equations and 6 unknown quantities: $\rho$, the 3 components of $\mathbf{v}$, $e$ and $P$, we need a last closure equation of state. We assume the gas to be an ideal non relativistic gas, which is described by:

$$P=(\gamma-1)\epsilon=(\gamma-1)(e-\frac{1}{2}\rho v^2)\,, \tag{140}$$

where $\epsilon$ is the internal energy per units volume of the gas and $\gamma$ is the adiabatic index, $5/3$ for a monoatomic gas.

As expected, this is a complex problem, with six coupled non-linear differential equations and this explains the massive use of computers. In §6.1.1.2, we explain how to numerically integrate these equations in a simplified case, without gravity nor cooling and heating, and in 1D, where the equations take the following form:

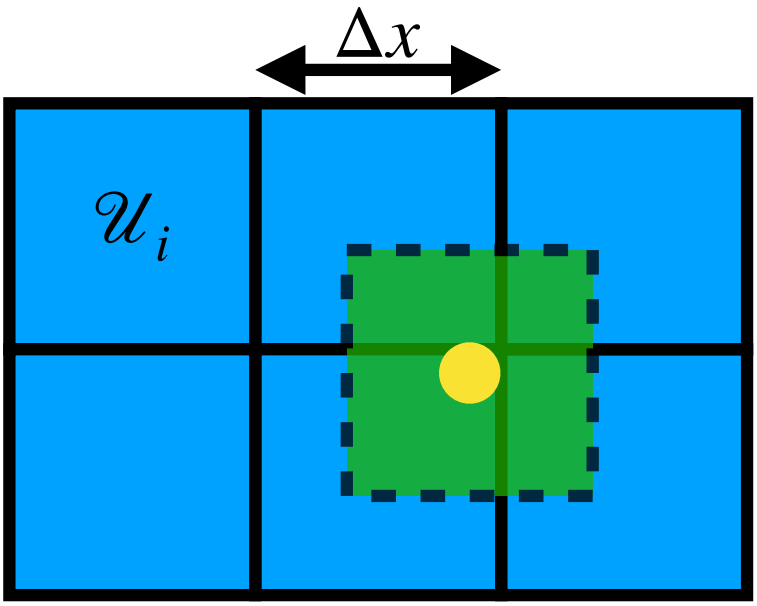


Figure 42: Grid containing all the hydrodynamical informations ($\mathbf{U}_i$) on cells of size $\Delta x$. We also show how the Cloud–In–Cell interpolation scheme works.

$$\frac{\partial}{\partial t}\begin{pmatrix}\rho\\ \rho u\\ e\end{pmatrix}+\frac{\partial}{\partial x}\begin{pmatrix}\rho u\\ \rho u^2+P\\ u(e+P)\end{pmatrix} = \frac{\partial \mathbf{U}}{\partial t}+\frac{\partial}{\partial x}(f(\mathbf{U})) \tag{141}$$

$$= 0\,, \tag{142}$$

where $u$ is the velocity among the axis considered.

#### 6.1.1.2 *Numerical techniques*

In grid based code based on Euler approach, such as `Ramses`, the fluid is sampled in cells with a finite volume, as shown in Fig. 42. In this Section, we consider a uniform grid with a constant cell size $\Delta x$, the center of the cell $i$ is $x_i$ and we denote the interface position between cells $i-1$ and $i$ by $x_{i-1/2}$. If the "real" solution to the problem is $\mathbf{U}(x,t)$, we sample it a different times $t_n$ and position $x_i$:

$$\mathbf{U}_i^n = \frac{1}{\Delta x}\int_{x_i-\Delta x/2}^{x_i+\Delta x/2}\mathbf{U}(x,t_n)dx\,. \tag{143}$$

**Godunov method** Integrating Eq. (142) on a cell between two timesteps, $t_{n+1}-t_n=\Delta t$, gives:

$$0 = \int_{x_i-\Delta x/2}^{x_i+\Delta x/2}\int_{t_n}^{t_{n+1}} \frac{\partial \mathbf{U}}{\partial t} + \frac{\partial}{\partial x}(f(\mathbf{U}))dtdx \tag{144}$$

$$0 = \int_{x_i-\Delta x/2}^{x_i+\Delta x/2}[\mathbf{U}(x,t_{n+1}) - \mathbf{U}(x,t_n)]dx + \int_{t_n}^{t_{n+1}}[f(\mathbf{U}(x_{i+1/2},t)) - f(\mathbf{U}(x_{i-1/2},t))]dt \tag{145}$$

$$0 = \Delta x[\mathbf{U}_i^{n+1} - \mathbf{U}_i^n] + \int_{t_n}^{t_{n+1}}[f(\mathbf{U}(x_{i+1/2},t)) - f(\mathbf{U}(x_{i-1/2},t))]dt \tag{146}$$

$$\Rightarrow \mathbf{U}_i^{n+1} = \mathbf{U}_i^n + \frac{1}{\Delta x}\int_{t_n}^{t_{n+1}}[f(\mathbf{U}(x_{i+1/2},t)) - f(\mathbf{U}(x_{i-1/2},t))]dt\,. \tag{147}$$

We see here that the technical problem comes from the integral which value is, *a priori*, unknown. However, if the time-step is small enough, one can consider that the interfaces at $x_{i\pm1}$ is a Riemann Problem (see following paragraph), for which the mean value of the integral, $f^\star(\mathbf{U}_L, \mathbf{U}_R)$, is known analytically and depends only on the initial value on the left and right side of the interface, $\mathbf{U}_L$ and $\mathbf{U}_R$:

- $\int_{t_n}^{t_{n+1}} f(\mathbf{U}(x_{i-1/2},t))dt = \Delta t f^\star(\mathbf{U}_{i-1}^n, \mathbf{U}_i^n)$ (148)
- $\int_{t_n}^{t_{n+1}} f(\mathbf{U}(x_{i+1/2},t))dt = \Delta t f^\star(\mathbf{U}_i^n, \mathbf{U}_{i+1}^n)\,.$ (149)

We finally obtain:

$$\mathbf{U}_i^{n+1} = \mathbf{U}_i^n + \frac{\Delta t}{\Delta x}\left[f^\star(\mathbf{U}_{i-1}^n, \mathbf{U}_i^n) - f^\star(\mathbf{U}_i^n, \mathbf{U}_{i+1}^n)\right]\,. \tag{150}$$

**Riemann problem** The Riemann Problem is following: consider two half space that meet in $x = 0$, the initial conditions being given by:

$$\mathbf{U}_L = \begin{pmatrix} \rho_L \\ \rho_L u_L \\ e_L \end{pmatrix}, \mathbf{U}_R = \begin{pmatrix} \rho_R \\ \rho_R u_R \\ e_R \end{pmatrix}, \tag{151}$$

where subscripts stand for left and right.

There exists an analytical solution to the Euler equations for this set of initial conditions (see Chapter 4 of Toro, 1997) which allows us to have an analytical expression for $f^\star$, however it involves solving a transcendental equation, which is numerically long. This is why

numericists usually prefer approximate solutions given by a Riemann solver. The one we use in `Ramses` is the Harten-Lax-Van Leer Contact Riemann solver (HLLC). More details can be found in Chapter 10 of Toro, 1997.

### 6.1.2 *Gravity*

In §6.1.1, we neglected gravity to focus on the different techniques used to solve the hydrodynamical equations. However, gravity is fundamental to understand formation, growth and evolution of galaxies, thus must be included.

#### 6.1.2.1 *Poisson equation*

The gravity force felt by matter can be obtained through the gradient of the gravitational potential, $\phi$, that can itself be obtained with the Poisson equation:

$$\Delta\phi = 4\pi G\,\rho\,, \tag{152}$$

where $G$ is the gravitational constant and $\rho$ is the total density of gas, stars and dark matter. To numerically solve this equation, we can again use the grid structure of `Ramses`. If $\phi_i$ and $\rho_i$ are the potential and density in cell $i$, and if we consider a 1D problem, Eq. (152) can numerically be written:

$$\frac{1}{\Delta x^2}\begin{pmatrix} -2 & 1 & 0 & 0 \\ 1 & . & . & 0 \\ 0 & . & . & 1 \\ 0 & 0 & 1 & -2 \end{pmatrix}\begin{pmatrix} \phi_1 \\ . \\ . \\ \phi_N \end{pmatrix} = A\phi = 4\pi G\begin{pmatrix} \rho_1 \\ . \\ . \\ \rho_N \end{pmatrix}, \tag{153}$$

N corresponding to the number of cells.

Since $A$ is symmetrical, there exists a basis of normal eigenvectors of $A$ in which $A$ is diagonal and easily inversible, therefore in which the expression of $\phi$ is easy to obtain. However, in the general 3D case, $A$ is a large 6D tensor and inversing it is a difficult task.

Instead, we use an approximate solution, obtained iteratively, which is sufficiently good for the problem we want to solve. We define:

$$f(x) = \frac{1}{2}x^T Ax - 4\pi G\,\rho^T x\,, \tag{154}$$

which is at minimum for $x = \phi$. Indeed, $f'(x) = (Ax - 4\pi G\,\rho)^T$, and from Eq. (153), $f'(\phi) = 0$. With this, we transformed a matrix inversion problem into a minimization problem. Starting with an initial "guess" for $\phi$, $\phi^{(0)} = 4\pi G\,\rho(\Delta x)^2$, and using an iterative approach ,

the exact solution to $f'(x) = 0$ can be found in N steps. As this number can be very large, in practice, we stop when $|f'(\phi^{(k+1)}) - f'(\phi^{(k)})| < \epsilon$, where $\epsilon$ is the resolution needed.

#### 6.1.2.2 *N-body solver*

We have discussed in §6.1.1 how to follow the dynamics of gas using the grid available in `Ramses`, however, dark matter and stars, because they form a collisionless system, cannot be treated the same way. Instead, we use particles, which only feel gravity and are moved through Newton's law:

$$\frac{d\mathbf{v}}{dt} = -\nabla\phi\,. \tag{155}$$

Here, we detail how we numerically integrate this equation. At time $t_n$, $\phi(\mathbf{r}, t_n)$ is computed as explained in §6.1.2.1. Then, a classic strategy to go from $t_n$ to $t_{n+1}$ would be the use of an Euler integrator. During $t_{n+1} - t_n = \Delta t$, the position $\mathbf{r}$ and velocity $\mathbf{v}$ are updated as:

- $\mathbf{r}_{n+1} = \mathbf{r}_n + \mathbf{v_n}\Delta t$
- $\mathbf{v}_{n+1} = \mathbf{v}_n - (\nabla\phi)\,(\mathbf{x}_n, t_n)\Delta t$

The well known issue with the Euler integrator is that it is not symplectic, *i.e.*, it does not conserve the energy of the system. For this reason we use the simplest symplectic integrator, which is not much expensive than the Euler one, the leap-frog (or kick-drift-kick). During $t_{n+1} - t_n = \Delta t$, the position $\mathbf{r}$ and velocity $\mathbf{v}$ are updated in three steps:

1. $\mathbf{r}_{n+1/2} = \mathbf{r}_n + \mathbf{v}_n \frac{\Delta t}{2}$
2. $\mathbf{v}_{n+1} = \mathbf{v}_n - (\nabla\phi)\,(\mathbf{x}_{n+1/2}, t_n)\Delta t$
3. $\mathbf{r}_{n+1} = \mathbf{r}_{n+1/2} + \mathbf{v}_{n+1} \frac{\Delta t}{2}$

#### 6.1.2.3 *Particle deposition*

We have seen in §6.1.2.1 how to use the grid structure available in `Ramses` to compute the gravitational potential. However, as stars and dark matter are particles (§6.1.2.2), their mass is initially not "on the grid". Therefore Poisson equation cannot be solved properly. Several techniques exists to perform this deposition (Nearest Grid Point, Triangular Shaped Cloud) but the one used in `Ramses` is the Cloud In Cell (CIC) deposition, a trilinear interpolation of the deposition, illustrated in Fig. 42.

## 6.2 AN ADAPTIVE CODE

Until now, we have described how numerically integrate the equations which describe the main components of our Universe. At each passage in the time-loop the following steps are done:

1. Deposit the mass of dark matter and stars onto the grid to obtain the total density in each cell (§6.1.2.3).
2. Given the total density, compute the gravitational potential (§6.1.2.1).
3. Given the potential, update the position and velocity of dark matter and stars (§6.1.2.2), update the density, velocity and energy of gas in each cell (§6.1.1.2).

Unfortunately, computing power is not infinite and we cannot always afford the spatial or temporal resolution wanted. To overcome this issue different techniques are used.

### 6.2.1 *Adaptive Mesh Refinement*

In grid-based codes, the different properties of the fluid (at least 6, more if metals, dust, magnetic fields, cosmic rays or radiation... are included) are stored in cells which sample the box of the simulation. The amount of numbers $N$ we need to store for a volume $L^3$ with a resolution $\Delta x$ is given by:

$$N \sim 6 \left( \frac{L}{\Delta x} \right)^3 . \tag{156}$$

As each numbers are stored on 8 bytes, the amount of memory $M$ needed is:

$$M \sim 8N \text{ bytes } \sim 48 \text{ bytes } \left( \frac{L}{\Delta x} \right)^3 . \tag{157}$$

For a reasonable patch of universe, say $L = 100\,\mathrm{Mpc}$, while resolving the interstellar medium, *i.e.*, having a resolution of $\Delta x = 10\,\mathrm{pc}$, this represents $4.8 \times 10^{13}$ GB, much more than what is available on the most powerful supercomputer available on Earth.

To overcome this issue, some cells of the grid are refined to a better resolution, but not all (see Fig. 43). This considerably reduces the total number of cells while not affecting too much the results, indeed, as we have seen in Chapter 1, the Universe is mostly empty, and we are interested in the dense regions (filaments, galaxies etc...). For this reason, refined cell are usually the ones containing the most mass but, in principle, any criterion can be used (pressure gradient, density etc...).

Although the idea is fairly simple, the numerical implementation is much more difficult than in the fixed grid situation. We use the sketch in Fig. 44 to describe how to translate

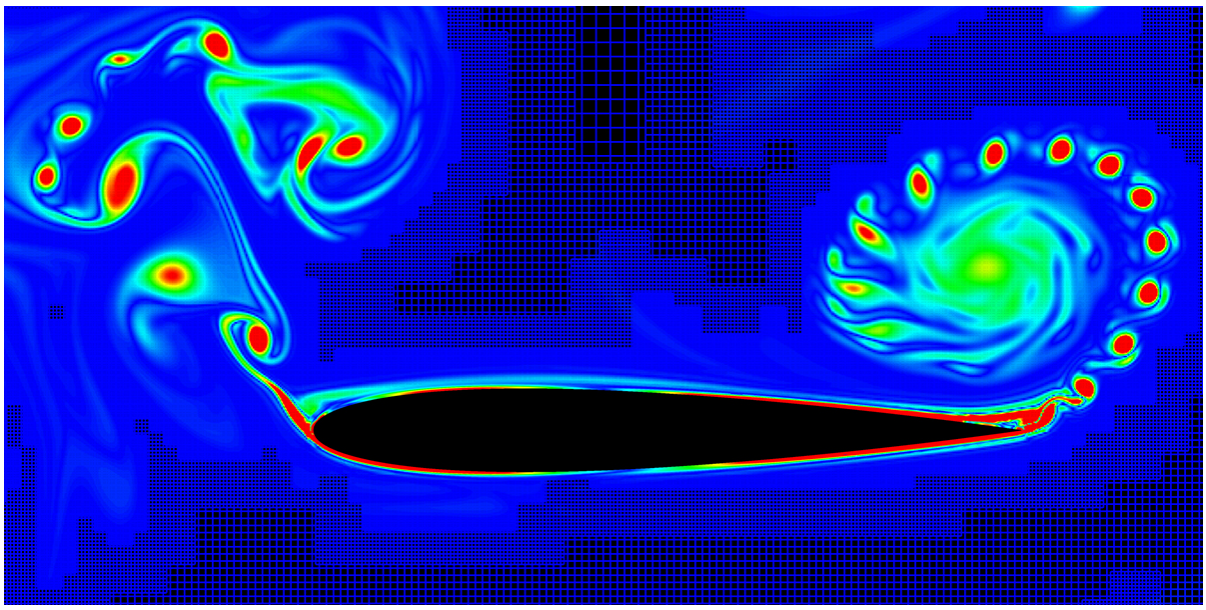

Figure 43: AMR used to resolve the airflow around planes. Interesting turbulent regions (red) are refined at maximum while empty laminar regions (dark blue) have a coarser resolution.

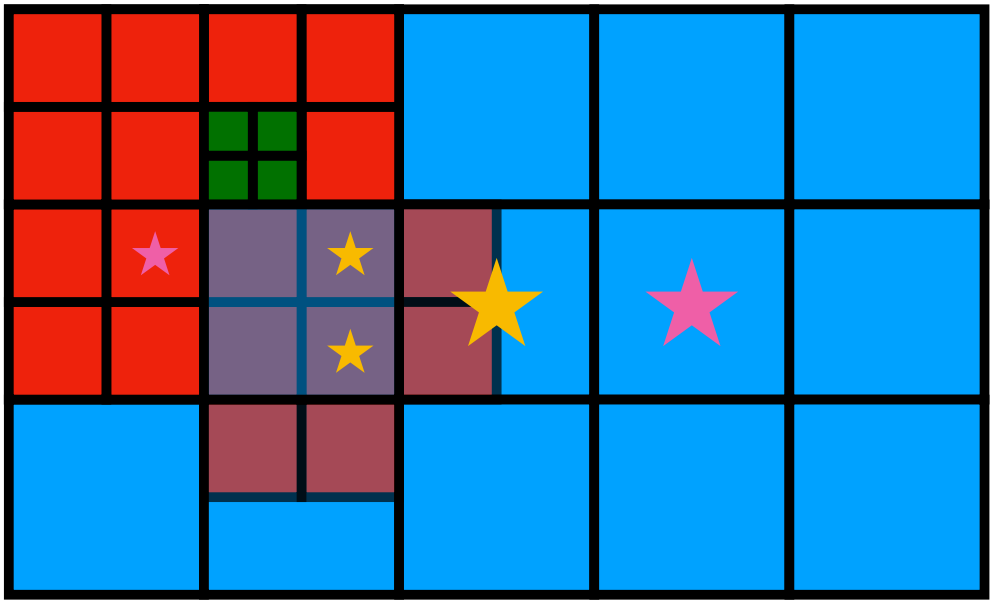

Figure 44: AMR in `Ramses`. Everything happens "as if" all cells had neighboring cells of the same level.

the techniques described for fixed grids in §6.1.1 and §6.1.2 to an adaptive grid. In this situation, there are 3 levels ($l_{min}$ in blue, $l_{min}+1$ in red and $l_{min}+2$ in green). Note that, as `Ramses` does, we force that two neighboring cells have at maximum one level difference (blue/green interface is not possible).

Different cases can occur. If all the neighboring cells are at the same level (two examples are marked in pink): fluxes and gravity can be computed as if the grid was uniform, this is the easy case. On the contrary, if some neighboring cells are at different levels (three examples are marked in yellow), it is more complicated. The idea is to add "fake cells" (transparent on our sketch) so that everything happens "as if" the grid was uniform. The simplest technique is to group cells of finer level to produce a larger cell with the mean properties, and to assume that a cell of the coarser level is split-up into cells of the finer level. In the end, everything happens "as if" all cells had neighboring cells of the same level.

### 6.2.2 *Adaptive timestep*

When moving particles on the grid or solving the hydrodynamical equations, we always assumed that the timestep $\Delta t$ was fixed. However, it is clear that the value cannot be chosen arbitrary. Here are the different conditions imposed for each cell with size $\Delta x$ in `Ramses`:

- The free-fall time, $t_{ff} = \sqrt{3\pi/(32\,G\,\rho)}$, with $\rho$ the density of the cell, must be resolved: $\Delta t < t_{ff}$.
- Particles in the cell, moving at $v$ cannot cross more than one cell in one timestep: $\Delta t < \Delta x / \max_{particles}(v)$.
- Gas with speed $u$ and sound speed $c_s$ cannot cross more than one cell in one timestep: $\Delta t < \Delta x/(u + c_s)$.
- For cosmological simulations, the expansion factor $a$ cannot vary by more than 10%: $\Delta t < 0.1 \times a/\dot{a}$.

In the end the timestep of cell $i$, $\Delta t_i$, is the minimum between these three (four for cosmological simulations) timesteps, and the global timestep of the simulation $\Delta t$ is the minimum between these $\Delta t_i$.

Again, on a grid with various levels, as some constraints depend on $\Delta x$, *i.e.* the size of the cell, it is clear that the timesteps of finer cells ($\Delta t_{l_{min}+2}$ using our sketch Fig. 44) will be shorter than the ones of coarser grid ($\Delta t_{l_{min}}$ using our sketch Fig. 44). However, it would be a waste of time to use $\Delta t_{l_{min}+2}$ to update the quantities of cells at level $l_{min}$... The

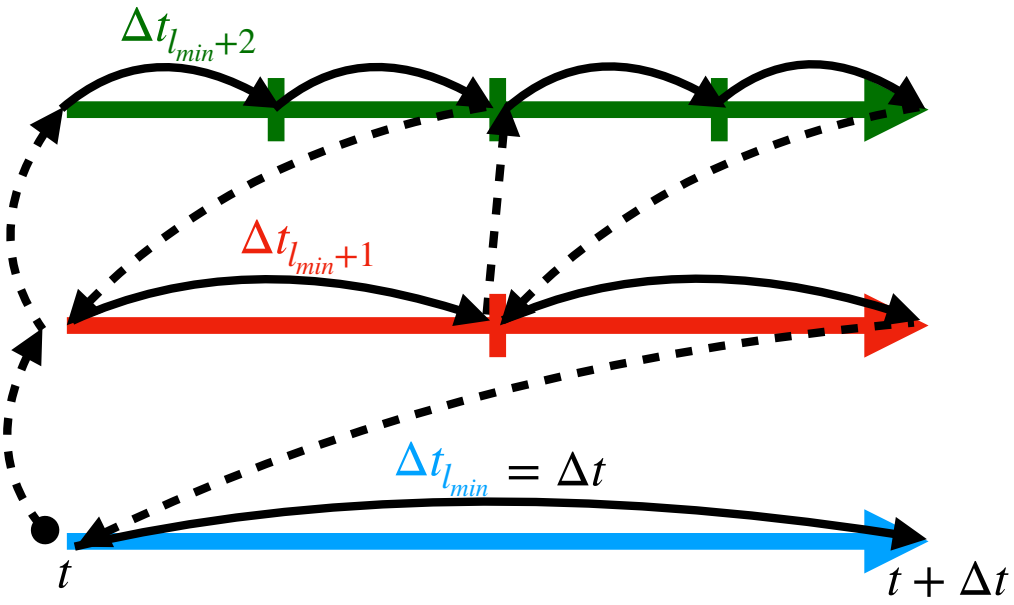


Figure 45: Timestep in `Ramses`, finer cells are evolved before coarser cells.

approach is therefore to compute the global coarse timestep $\Delta t$, using rescaled timesteps for finer levels, in our example:

$$\Delta t = \min(2^0 \Delta t_{l_{min}}, 2^1 \Delta t_{l_{min}+1}, 2^2 \Delta t_{l_{min}+2} ...). \tag{158}$$

And then to use this $\Delta t$ to update level $l_{min}$, $\Delta t/2$ for level $l_{min}+1$, $\Delta t/2^2$ for level $l_{min}+2$ etc... in the order described in Fig. 45.

### 6.2.3 *Domain decomposition*

Usually, even if we use the AMR, the computing time remains very high because computers can only perform a fixed amount of operations per second. To overcome this issue, we decompose space into different volume, as described in Fig. 46, and make each processors evolving the calculation on this domain with the method described in the Sections above. Note that this involves communications between processors at boundaries, as it is mandatory to know the properties of neighboring cells.

## 6.3 SUBGRID PHYSICS

Even with all the techniques described in §6.2, we cannot always achieve the resolution wanted. And some processes, important to understand galaxy evolution, are always below resolution. For this reason, astrophysical codes rely on "subgrid physics", that is physics which is (sometimes poorly) understood, which is relevant, but which we cannot resolve.

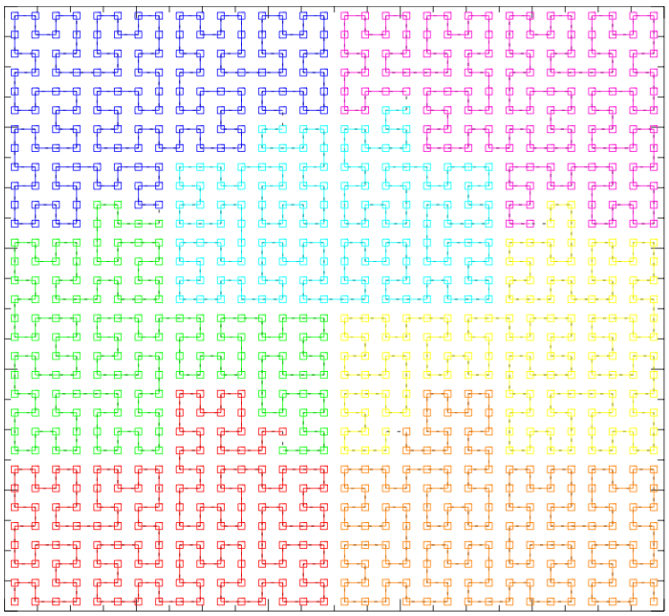

Figure 46: Domain decomposed, with the Peano-Hilbert curve, in 7 different domains. Taken from the Ramses User Guide.

In general, the subgrid physics used in numerical simulations has more impact than the gravity or hydrodynamical solver used. In this Section, we detail the subgrid physics used in `Ramses`.

### 6.3.1 *Cooling and Heating*

For metal rich gas, or gas hot enough to begin to collisionally ionize hydrogen ($T > 10^4\,K$), various atomic processes (recombination, collisional excitation and subsequent decay or Bremsstrahlung) are accompanied with the emission of photons, resulting in a loss of energy, and therefore of a decrease of the temperature: this is cooling. As these are two-body processes, the loss of energy per unit volume and time, *i.e.* the cooling rate $\mathcal{L}$, scales as the square of the number density $n$, and is usually written:

$$\mathcal{L} = n^2 \Lambda(T, Z)\,, \tag{159}$$

where $\Lambda$ is the cooling function and, at first order and in equilibrium, depends on the temperature $T$ and metallicity $Z$. Codes such as `Cloudy` (Ferland et al., 1998) compute all the different processes resulting in loss of energy, for different $T$ and $Z$, different species etc... We show an example in Fig. 47.

In practice, in `Ramses`, we use the cooling functions from Sutherland and Dopita, 1993, including contribution of hydrogen, helium and metals above $10^4\,K$, and from Rosen and

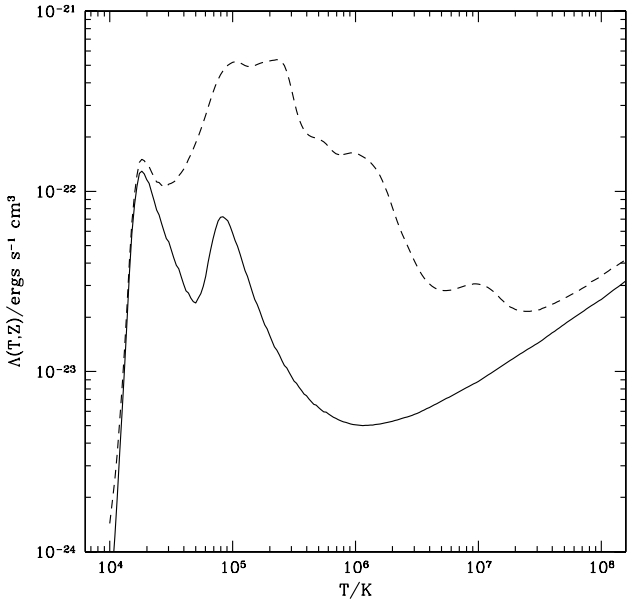


Figure 47: Cooling function as a function of temperature for a gas of primordial composition (solid line) and of Solar composition (dashed). Taken from Benson, 2010.

Bregman, 1995 below, down to 10 K. At each timestep, given the temperature $T$, metallicity[1] $Z$ and density $\rho$ measured in each cell, the variation of total energy per unit volume $e$ during the timestep $\Delta t$ is:

$$\Delta e = -\left(\frac{\rho}{\mu m_p}\right)^2 \Lambda(T,Z)\Delta t\,, \tag{160}$$

where $\mu$ is the mean molecular weight (1.25 for pristine gas and 0.7 for fully ionized gas) and $m_p$ the proton mass.

In addition, as discussed in Chapter 1, at some point, the Universe is fully reionized by the uniform UV background. As we do not track radiation emitted from stars nor AGNs, we have to add this background, source of energy and resulting in heating, by hand. Below $z \sim 8.5$, each cells total energy is increased by $\mathcal{H}\Delta t$ where $\mathcal{H}$ is computed following Haardt and Madau, 1996.

### 6.3.2 *Star formation*

In the early Universe, there were no stars, whereas today galaxies are full of them. It is therefore important to include star formation if we want to understand galaxy evolution. In simulations, resolution is typically (for the best) pc whereas a star radius is typically

1 The metallicity is modeled as a passive variable, moving with the flow and enhanced when a supernovae explode.

$10^{-8}$ pc. Therefore, we are far from resolving single stars. For this reason, stars are implemented as stellar particles (see §6.1.2.2), of mass $m_\star \gtrsim 10^3\,M_\odot$, which typically sample the initial mass function and represent a population of stars.

Observationally, it has been shown that the surface star formation rates, $\dot{\Sigma}_\star$, correlates well with the gas surface density, $\Sigma_{gas}$. Although there are many observational problems, coming from the fact that different tracers for star formation (H$\alpha$, UV, IR etc...) do not necessarily converge or that the gas surface density is hard to measure, the Kennicutt Law (Kennicutt, 1998) can be written as following:

$$\dot{\Sigma}_\star = (2.5 \pm 0.7) \times 10^{-4} \left( \frac{\Sigma_{gas}}{M_\odot\ pc^{-2}} \right)^{1.4\pm0.2} M_\odot\ yr^{-1}\ kpc^{-2} \tag{161}$$

Theoretically, this relation was expected: gas, under its own gravity, collapses to form stars. This suggests a correlation between the star formation rate and the gaseous density. To be more precise, Schmidt, 1959 expressed the star formation rate (per units volume), $\dot{\rho}_\star$, as the ratio between the density $\rho_{gas}$ and the time taken for a spherical gaseous sphere to collapse under its own gravity $t_{ff} = \sqrt{3\pi/(32\,G\,\rho)}$, this yields:

$$\dot{\rho}_\star = \epsilon \frac{\rho_{gas}}{t_{ff}} \tag{162}$$

where $\epsilon \sim 1\%$ is the star formation efficiency and has been calibrated to recover observations. This has been implemented in `Ramses` by Rasera and Teyssier, 2006: at each timestep $\Delta t$ and in each cell containing a gas mass $m_{gas} = \rho_{gas}\Delta x^3$, N stellar particles are formed, where N is drawn from a Poisson distribution:

$$P(N) = \frac{\lambda^N}{N!} e^{-\lambda} \tag{163}$$

with $\lambda = \epsilon \Delta t / t_{ff} m_{gas} m_\star$. Consequently, the mean mass of stars formed between $t$ and $t + \Delta t$ is $\lambda m_\star = \Delta t \Delta x^3 \dot{\rho}_\star$, where $\dot{\rho}_\star$ is computed using Eq. (162) and the star formation rate computed is correct. An additional criterion is used, indeed, if only Eq. (162) is used, stars can form everywhere, which is not what we see in the sky. For this reason a threshold density is used, $\rho_0$, and stars are allowed to form only if the density is above this value.

There has been a massive use of this implementation (Dubois et al., 2012; Dubois et al., 2014; Dubois, Volonteri, and Silk, 2014) however, better computers allowed to increase resolution and better understanding of star formation led to the development of more sophisticated models (Krumholz, McKee, and Klein, 2004; Federrath and Klessen, 2012; Kraljic et al., 2014). In particular, Federrath and Klessen, 2012 presents several models solving the following main issues we have when simply using the Schmidt law:

- The criterion based on the density to allow for star formation is quite arbitrary and strongly resolution dependant.
- The density is not the only parameter that should play a role, a more physical model for star formation would take into account the turbulence in the gas or the magnetic fields.
- There are no reason to consider the star formation efficiency constant.

We summarize here the implementation of multi-ff PN model presented in Federrath and Klessen, 2012, which (partly) solves these issues. The idea is to keep the Schmidt law but hide all the physics in $\epsilon$, which is not anymore constant and vary with the local properties of the fluid. They find, for the hydrodynamical case, without including magnetic fields:

$$\epsilon = \frac{1}{4\phi_t} \exp\left(\frac{3}{8}\sigma_s^2\right)\left[1 + \operatorname{erf}\left(\frac{\sigma_s^2 - s_{crit}}{\sqrt{2\sigma_s^2}}\right)\right], \tag{164}$$

with:

$$s_{crit} = \ln\left(0.067 \times \theta^{-2}\alpha_{vir}\mathcal{M}^2\right) \tag{165}$$

$$\sigma_s^2 = \ln\left[1 + b^2\mathcal{M}^2\right] \tag{166}$$

where $\mathcal{M} = u/c_s$ is the Mach number ($u$ is the speed of gas in each cell and $c_s$ the local sound speed); $\alpha_{vir} = 2E_{kin}/E_{grav}$ is the Virial parameter ($E_{kin} = 1/2u^2$ is the specific kinetic energy in each cell and $E_{grav} = 3/5\,G\,\rho(\Delta x)^2$ is the specific gravitational energy); and the parameters $1/\phi_t = 0.49$, $\theta = 0.97$ and $b = 0.4$ have been fitted to recover very high resolution simulations of molecular clouds, where the star formation is resolved and not treated as a subgrid model.

This prescription has the advantage of not being strongly dependent of the density threshold chosen. If it is very low then, in very dense regions dominated by gravity the efficiency is very high and in lower dense region, though above the threshold, the efficiency can be vanishingly small. Moreover, because the efficiency depends on the local properties of the fluid, star formation much clumpier, in better agreement with the idea of star nurseries that we observe (see Fig. 48).

### 6.3.3 *Supernovae feedback*

When massive stars have burned all their fuel, gravity overcomes radiative pressure resulting in an explosion: this is a supernovae[2]. From an observational perspective, the tremendous amount of energy released ($2 \times 10^{50}$ erg for a 10 $M_\odot$ star) can completely outshine

2 We consider only Type II supernovae, as the energy released in Type I A is lower.

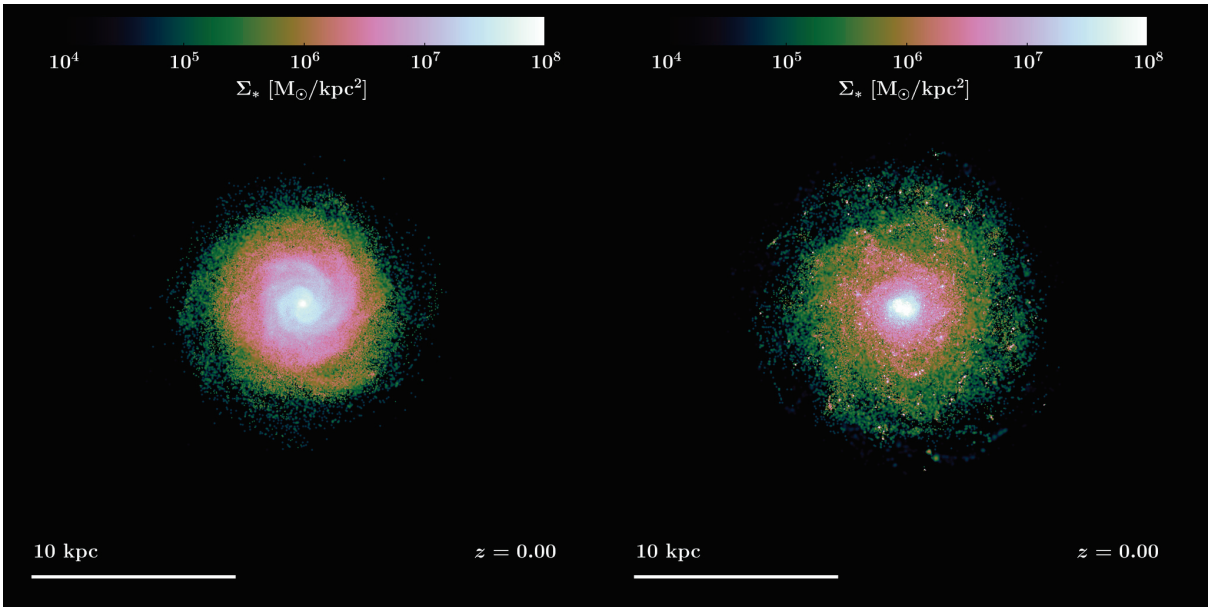


Figure 48: Exact same simulation run with the classical model for star formation (left) and the one adapted from Federrath and Klessen, 2012 (right). In the more physically motivated model, star formation is clumpy, as in real galaxies. Courtesy of Maxime Trebitsch.

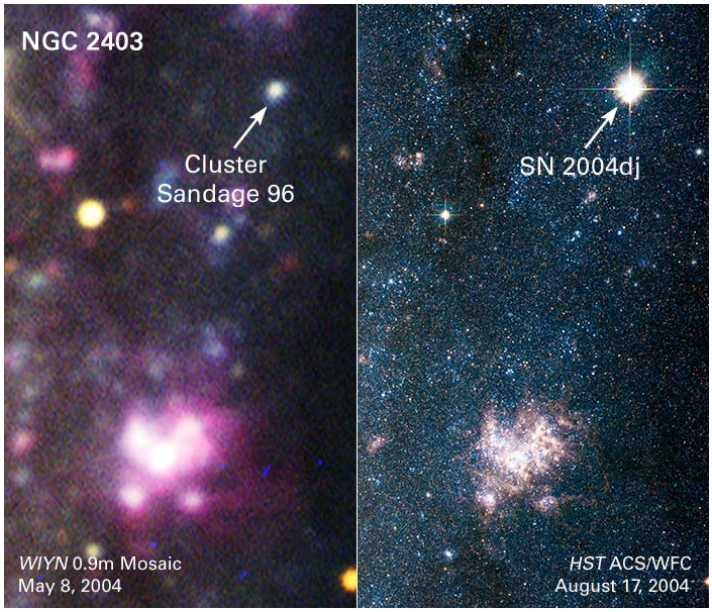


Figure 49: Same patch of the sky observed with a 3 month interval. A supernovae has exploded, outshining the entire galaxy. Taken from spacetelescope.org.

the host galaxy (see Fig. 49). From a theoretical perspective, the tremendous amount of energy released can affect the entire galaxy, heating the surrounding gas, releasing metals increasing the metallicity etc... All these processes are usually synthesized in the word feedback.

Similarly to star formation, feedback begins with single stars, therefore is far to be resolved in simulations and has to be treated as a subgrid model. Many attempts to simulate this have been done (Katz, 1992; Stinson et al., 2006; Dalla Vecchia and Schaye, 2012) releasing the energy either in thermal energy or kinetic energy. However, reality is more subtle and, in principle, there should be a fraction of the energy deposited of kinetic energy and the rest of thermal energy. Kimm and Cen, 2014 considers two distincts phases following a supernovae explosion:

1. The Sedov blastwave, just after the explosion, during which the shell swept up by the supernovae expands adiabatically. In this situation, cooling has not been efficient yet and both the energy and momentum are conserved. Analytical results of the Sedov solution can be used to estimate the fraction of kinetic and thermal energy deposited.

2. The snow-plow phase, when cooling has been efficient enough so that the energy has decreased. In this situation only momentum is conserved.

The transition between these two regime is obtained following the works of Blondin et al., 1998: if we consider $\chi$ as the ratio between the swept-up mass and the initially ejected mass, there exist a critical value for which we are in the Sedov phase or in the snow-plow phase. Additionally, Blondin et al., 1998 provided an expression for the amount of energy and momentum to deposit in the snow-plow phase.

### 6.3.4 *Black holes*

BHs have been the main topic of this Thesis, and therefore have to be included in our numerical simulations to track their dynamics, growth and effect on their surrounding galaxy. Again, the typical size of the BH (the Schwarzschild radius) is much smaller than our resolution, and BHs have to be treated as subgrid physics. We briefly describe here our implementation from Dubois et al., 2012.

In `Ramses`, similarly to dark matter and stars, BHs are modelled as a particle. Around the BH, "cloud particles" are uniformly displaced in a sphere of radius $4\Delta x$ and separated by $0.5\Delta x$ (about 2000 particles). These cloud particles are test particles, *i.e.* have a zero mass, and are used to sample the properties of surrounding gas, which will be needed to compute the accretion rate.

#### 6.3.4.1 *Formation*

The formation of BHs is still poorly understood (Volonteri and Bellovary, 2012) and therefore, our seeding model is extremely simple, although some better implementation for `Ramses` exist (Habouzit, Volonteri, and Dubois, 2017).

In each cell, if the stellar and gas density are larger than a threshold (we usually chose $\rho_{tr} = 100 \mathrm{amu\,cm^{-3}}$), and if no BH already exists within $r_{min} = 50\,\mathrm{kpc}$, a BH with its cloud particles is seeded with a mass $M_{\bullet,seed}$. The last condition is used to avoid forming multiple BHs in galaxies.

Consequently, we have here 3 free parameters: $\rho_{tr}$ and $r_{min}$, constant in all the simulations performed during this Thesis, and $M_{\bullet,seed}$ which we vary between $10^4$ and $10^5\,M_\odot$.

#### 6.3.4.2 *Growth*

Once the BH is seeded, it is allowed to grow through Bondi accretion (see §1.2.1). For this, we need the mean density $\tilde{\rho}$, sound speed $\tilde{c}_s$ and relative speed of the BH with respect to surrounding gas $\tilde{u}$, this is where cloud particles are used.

Consider for example $\tilde{\rho}$. Each cloud particle $i$ is in a cell with density $\rho_i$ and at a distance $r_i$ from the BH. $\tilde{\rho}$ is computed as:

$$\tilde{\rho} = \sum \rho_i \exp\left(-\frac{r_i^2}{r_\bullet^2}\right), \tag{167}$$

where:

$$r_\bullet \equiv \begin{cases} \frac{\Delta x}{4} & \text{if } r_B < \frac{\Delta x}{4} \\ r_B & \text{if } \frac{\Delta x}{4} < r_B < 2\Delta x \\ 2\Delta x & \text{if } 2\Delta x < r_B \end{cases} \tag{168}$$

with $r_B \equiv G\,M_\bullet/c_s$ is the Bondi radius measured at the location of the BH.

From this, the Bondi accretion rate can be computed. Note that, due to our inability to resolve the dense cold (large $\rho$, low $c_s$) regions around BHs, the accretion rate computed as is can be underestimated. For this reason, it is boosted by a density dependent factor introduced by Booth and Schaye, 2009:

$$\alpha = \max\left(\left(\frac{\tilde{\rho}}{\rho_\alpha}\right)^2, 1\right), \tag{169}$$

where $\rho_\alpha$ is a free parameter.

Finally, the accretion rate is capped at the Eddington rate corresponding to the accretion rate leading to a luminosity for which radiative pressure is larger than gravity in a spherically symmetric homogeneous medium:

$$\dot{M}_{Edd} = \frac{4\pi G\, M_\bullet\, m_p}{\epsilon_r \sigma_T c}\,, \tag{170}$$

where $m_p$ is the proton mass, $\epsilon_r \sim 0.1$ the radiative efficiency (the value depends on the spin of the BH, but with mean 0.1), $\sigma_T$ is the Thompson cross-section and $c$ the speed of light.

All this adds only one free parameter, $\rho_\alpha$ which we varied during this Thesis as:

$$\rho_\alpha = 500 \mathrm{amu\,cm^{-3}} \left(\frac{\Delta x}{\mathrm{pc}}\right)^{-1}. \tag{171}$$

#### 6.3.4.3 *Feedback*

As discussed in §1.2.1, a fraction of the mass accreted is radiated, heating and pushing the surrounding gas. Similarly to supernovae feedback, the energy can be deposited either through kinetic energy either through thermal energy (Combes, 2015).

It is believed that AGNs with low accretion rates (eddington ratio lower than 3%) launch jets which which mostly deposit kinetic energy (jet/radio mode), while at higher accretion rates, the energy is deposited through thermal energy (thermal/quasar mode) by winds (Merloni and Heinz, 2008). In `Ramses`, both modes are implemented.

In both cases, the energy deposited during $t$ and $t + \Delta t$ is:

$$E_{AGN} = \epsilon_r \epsilon_f \dot{M}_\bullet c^2 \Delta t\,, \tag{172}$$

where $\epsilon_f$ is the coupling efficiency, indicating how does the energy released couple with the gas. It is a free parameter (0.15 for thermal mode and 1 for jet mode) tuned to recover the $M_\bullet - \sigma$ relation (Kormendy and Ho, 2013).

For the thermal mode, the energy is uniformly distributed in all cells within $r_{AGN} \equiv 4\Delta x$ from the BH.

For the jet mode, we assume a cylindrical bipolar jet centered on the BH, with radius and height $r_{AGN}$. Its direction is parallel to the angular momentum of surrounding gas $\mathbf{L}$, computed with cloud particles as:

$$\mathbf{L} = \sum \rho_i \mathbf{r_i} \times \mathbf{v_i}\,, \tag{173}$$

where $\mathbf{r_i}$ and $\mathbf{v_i}$ are respectively the distance and velocity of the gas cell, hosting the cloud particle $i$, relative to the BH. The energy deposited depends on the radial distance to the axis of the cylinder:

$$\begin{aligned} E(r) &= \psi(r) E_{AGN} && (174)\\ &= \psi(r)\epsilon_r\epsilon_f \dot{M}_\bullet c^2 \Delta t\,, && (175)\end{aligned}$$

where:

$$\psi(r) \propto \exp\left(-\frac{r^2}{r_{AGN}^2}\right)\,, \qquad (176)$$

and sums up to 1 over the whole cylinder.

The momentum deposited depends on the radial distance to the BH and is:

$$\dot{p}_{Jet}(r)\Delta t = \dot{M}_{Jet}(r)\Delta t \times u_{Jet}(r)\,, \qquad (177)$$

where $\dot{M}_{Jet}(r)$ and $u_{Jet}(r)$ are respectively the mass deposited and its speed.

As all the energy is deposited through kinetic energy, we have:

$$\begin{aligned} E(r) &= \frac{1}{2}\dot{M}_{Jet}(r)\Delta t \times u_{Jet}^2(r) && (178)\\ &= \psi(r)\epsilon_r\epsilon_f \dot{M}_\bullet c^2 \Delta t\,. && (179)\end{aligned}$$

At our resolution (the jet is launched up to $4\Delta x \sim 100\,\mathrm{pc}$), similarly to supernovae explosion, mass has been swept up and the speed has greatly decreased. For this reason, we arbitrary introduce a mass–loading factor $\eta = 100$ corresponding to the enhancement of the mass deposited with respect to the one deposited close to the BH:

$$\dot{M}_{Jet}(r) = \eta\psi(r)\dot{M}_\bullet\,, \qquad (180)$$

which immediately leads to:

$$\begin{aligned} u_{Jet}(r) &= \sqrt{\frac{2\epsilon_r \epsilon f}{\eta}} c && (181)\\ &\sim 10^4\,\mathrm{km\ s^{-1}} \left(\frac{\epsilon_r}{0.1}\right)^{1/2} \left(\frac{\epsilon_f}{0.15}\right)^{1/2} \left(\frac{\eta}{100}\right)^{-1/2}\,. && (182)\end{aligned}$$

All this introduces three new free parameters: $r_{AGN} = 4\Delta x$, $\epsilon_f = 0.15$ $(= 1)$ for the thermal (jet) mode and $\eta = 100$, which we did not vary during this Thesis. We adopted the reference value from Dubois et al., 2012.

#### 6.3.4.4 *Dynamical friction*

As explained in Chapter 2, dynamical friction is important to understand the dynamics of BHs.

In `Ramses`, dynamical friction from gas following Ostriker, 1999 analytical estimate has been implemented by Dubois et al., 2012. An additional force is added to BHs:

$$\mathbf{F}_{DF,gas} = f_{gas} 4\pi \frac{\tilde{\rho} G^2 M_\bullet{}^2}{\tilde{c}_s^2}, \tag{183}$$

where $f_{gas}$ is a fudge factor depending on the Mach number (Ostriker, 1999; Chapon, Mayer, and Teyssier, 2013) and $\alpha$ is the boost factor discussed in §6.3.4.2. During this Thesis, we adopted $\alpha = 1$ in our simulations, but this parameter seems to greatly affect the growth of BHs and further studies are needed to fully understand its effects.

In addition to gas dynamical friction, we use the dark matter/stellar dynamical friction presented in §2.3.2.

#### 6.3.4.5 *Mergers*

Some groups (Di Matteo et al., 2012; Davé et al., 2019) run a halo finder on the fly, and automatically merge BHs which are in the same galaxy. This leads to instantaneous mergers while this process can take several Gyr (Tremmel et al., 2015; Pfister et al., 2019a).

In `Ramses`, we do not adopt this approach, following the dynamics of BHs separately until they are separated by $4\Delta x$. In this situation, if the gravitational energy of the binary is larger than the kinetic energy, BHs are merged.

## 6.4 INITIAL CONDITIONS

`Ramses` solves the hydrodynamical and gravity equations with additional subgrid physics. However, at the beginning of simulations, initial conditions have to be given. We briefly detail here how we proceeded during this Thesis.

### 6.4.1 *Cosmological simulations*

At high redshift, the Universe was mostly homogeneous, with small perturbations well approximated by a gaussian random field.

`Music` (Hahn and Abel, 2013) is made to produce high redshift conditions ($z \sim 100$) which depend on the cosmology chosen ($H_0$, $\Omega_{b,0}$ etc...) and produces outputs directly readable by `Ramses`.

This allows to simulate a patch of Universe from $z \sim 100$ down to current time (or higher $z$ if the computational power needed is too large). Note that in this situation, the size of the box evolves with time following Friedman–Lemaitre equations to simulate the expansion of the Universe.

### 6.4.2 *Ideal simulations*

Running a cosmological box with hundreds of thousands of galaxies is sometime too computationally expensive and lack the resolution needed to study in details some processes. In this situation, one can decide to initialize one or more galaxies with different masses, density profiles, positions, velocities etc...

`Dice` (Perret, 2016) is made to produce isolated stable galaxies in hydrostatic equilibrium which can then be placed at different position/velocity in a box, to simulate a galaxy merger for instance. Again, conveniently, the outputs of `Dice` can be read by `Ramses`.

We insist here that, initializing ideal simulations is slightly more technical than cosmological simulations. The reason is that the initial conditions are at hydrostatic equilibrium but, as soon as read by `Ramses`, cooling takes place and galaxies collapse. This leads to a burst of star formation (see Rosdahl et al., 2017 for instance) which is soon after followed by supernovae explosions, possibly destroying the disk. Some fine tuning on the mass of galaxies or the density profiles have to be made to overcome this issue.

## 6.5 THE SMOOTHED PARTICLE HYDRODYNAMICS CODE gasoline

Many different codes exist to solve the hydrodynamical equations (`GADGET`, Springel, 2005 – `ChaNGa`, Menon et al., 2015 – `Gizmo`, Hopkins, 2015 etc...). This is mandatory to make comparisons between different codes and be confident in our results.

During this Thesis, we also used `Gasoline` (Wadsley, Stadel, and Quinn, 2004) which, contrary to `Ramses`, does not use a grid but a Lagrangian approach with gas particle moving with the fluid (see Springel, 2014 for details). Each particles at position $\mathbf{r_i}$ carry the hydrodynamical quantities $F_i$ and, at position $\mathbf{r}$, $F$ can be computed as:

$$F(\mathbf{r}) = \sum F_i W(|\mathbf{r} - \mathbf{r_i}|, h_i)\,, \tag{184}$$

where $W$ is the kernel function, $h_i$ is the smoothing length (resolution) and, usually the sum is performed on the 32 or 64 closest neighbors. The resolution is adaptive in the sense that $h_i$ is shorter when particles are grouped, and vice versa.

Gravity is computed with a tree code: a grid in which each cell contains one particle is built. Then, a critical angle $\theta_{crit}$ is defined so that particles in cells with angular size $\theta < \theta_{crit}$ are grouped. For instance, using the sketch of Fig. 50, particles in the cell with

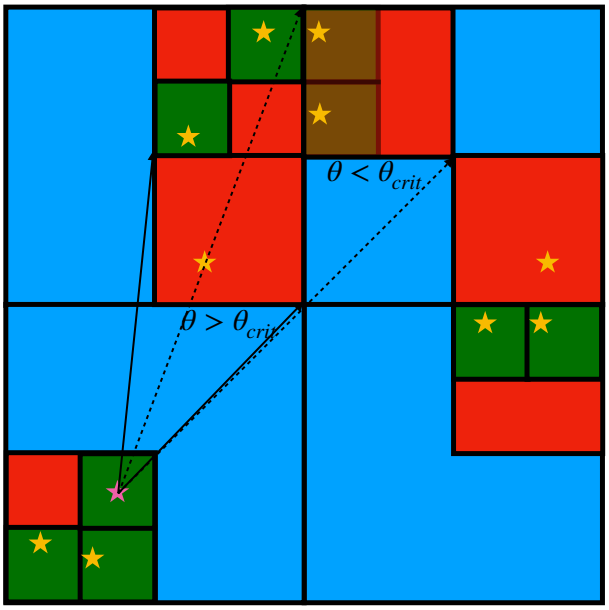


Figure 50: Sketch of the tree code used in `Gasoline`.

angular size defined by the dashed lines are consider as one more massive particles. Instead of having to compute $N^2/2$ forces for N particles, one can show that the complexity of this algorithm is $\mathcal{O}(N \log N)$ resulting in a much faster code.

The subgrid physics is slightly different than in `Ramses` (see Gabor et al., 2016, for a comparison) and details about the implementation can be found in:

- Shen, Wadsley, and Stinson, 2010 for the cooling ;
- Stinson et al., 2006 for star formation and supernovae feedback ;
- Bellovary et al., 2010 for BH accretion and feedback.

# 7

# HYPERBOLIC ENCOUNTERS

Research is like a house: solid foundations are required to get a step further, and it is from adding small pieces all together that complexity arises. In this Thesis, we used the simple results from hyperbolic encounters to understand Bondi–Hoyle accretion (see §1.2.1), dynamical friction (see §2.1) and express the relaxation timescale (see §4.1.3). For this reason, an excellent understanding of this simple problem is needed. We derive all the results in this Appendix.

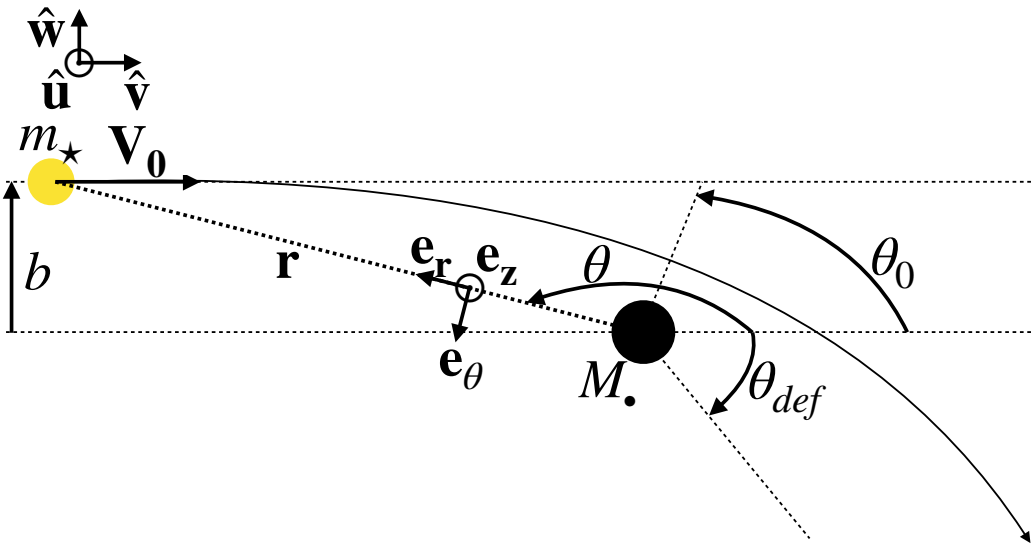


Figure 51: Sketch of a hyperbolic encounter, geometry used is cylindrical.

## 7.1 A SIMPLE PROBLEM WITH A SIMPLE EQUATION

The problem is sketched in Fig. 51: two particles with masses $m_\star$ and $M_\bullet$, at position $\mathbf{r}_\star$ and $\mathbf{r}_\bullet$ and moving with velocity $\mathbf{v}_\star$ and $\mathbf{v}_\bullet$ interact. The goal is to compute the dynamics of the two bodies.

We begin by writing Newton's law for both particles:

$$m_\star \frac{d\mathbf{v}_\star}{dt} = -\frac{G\, M_\bullet\, m_\star}{|\mathbf{r}_\star - \mathbf{r}_\bullet|^2} \frac{\mathbf{r}_\star - \mathbf{r}_\bullet}{|\mathbf{r}_\star - \mathbf{r}_\bullet|} \tag{185}$$

$$M_\bullet \frac{d\mathbf{v}_\bullet}{dt} = \frac{G\, M_\bullet\, m_\star}{|\mathbf{r}_\star - \mathbf{r}_\bullet|^2} \frac{\mathbf{r}_\star - \mathbf{r}_\bullet}{|\mathbf{r}_\star - \mathbf{r}_\bullet|}\,. \tag{186}$$

Considering the relative position of $m_\star$with respect to $M_\bullet$: $\mathbf{r} \equiv \mathbf{r}_\star - \mathbf{r}_\bullet$ with velocity $\mathbf{V} \equiv \mathbf{v}_\star - \mathbf{v}_\bullet$, after some simple transformation, we find:

$$\frac{d\mathbf{V}}{dt} = -\frac{G\,(M_\bullet + m_\star)}{r^2} \frac{\mathbf{r}}{r} \tag{187}$$

from which we immediately obtain that the angular momentum $\mathbf{L} \equiv \mathbf{r} \times \mathbf{V}$ is conserved. This implies that the dynamics is coplanar, justifying our sketch in Fig. 51, and we shall now use cylindrical coordinates $(r, \theta, z)$, for which we have:

$$\mathbf{L} = r^2 \dot{\theta} \mathbf{e}_z \tag{188}$$

$$\frac{d}{dt} = \frac{d}{d\theta}\frac{d\theta}{dt} = \frac{d}{d\theta} \times \frac{L}{r^2} \tag{189}$$

At $t = 0$, we assume that the distance between the two particles is infinite, with an impact parameter $b$ and a velocity $\mathbf{V_0} = V_0\hat{\mathbf{v}}$, resulting in an angular momentum $L = -bV_0$. Projecting Newton's law over $\mathbf{e_r}$, we have:

$$\ddot{r} - r\dot{\theta}^2 = -\frac{G(M_\bullet + m_\star)}{r^2} \tag{190}$$

$$\Leftrightarrow \quad L^2\frac{d}{d\theta}\left(\frac{1}{r^2}\frac{dr}{d\theta}\right) - \frac{L^2}{r} = -G(M_\bullet + m_\star)\,. \tag{191}$$

The last equation in $r$ depending on $\theta$ is the one we solve in the following.

## 7.2 A SIMPLE PROBLEM WITH A SIMPLE SOLUTION

### 7.2.1 *Distance between the two particles*

Using Binnet's transformation $u \equiv 1/r$, we have:

$$\frac{d^2u}{d\theta^2} + u = \frac{G(m_\star + M_\bullet)}{L^2} \tag{192}$$

leading to:

$$u = A\cos(\theta - \theta_0) + \frac{G(m_\star + M_\bullet)}{L^2} \tag{193}$$

$$= \frac{1}{r}\,, \tag{194}$$

with $A$ and $\theta_0$ integration constants. Additionally, we can express:

$$\frac{dr}{dt} = \frac{d}{dt}\left(\frac{1}{u}\right) \tag{195}$$

$$= LA\sin(\theta - \theta_0)\,. \tag{196}$$

We now use the initial conditions to obtain the integration constants. At $t = 0$, $\hat{\mathbf{v}} = -\mathbf{e_r}$ and $\theta = \pi$. From Eq. (193) and Eq. (196) , given our initial conditions, this yields:

$$0 = -A\cos(\theta_0) + \frac{G(m_\star + M_\bullet)}{L^2} \tag{197}$$

$$-V_0 = LA\sin(\theta_0)\,, \tag{198}$$

from which we obtain:

$$\tan(\theta_0) = -\frac{V_0 L}{G(m_\star + M_\bullet)} \tag{199}$$

$$= \frac{bV_0^2}{G(m_\star + M_\bullet)}\,. \tag{200}$$

From Eq. (193) it is clear that $u(r)$ is maximum (minimum) for $\theta = \theta_0$, say $r(\theta_0) = r_{min}$. As, in this situation we also have $dr/dt = 0$, by energy conservation this yields:

$$\frac{1}{2}V_0^2 = \frac{1}{2}\frac{L^2}{r_{min}^2} - \frac{G(m_\star + M_\bullet)}{r_{min}^2} \tag{201}$$

which unique positive solution is:

$$r_{min} = \frac{G(m_\star + M_\bullet)}{V_0^2}\left(-1 + \sqrt{1 + \frac{b^2V_0^4}{G^2(m_\star + M_\bullet)^2}}\right)\,. \tag{202}$$

Injecting this in Eq. (193) leads to:

$$A = \frac{1}{r_{min}} - \frac{G(m_\star + M_\bullet)}{L^2} \tag{203}$$

$$= \frac{G(m_\star + M_\bullet)}{b^2V_0^2}\sqrt{1 + \frac{b^2V_0^4}{G^2(m_\star + M_\bullet)^2}}\,. \tag{204}$$

With Eq. (193), Eq. (200) and Eq. (204) we have the expression of the distance between the two particles.

### 7.2.2 *Variation of the velocity*

We are also interested in how the velocities of $m_\star$ and $M_\bullet$ vary between $t = 0$ and $t = +\infty$.

Clearly, the problem is symmetrical with respect to $\theta_0$ and the deflection angle is:

$$\theta_{def} = -\pi + 2\theta_0\,. \tag{205}$$

This means that for $\theta_0 = \pi/4$, *i.e.* $b = G(m_\star + M_\bullet)/V_0^2 \equiv r_{def}$ (see Eq. (200)), $m_\star$ is deflected by 90°, and we introduced the deflection radius $r_{def}$.

At $t = +\infty$, through energy conservation, the final speed is $V_0$ and the variation obeys:

$$\Delta V_{\parallel} \equiv \Delta\mathbf{V}\cdot\hat{\mathbf{v}} = \cos(\theta_{def})V_0 - V_0 \tag{206}$$

$$\Delta V_{\perp} \equiv \Delta\mathbf{V}\cdot\hat{\mathbf{w}} = -\sin(\theta_{def})V_0\,. \tag{207}$$

After some calculations:

$$\Delta V_{\parallel} = -2V_0 \left[1 + \frac{b^2}{r_{def}^2}\right]^{-1} \tag{208}$$

$$\Delta V_{\perp} = -V_0 \frac{2b}{r_{def}} \left[1 + \frac{b^2}{r_{def}^2}\right]^{-1} . \tag{209}$$

In the limit $b >> r_{def}$, particles do not interact and the variation of velocity is zero.

If one wants to estimate the variation in $\mathbf{v}_\bullet$, by combining Eq. (185) and Eq. (186), we obtain:

$$\frac{d}{dt}(m_\star \mathbf{v}_\star + M_\bullet \mathbf{v}_\bullet) = 0 \tag{210}$$

$$\Rightarrow \quad m_\star \Delta \mathbf{v}_\star + M_\bullet \Delta \mathbf{v}_\bullet = 0 \tag{211}$$

$$\Rightarrow \quad \Delta \mathbf{v}_\bullet = -\frac{m_\star}{m_\star + M_\bullet} \Delta \mathbf{V} , \tag{212}$$

where we have used that $\Delta \mathbf{V} = \Delta \mathbf{v}_\star - \Delta \mathbf{v}_\bullet$. In the end, this yields:

$$\Delta v_{\bullet,\parallel} \equiv \Delta \mathbf{v}_\bullet \cdot \hat{\mathbf{v}} = V_0 \frac{2m_\star}{m_\star + M_\bullet} \left[1 + \frac{b^2}{r_{def}^2}\right]^{-1} \tag{213}$$

$$\Delta v_{\bullet,\perp} \equiv \Delta \mathbf{v}_\bullet \cdot \hat{\mathbf{w}} = V_0 \frac{b}{r_{def}} \frac{2m_\star}{m_\star + M_\bullet} \left[1 + \frac{b^2}{r_{def}^2}\right]^{-1} . \tag{214}$$

# BIBLIOGRAPHY


Abbott, B. P. et al. (Feb. 2016). "Observation of Gravitational Waves from a Binary Black Hole Merger." In: *Physical Review Letters* 116.6, 061102.

Ahn, Jieun, Juhan Kim, Jihye Shin, Sungsoo Kim, and Yun-Young Choi (Mar. 2014). "Halo Spin Parameter in Cosmological Simulations." In: *Journal of The Korean Astronomical Society* 47.

Alexander, T. and B. Bar-Or (Aug. 2017). "A universal minimal mass scale for present-day central black holes." In: *Nature Astronomy* 1, 0147.

Amaro-Seoane, P. et al. (Feb. 2017). "Laser Interferometer Space Antenna." In: *ArXiv e-prints*.

Amaro-Seoane, Pau, M. Coleman Miller, and Gareth F. Kennedy (2012). "Tidal disruptions of separated binaries in galactic nuclei." In: *MNRAS* 425.4.

Amaro-Seoane, Pau, Cristián Maureira-Fredes, Massimo Dotti, and Monica Colpi (2016). "Retrograde binaries of massive black holes in circumbinary accretion discs." In: *AAP* 591, A114.

Antonini, F. and D. Merritt (Jan. 2012). "Dynamical Friction around Supermassive Black Holes." In: *ApJ* 745, 83.

Arcavi, I. et al. (Sept. 2014). "A Continuum of H- to He-rich Tidal Disruption Candidates With a Preference for E+A Galaxies." In: *ApJ* 793, 38.

Armano, M. et al. (Feb. 2018). "Beyond the Required LISA Free-Fall Performance: New LISA Pathfinder Results down to 20 μ Hz." In: *Physical Review Letters* 120.6, 061101.

Aubert, D., C. Pichon, and S. Colombi (Aug. 2004). "The origin and implications of dark matter anisotropic cosmic infall on ˜L$_*$ haloes." In: *MNRAS* 352.

Auchettl, K., E. Ramirez-Ruiz, and J. Guillochon (Jan. 2018). "A Comparison of the X-Ray Emission from Tidal Disruption Events with those of Active Galactic Nuclei." In: *ApJ* 852, 37.

Auchettl, Katie, James Guillochon, and Enrico Ramirez-Ruiz (2017). "New Physical Insights about Tidal Disruption Events from a Comprehensive Observational Inventory at X-Ray Wavelengths." In: *ApJ* 838.2, 149.

Bañados, E. et al. (Jan. 2018). "An 800-million-solar-mass black hole in a significantly neutral Universe at a redshift of 7.5." In: *Nature* 553.

Bahcall, J. N. and R. A. Wolf (Oct. 1976). "Star distribution around a massive black hole in a globular cluster." In: *ApJ* 209.

Bar-Or, Ben and Tal Alexander (2016). "Steady-state Relativistic Stellar Dynamics Around a Massive Black hole." In: *ApJ* 820.2, 129.

Baron, D., H. Netzer, J. X. Prochaska, Z. Cai, S. Cantalupo, D. C. Martin, M. Matuszewski, A. M. Moore, P. Morrissey, and J. D. Neill (Nov. 2018). "Direct evidence of AGN feedback: a post-starburst galaxy stripped of its gas by AGN-driven winds." In: *MRAS* 480.

Beckmann, R. S., A. Slyz, and J. Devriendt (July 2018). "Bondi or not Bondi: the impact of resolution on accretion and drag force modelling for supermassive black holes." In: *MNRAS* 478.

Behroozi, P. S., R. H. Wechsler, and C. Conroy (June 2013). "The Average Star Formation Histories of Galaxies in Dark Matter Halos from z = 0-8." In: *ApJ* 770, 57.

Bellm, Eric C., Shrinivas R. Kulkarni, Matthew J. Graham, Richard Dekany, Roger M. Smith, Reed Riddle, Frank J. Masci, George Helou, Thomas A. Prince, and Scott M. Adams (2019). "The Zwicky Transient Facility: System Overview, Performance, and First Results." In: *PASP* 131.995.

Bellovary, J. M., F. Governato, T. R. Quinn, J. Wadsley, S. Shen, and M. Volonteri (Oct. 2010). "Wandering Black Holes in Bright Disk Galaxy Halos." In: *ApJ* 721.

Bellovary, J. M., C. E. Cleary, F. Munshi, M. Tremmel, C. R. Christensen, A. Brooks, and T. R. Quinn (Jan. 2019). "Multimessenger signatures of massive black holes in dwarf galaxies." In: *MNRAS* 482.

Benson, A. J. (Oct. 2010). "Galaxy formation theory." In: *physrep* 495.

Biernacki, P., R. Teyssier, and A. Bleuler (July 2017). "On the dynamics of supermassive black holes in gas-rich, star-forming galaxies: the case for nuclear star cluster co-evolution." In: *MNRAS* 469.

Binney, J. and S. Tremaine (1987). *Galactic Dynamics*. First. Princeton Series in Astrophysics. Princeton University Press.

Blain, A. W., Allon Jameson, Ian Smail, M. S. Longair, J. P. Kneib, and R. J. Ivison (1999). "Dust-obscured star formation and AGN fuelling in hierarchical models of galaxy evolution." In: *MNRAS* 309.3.

Blondin, J. M., E. B. Wright, K. J. Borkowski, and S. P. Reynolds (June 1998). "Transition to the Radiative Phase in Supernova Remnants." In: *ApJ* 500.

Bogdanović, Tamara, Roseanne M. Cheng, and Pau Amaro-Seoane (2014). "Disruption of a Red Giant Star by a Supermassive Black Hole and the Case of PS1-10jh." In: *ApJ* 788.2, 99.

Bogdanović, Tamara, Michael Eracleous, Suvrath Mahadevan, Steinn Sigurdsson, and Pablo Laguna (2004). "Tidal Disruption of a Star by a Black Hole: Observational Signature." In: *ApJ* 610.2.

Bondi, H. (1952). "On spherically symmetrical accretion." In: *MNRAS* 112.

Bondi, H. and F. Hoyle (1944). "On the mechanism of accretion by stars." In: *MNRAS* 104.

Bonetti, M., F. Haardt, A. Sesana, and E. Barausse (July 2018). "Post-Newtonian evolution of massive black hole triplets in galactic nuclei - II. Survey of the parameter space." In: *MNRAS* 477.

Booth, C. M. and J. Schaye (Sept. 2009). "Cosmological simulations of the growth of supermassive black holes and feedback from active galactic nuclei: method and tests." In: *MNRAS* 398.

Bournaud, F. (2011). "Star formation in galaxy interactions and mergers." In: *EAS Publications Series*. Ed. by Corinne Charbonnel and Thierry Montmerle. Vol. 51. EAS Publications Series.

Buchert, T. (1989). "A class of solutions in Newtonian cosmology and the pancake theory." In: *AAP* 223.1-2.

Bullock, J. S., A. Dekel, T. S. Kolatt, A. V. Kravtsov, A. A. Klypin, C. Porciani, and J. R. Primack (July 2001). "A Universal Angular Momentum Profile for Galactic Halos." In: *ApJ* 555.

Callegari, S., L. Mayer, S. Kazantzidis, M. Colpi, F. Governato, T. Quinn, and J. Wadsley (May 2009). "Pairing of Supermassive Black Holes in Unequal-Mass Galaxy Mergers." In: *ApJ* 696.

Capelo, P. R., M. Volonteri, M. Dotti, J. M. Bellovary, L. Mayer, and F. Governato (Mar. 2015). "Growth and activity of black holes in galaxy mergers with varying mass ratios." In: *MNRAS* 447.

Chandrasekhar, S. (Mar. 1943). "Dynamical Friction. I. General Considerations: the Coefficient of Dynamical Friction." In: *ApJ* 97.

Chapon, D., L. Mayer, and R. Teyssier (Mar. 2013). "Hydrodynamics of galaxy mergers with supermassive black holes: is there a last parsec problem?" In: *MNRAS* 429.

Chen, Xian, Piero Madau, Alberto Sesana, and F. K. Liu (2009). "Enhanced Tidal Disruption Rates from Massive Black Hole binaries." In: *The Astrophysical Journal* 697.2.

Choi, Ena, Rachel S. Somerville, Jeremiah P. Ostriker, Thorsten Naab, and Michaela Hirschmann (2018). "The Role of Black Hole Feedback on Size and Structural Evolution in Massive Galaxies." In: *ApJ* 866.2, 91.

Cibinel, A., E. Le Floc'h, V. Perret, F. Bournaud, E. Daddi, M. Pannella, D. Elbaz, P. Amram, and P. A. Duc (2015). "A Physical Approach to the Identification of High-z Mergers: Morphological Classification in the Stellar Mass Domain." In: *ApJ* 805.2, 181.

Cohn, H. and R. M. Kulsrud (1978). "The stellar distribution around a black hole: numerical integration of the Fokker-Planck equation." In: *ApJ* 226.

Colpi, M., L. Mayer, and F. Governato (Nov. 1999). "Dynamical Friction and the Evolution of Satellites in Virialized Halos: The Theory of Linear Response." In: *ApJ* 525.

Colpi, M. and A. Pallavicini (July 1998). "Drag on a Satellite Moving across a Spherical Galaxy: Tidal and Frictional Forces in Short-lived Encounters." In: *ApJ* 502.

Combes, Françcoise (2015). "Models of AGN feedback." In: *Galaxies in 3D across the Universe*. Ed. by Bodo L. Ziegler, Françoise Combes, Helmut Dannerbauer, and Miguel Verdugo. Vol. 309. IAU Symposium.

Dai, L., J. C. McKinney, N. Roth, E. Ramirez-Ruiz, and M. C. Miller (June 2018). "A Unified Model for Tidal Disruption Events." In: *ApJ* 859, L20.

Dalla Vecchia, Claudio and Joop Schaye (2012). "Simulating galactic outflows with thermal supernova feedback." In: *MNRAS* 426.1.

Dashyan, Gohar, Ena Choi, Rachel S. Somerville, Thorsten Naab, Amanda C. N. Quirk, Michaela Hirschmann, and Jeremiah P. Ostriker (2019). "AGN-driven quenching of satellite galaxies." In: *arXiv e-prints*, arXiv:1906.07431.

Davé, Romeel, Daniel Anglés-Alcázar, Desika Narayanan, Qi Li, Mika H. Rafieferantsoa, and Sarah Appleby (2019). "SIMBA: Cosmological simulations with black hole growth and feedback." In: *MNRAS* 486.2.

Di Matteo, P., F. Bournaud, M. Martig, F. Combes, A. L. Melchior, and B. Semelin (2008). "On the frequency, intensity, and duration of starburst episodes triggered by galaxy interactions and mergers." In: *AAP* 492.1.

Di Matteo, T., V. Springel, and L. Hernquist (Feb. 2005). "Energy input from quasars regulates the growth and activity of black holes and their host galaxies." In: *Nature* 433.

Di Matteo, T., N. Khandai, C. DeGraf, Y. Feng, R. A. C. Croft, J. Lopez, and V. Springel (Feb. 2012). "Cold Flows and the First Quasars." In: *ApJ* 745, L29.

Dosopoulou, F. and F. Antonini (May 2017). "Dynamical Friction and the Evolution of Supermassive Black Hole Binaries: The Final Hundred-parsec Problem." In: *ApJ* 840, 31.

Dubois, Y., M. Volonteri, and J. Silk (May 2014). "Black hole evolution - III. Statistical properties of mass growth and spin evolution using large-scale hydrodynamical cosmological simulations." In: *MNRAS* 440.

Dubois, Y., J. Devriendt, A. Slyz, and R. Teyssier (Mar. 2012). "Self-regulated growth of supermassive black holes by a dual jet-heating active galactic nucleus feedback mechanism: methods, tests and implications for cosmological simulations." In: *MNRAS* 420.

Dubois, Y. et al. (Oct. 2014). "Dancing in the dark: galactic properties trace spin swings along the cosmic web." In: *MNRAS* 444.

Escala, A., R. B. Larson, P. S. Coppi, and D. Mardones (Sept. 2005). "The Role of Gas in the Merging of Massive Black Holes in Galactic Nuclei. II. Black Hole Merging in a Nuclear Gas Disk." In: *ApJ* 630.

Faber, S. M., S. Tremaine, E. A. Ajhar, Y.-I. Byun, A. Dressler, K. Gebhardt, C. Grillmair, J. Kormendy, T. R. Lauer, and D. Richstone (Nov. 1997). "The Centers of Early-Type Galaxies with HST. IV. Central Parameter Relations." In: *ApJ* 114.

Fakhouri, O., C.-P. Ma, and M. Boylan-Kolchin (Aug. 2010). "The merger rates and mass assembly histories of dark matter haloes in the two Millennium simulations." In: *MNRAS* 406.

Federrath, C. and R. S. Klessen (Dec. 2012). "The Star Formation Rate of Turbulent Magnetized Clouds: Comparing Theory, Simulations, and Observations." In: *ApJ* 761, 156.

Ferland, G. J., K. T. Korista, D. A. Verner, J. W. Ferguson, J. B. Kingdon, and E. M. Verner (1998). "CLOUDY 90: Numerical Simulation of Plasmas and Their Spectra." In: *PASP* 110.749.

Fiacconi, D., L. Mayer, R. Roškar, and M. Colpi (Nov. 2013). "Massive Black Hole Pairs in Clumpy, Self-gravitating Circumnuclear Disks: Stochastic Orbital Decay." In: *ApJ* 777, L14.

Friedmann, A. (1922). "Über die Krümmung des Raumes." In: *Zeitschrift fur Physik* 10.

Gabor, J. M. and Frédéric Bournaud (2013). "Simulations of supermassive black hole growth in high-redshift disc galaxies." In: *MNRAS* 434.1.

Gabor, J. M., P. R. Capelo, M. Volonteri, F. Bournaud, J. Bellovary, F. Governato, and T. Quinn (July 2016). "Comparison of black hole growth in galaxy mergers with GASOLINE and RAMSES." In: *AAP* 592, A62.

Georgiev, I. Y., T. Böker, N. Leigh, N. Lützgendorf, and N. Neumayer (Apr. 2016). "Masses and scaling relations for nuclear star clusters, and their co-existence with central black holes." In: *MNRAS* 457.

Gezari, S. et al. (May 2012). "An ultraviolet-optical flare from the tidal disruption of a helium-rich stellar core." In: *Nature* 485.

Glass, L. et al. (Jan. 2011). "The ACS Fornax Cluster Survey. IV. Deprojection of the Surface Brightness Profiles of Early-type Galaxies in the Virgo and Fornax Clusters: Investigating the "Core/Power-law Dichotomy"." In: *ApJ* 726, 31.

Goicovic, F. G., A. Sesana, J. Cuadra, and F. Stasyszyn (Feb. 2016). "Infalling clouds on to supermassive black hole binaries - II. Binary evolution and the final parsec problem." In: *ArXiv e-prints*.

Goulding, Andy D., Jenny E. Greene, Rachel Bezanson, Johnny Greco, Sean Johnson, Alexie Leauthaud, Yoshiki Matsuoka, Elinor Medezinski, and Adrian M. Price-Whelan (2018). "Galaxy interactions trigger rapid black hole growth: An unprecedented view from the Hyper Suprime-Cam survey." In: *PASJ* 70, S37.

Governato, F., M. Colpi, and L. Maraschi (Nov. 1994). "The fate of central black holes in merging galaxies." In: *MNRAS* 271.

Graur, O., K. D. French, H. J. Zahid, J. Guillochon, K. S. Mandel, K. Auchettl, and A. I. Zabludoff (Jan. 2018). "A Dependence of the Tidal Disruption Event Rate on Global Stellar Surface Mass Density and Stellar Velocity Dispersion." In: *ApJ* 853, 39.

Gruzinov, Andrei, Yuri Levin, and Christopher D. Matzner (2019). "Negative Dynamical Friction on compact objects moving through dense gas." In: *arXiv e-prints*, arXiv:1906.01186.

Guillochon, J. and E. Ramirez-Ruiz (Apr. 2013). "Hydrodynamical Simulations to Determine the Feeding Rate of Black Holes by the Tidal Disruption of Stars: The Importance of the Impact Parameter and Stellar Structure." In: *ApJ* 767, 25.

Haardt, Francesco and Piero Madau (1996). "Radiative Transfer in a Clumpy Universe. II. The Ultraviolet Extragalactic Background." In: *ApJ* 461.

Habouzit, Mélanie, Marta Volonteri, and Yohan Dubois (2017). "Blossoms from black hole seeds: properties and early growth regulated by supernova feedback." In: *MNRAS* 468.4.

Hahn, O. and T. Abel (Nov. 2013). *MUSIC: MUlti-Scale Initial Conditions*. Astrophysics Source Code Library.

Hernquist, L. (June 1990). "An analytical model for spherical galaxies and bulges." In: *ApJ* 356.

Hills, J. G. (Mar. 1975). "Possible power source of Seyfert galaxies and QSOs." In: *Nature* 254.

Hopkins, Philip F. (2015). "A new class of accurate, mesh-free hydrodynamic simulation methods." In: *MNRAS* 450.1.

Hubble, E. P. (May 1925). "Cepheids in spiral nebulae." In: *The Observatory* 48.

Hubble, E. (Mar. 1929). "A Relation between Distance and Radial Velocity among Extra-Galactic Nebulae." In: *Proceedings of the National Academy of Science* 15.

Johansson, Peter H., Thorsten Naab, and Andreas Burkert (2009). "Equal- and Unequal-Mass Mergers of Disk and Elliptical Galaxies with Black Holes." In: *ApJ* 690.1.

Katz, Neal (1992). "Dissipational Galaxy Formation. II. Effects of Star Formation." In: *ApJ* 391.

Kauffmann, Guinevere et al. (2003). "Stellar masses and star formation histories for $10^5$ galaxies from the Sloan Digital Sky Survey." In: *MNRAS* 341.1.

Kaviraj, S., C. Laigle, T. Kimm, J. E. G. Devriendt, Y. Dubois, C. Pichon, A. Slyz, E. Chisari, and S. Peirani (June 2017). "The Horizon-AGN simulation: evolution of galaxy properties over cosmic time." In: *MNRAS* 467.

Kennicutt Jr., R. C. (May 1998). "The Global Schmidt Law in Star-forming Galaxies." In: *ApJ* 498.

Kimm, T. and R. Cen (June 2014). "Escape Fraction of Ionizing Photons during Reionization: Effects due to Supernova Feedback and Runaway OB Stars." In: *ApJ* 788, 121.

Kocevski, Dale D., S. M. Faber, Mark Mozena, Anton M. Koekemoer, Kirpal Nandra, Cyprian Rangel, Elise S. Laird, Marcella Brusa, Stijn Wuyts, and Jonathan R. Trump (2012). "CANDELS: Constraining the AGN-Merger Connection with Host Morphologies at z $\sim$2." In: *ApJ* 744.2, 148.

Kormendy, J. and L. C. Ho (Aug. 2013). "Coevolution (Or Not) of Supermassive Black Holes and Host Galaxies." In: *ARAA* 51.

Kraljic, Katarina, Florent Renaud, Frédéric Bournaud, Françoise Combes, Bruce Elmegreen, Eric Emsellem, and Romain Teyssier (2014). "The Role of Turbulence in Star Formation Laws and Thresholds." In: *ApJ* 784.2, 112.

Krumholz, Mark R., Christopher F. McKee, and Richard I. Klein (2004). "Embedding Lagrangian Sink Particles in Eulerian Grids." In: *ApJ* 611.1.

LIGO Scientific Collaboration et al. (Apr. 2015). "Advanced LIGO." In: *Classical and Quantum Gravity* 32.7, 074001.

Lacey, C. and S. Cole (June 1993). "Merger rates in hierarchical models of galaxy formation." In: *MNRAS* 262.

Laigle, C et al. (2017). "COSMOS2015 photometric redshifts probe the impact of filaments on galaxy properties." In: *MNRAS* 474.4.

Lauer, T. R. et al. (July 2007). "The Centers of Early-Type Galaxies with Hubble Space Telescope. VI. Bimodal Central Surface Brightness Profiles." In: *ApJ* 664.

Law-Smith, J., E. Ramirez-Ruiz, S. L. Ellison, and R. J. Foley (Nov. 2017). "Tidal Disruption Event Host Galaxies in the Context of the Local Galaxy Population." In: *ApJ* 850, 22.

Law, Nicholas M. et al. (2009). "The Palomar Transient Factory: System Overview, Performance, and First Results." In: *PASP* 121.886.

Leavitt, H. S. (1908). "1777 variables in the Magellanic Clouds." In: *Annals of Harvard College Observatory* 60.

Lemaître, G. (1927). "Un Univers homogène de masse constante et de rayon croissant rendant compte de la vitesse radiale des nébuleuses extra-galactiques." In: *Annales de la Société Scientifique de Bruxelles* 47.

Lezhnin, K. and E. Vasiliev (Apr. 2019). "Evolution of supermassive black hole binaries and tidal disruption rates in non-spherical galactic nuclei." In: *MNRAS* 484.

Li, Shuo, F. K. Liu, Peter Berczik, and Rainer Spurzem (2017). "Boosted Tidal Disruption by Massive Black Hole Binaries During Galaxy Mergers from the View of N-Body Simulation." In: *ApJ* 834, 195.

Lightman, A. P. and S. L. Shapiro (Jan. 1977). "The distribution and consumption rate of stars around a massive, collapsed object." In: *ApJ* 211.

Lin, D. et al. (June 2018). "A luminous X-ray outburst from an intermediate-mass black hole in an off-centre star cluster." In: *Nature Astronomy* 2.

Maggiore, Michele (2008). *Gravitational waves. Vol 1, Theory and Experiments*. Oxford University Press (OUP).

Maksym, W. Peter, M. P. Ulmer, and Michael Eracleous (2010). "A Tidal Disruption Flare in A1689 from an Archival X-ray Survey of Galaxy Clusters." In: *ApJ* 722.2.

Matthews, B.W. (1975). "Comparison of the predicted and observed secondary structure of T4 phage lysozyme." In: *Biochimica et Biophysica Acta (BBA) - Protein Structure* 405.2.

McKee, C. F. (1999). "The Dynamical Structure and Evolution of Giant Molecular Clouds." In: *NATO Advanced Science Institutes (ASI) Series C*. Ed. by C. J. Lada and N. D. Kylafis. Vol. 540. NATO Advanced Science Institutes (ASI) Series C.

McMillan, P. J. (July 2011). "Mass models of the Milky Way." In: *MNRAS* 414.

Menon, H., L. Wesolowski, G. Zheng, P. Jetley, L. Kale, T. Quinn, and F. Governato (Mar. 2015). "Adaptive techniques for clustered N-body cosmological simulations." In: *Computational Astrophysics and Cosmology* 2, 1.

Merloni, A. et al. (2012). "eROSITA Science Book: Mapping the Structure of the Energetic Universe." In: *arXiv e-prints*, arXiv:1209.3114.

Merloni, Andrea and Sebastian Heinz (2008). "A synthesis model for AGN evolution: supermassive black holes growth and feedback modes." In: *MNRAS* 388.3.

Merritt, D. (2013). *Dynamics and Evolution of Galactic Nuclei*. Princeton University Press.

Messier, C. (1781). *Catalogue des Nébuleuses et des Amas d'Étoiles (Catalog of Nebulae and Star Clusters)*. Tech. rep.

Mezcua, M. (May 2017). "Observational evidence for intermediate-mass black holes." In: *ArXiv e-prints*.

Mihos, J. C. and L. Hernquist (June 1996). "Gasdynamics and Starbursts in Major Mergers." In: *ApJ* 464.

Milosavljević, M. and D. Merritt (Dec. 2001). "Formation of Galactic Nuclei." In: *ApJ* 563.

Milosavljević, Miloš, David Merritt, and Luis C. Ho (2006). "Contribution of Stellar Tidal Disruptions to the X-Ray Luminosity Function of Active Galaxies." In: *ApJ* 652.1.

Mockler, Brenna, James Guillochon, and Enrico Ramirez-Ruiz (2019). "Weighing Black Holes Using Tidal Disruption Events." In: *ApJ* 872.2, 151.

Muñoz-Cuartas, J. C., A. V. Macciò, S. Gottlöber, and A. A. Dutton (Feb. 2011). "The redshift evolution of $\Lambda$ cold dark matter halo parameters: concentration, spin and shape." In: *MNRAS* 411.

Naab, Thorsten and Jeremiah P. Ostriker (2017). "Theoretical Challenges in Galaxy Formation." In: *ARAA* 55.1.

Navarro, J. F., C. S. Frenk, and S. D. M. White (Dec. 1997). "A Universal Density Profile from Hierarchical Clustering." In: *ApJ* 490.

Ostriker, E. C. (Mar. 1999). "Dynamical Friction in a Gaseous Medium." In: *ApJ* 513.

Panter, B., A. F. Heavens, and R. Jimenez (Dec. 2004). "The mass function of the stellar component of galaxies in the Sloan Digital Sky Survey." In: *MNRAS* 355.

Park, KwangHo and Tamara Bogdanović (2017). "Gaseous Dynamical Friction in Presence of Black Hole Radiative Feedback." In: *ApJ* 838.2, 103.

Pasquet, J., E. Bertin, M. Treyer, S. Arnouts, and D. Fouchez (Jan. 2019). "Photometric redshifts from SDSS images using a convolutional neural network." In: *AAP* 621, A26.

Peng, Ying-jie et al. (2010). "Mass and Environment as Drivers of Galaxy Evolution in SDSS and zCOSMOS and the Origin of the Schechter Function." In: *ApJ* 721.1.

Perret, V. (July 2016). *DICE: Disk Initial Conditions Environment*. Astrophysics Source Code Library.

Peter, A. H. G. (Jan. 2012). "Dark Matter: A Brief Review." In: *arXiv e-prints*.

Peter, Patrick and Jean-Philippe Uzan (2009). *Primordial cosmology*. Oxford Graduate Texts. Oxford: Oxford Univ. Press.

Peters, P. C. (1964). "Gravitational Radiation and the Motion of Two Point Masses." In: *Physical Review* 136.4B.

Pfister, H. and M. Dotti (in prep). "From galaxy pairs to galaxy mergers." In:

Pfister, Hugo, Alessandro Lupi, Pedro R. Capelo, Marta Volonteri, Jillian M. Bellovary, and Massimo Dotti (2017). "The birth of a supermassive black hole binary." In: *MNRAS* 471.3.

Pfister, Hugo, Marta Volonteri, Yohan Dubois, Massimo Dotti, and Monica Colpi (2019a). "The erratic dynamical life of black hole seeds in high-redshift galaxies." In: *MNRAS* 486.1.

Pfister, Hugo, Ben Bar-Or, Marta Volonteri, Yohan Dubois, and Pedro R. Capelo (2019b). "Tidal disruption event rates in galaxy merger remnants." In: *MNRAS*.

Phinney, E. S. (1989). "Manifestations of a Massive Black Hole in the Galactic Center." In: *The Center of the Galaxy*. Ed. by M. Morris. Vol. 136. IAU Symposium.

Pichon, C., E. Thiébaut, S. Prunet, K. Benabed, S. Colombi, T. Sousbie, and R. Teyssier (Jan. 2010). "ASKI: full-sky lensing map-making algorithms." In: *MNRAS* 401.

Planck Collaboration et al. (Sept. 2016). "Planck 2015 results. XIII. Cosmological parameters." In: *AAP* 594, A13.

Power, C., J. F. Navarro, A. Jenkins, C. S. Frenk, S. D. M. White, V. Springel, J. Stadel, and T. Quinn (Jan. 2003). "The inner structure of ΛCDM haloes - I. A numerical convergence study." In: *MNRAS* 338.

Quinlan, G. D. (July 1996). "The dynamical evolution of massive black hole binaries I. Hardening in a fixed stellar background." In: 1.

Quinlan, Gerald D., Lars Hernquist, and Steinn Sigurdsson (1995). "Models of Galaxies with Central Black Holes: Adiabatic Growth in Spherical Galaxies." In: *ApJ* 440.

Rantala, Antti, Pauli Pihajoki, Peter H. Johansson, Thorsten Naab, Natalia Lahén, and Till Sawala (2017). "Post-Newtonian Dynamical Modeling of Supermassive Black Holes in Galactic-scale Simulations." In: *ApJ* 840.1, 53.

Rasera, Y. and R. Teyssier (Jan. 2006). "The history of the baryon budget. Cosmic logistics in a hierarchical universe." In: *AAP* 445.

Rauch, Kevin P. and Brian Ingalls (1998). "Resonant tidal disruption in galactic nuclei." In: *MNRAS* 299.4.

Rauch, Kevin P. and Scott Tremaine (1996). "Resonant relaxation in stellar systems." In: *New Astronomy* 1.2.

Rees, M. J. (June 1988). "Tidal disruption of stars by black holes of 10 to the 6th-10 to the 8th solar masses in nearby galaxies." In: *Nature* 333.

Robitaille, T. P. and B. A. Whitney (Feb. 2010). "The Present-Day Star Formation Rate of the Milky Way Determined from Spitzer-Detected Young Stellar Objects." In: *ApJ* 710.

Rodriguez, C., G. B. Taylor, R. T. Zavala, A. B. Peck, L. K. Pollack, and R. W. Romani (July 2006). "A Compact Supermassive Binary Black Hole System." In: *ApJ* 646.

Rosdahl, J., J. Schaye, Y. Dubois, T. Kimm, and R. Teyssier (Apr. 2017). "Snap, crackle, pop: sub-grid supernova feedback in AMR simulations of disc galaxies." In: *MNRAS* 466.

Rosen, Alexander and Joel N. Bregman (1995). "Global Models of the Interstellar Medium in Disk Galaxies." In: *ApJ* 440.

Roškar, Rok, Davide Fiacconi, Lucio Mayer, Stelios Kazantzidis, Thomas R. Quinn, and James Wadsley (2015). "Orbital decay of supermassive black hole binaries in clumpy multiphase merger remnants." In: *MNRAS* 449.1.

Schaye, J. et al. (Jan. 2015). "The EAGLE project: simulating the evolution and assembly of galaxies and their environments." In: *MNRAS* 446.

Schmidt, M. (Mar. 1959). "The Rate of Star Formation." In: *ApJ* 129.

Schneider, R., A. Ferrara, P. Natarajan, and K. Omukai (May 2002). "First Stars, Very Massive Black Holes, and Metals." In: *ApJ* 571.

Sesana, A., F. Haardt, and P. Madau (Nov. 2006). "Interaction of Massive Black Hole Binaries with Their Stellar Environment. I. Ejection of Hypervelocity Stars." In: *ApJ* 651.

Shen, S., J. Wadsley, and G. Stinson (Sept. 2010). "The enrichment of the intergalactic medium with adiabatic feedback - I. Metal cooling and metal diffusion." In: *MNRAS* 407.

Shen, Y. et al. (June 2011). "A Catalog of Quasar Properties from Sloan Digital Sky Survey Data Release 7." In: *ApJ* 194, 45.

Shima, E., T. Matsuda, H. Takeda, and K. Sawada (Nov. 1985). "Hydrodynamic calculations of axisymmetric accretion flow." In: *MNRAS* 217.

Silk, Joseph and Martin J. Rees (1998). "Quasars and galaxy formation." In: *AAP* 331.

Smith, B., J. Regan, T. Downes, M. Norman, B. O'Shea, and J. Wise (Apr. 2018). "The Growth of Black Holes from Population III Remnants in the Renaissance Simulations." In: *ArXiv e-prints*.

Snyder, G. F., J. M. Lotz, V. Rodriguez-Gomez, R. d. S. Guimarães, P. Torrey, and L. Hernquist (June 2017). "Massive close pairs measure rapid galaxy assembly in mergers at high redshift." In: *MNRAS* 468.

Somerville, R. S. and R. Davé (Aug. 2015). "Physical Models of Galaxy Formation in a Cosmological Framework." In: *ARAA* 53.

Souza Lima, R., L. Mayer, P. R. Capelo, and J. M. Bellovary (Oct. 2016). "The Pairing of Accreting Massive Black Holes in Multiphase Circumnuclear Disks: the Interplay between Radiative Cooling, Star Formation, and Feedback Processes." In: *ArXiv e-prints*.

Spitzer Lyman, Jr. (1942). "The Dynamics of the Interstellar Medium. III. Galactic Distribution." In: *ApJ* 95.

Spitzer Jr., L. and R. Harm (May 1958). "Evaporation of Stars from Isolated Clusters." In: *ApJ* 127.

Springel, V. (Dec. 2014). "High performance computing and numerical modelling." In: *ArXiv e-prints*.

Springel, Volker (2005). "The cosmological simulation code GADGET-2." In: *MNRAS* 364.4.

Stadel, J. G. (2001). "Cosmological N-body simulations and their analysis." PhD thesis. UNIVERSITY OF WASHINGTON.

Steinborn, L. K., K. Dolag, M. Hirschmann, R.-S. Remus, and A. F. Teklu (June 2016). "AGN and their host galaxies." In: *The Interplay between Local and Global Processes in Galaxies,*

Stinson, G., A. Seth, N. Katz, J. Wadsley, F. Governato, and T. Quinn (Dec. 2006). "Star formation and feedback in smoothed particle hydrodynamic simulations - I. Isolated galaxies." In: *MNRAS* 373.

Stone, N. C. and B. D. Metzger (Jan. 2016). "Rates of stellar tidal disruption as probes of the supermassive black hole mass function." In: *MNRAS* 455.

Stone, N. C. and S. van Velzen (July 2016). "An Enhanced Rate of Tidal Disruptions in the Centrally Overdense E+A Galaxy NGC 3156." In: *ApJ* 825, L14.

Sutherland, R. S. and M. A. Dopita (Sept. 1993). "Cooling functions for low-density astrophysical plasmas." In: *ApJ* 88.

Syer, D. and A. Ulmer (June 1999). "Tidal disruption rates of stars in observed galaxies." In: *MNRAS* 306.

Tadhunter, C., R. Spence, M. Rose, J. Mullaney, and P. Crowther (Mar. 2017). "A tidal disruption event in the nearby ultra-luminous infrared galaxy F01004-2237." In: *Nature Astronomy* 1, 0061.

Taffoni, G., L. Mayer, M. Colpi, and F. Governato (May 2003). "On the life and death of satellite haloes." In: *MNRAS* 341.

Teyssier, R. (Apr. 2002). "Cosmological hydrodynamics with adaptive mesh refinement. A new high resolution code called RAMSES." In: *AAP* 385.

The LIGO Scientific Collaboration and the Virgo Collaboration (2017). "GW170817: Observation of Gravitational Waves from a Binary Neutron Star Inspiral." In: *Physical Review Letters* 119.16.

The LIGO Scientific Collaboration and the Virgo Collaboration (Nov. 2018). "GWTC-1: A Gravitational-Wave Transient Catalog of Compact Binary Mergers Observed by LIGO and Virgo during the First and Second Observing Runs." In: *arXiv e-prints*.

Toomre, A. (1977). "Mergers and Some Consequences." In: *Evolution of Galaxies and Stellar Populations*. Ed. by B. M. Tinsley and R. B. G. Larson D. Campbell.

Toro, Eleuterio F. (1997). *Riemann Solvers and Numerical Methods for Fluid Dynamics*. Springer-Verlag Berlin Heidelberg.

Tremmel, M., F. Governato, M. Volonteri, and T. R. Quinn (Aug. 2015). "Off the beaten path: a new approach to realistically model the orbital decay of supermassive black holes in galaxy formation simulations." In: *MNRAS* 451.

Tremmel, M., F. Governato, M. Volonteri, A. Pontzen, and T. R. Quinn (Apr. 2018). "Wandering Supermassive Black Holes in Milky-Way-mass Halos." In: *ApJ* 857, L22.

Tweed, D., J. Devriendt, J. Blaizot, S. Colombi, and A. Slyz (Nov. 2009). "Building merger trees from cosmological N-body simulations. Towards improving galaxy formation models using subhaloes." In: *AAP* 506.

Van Wassenhove, S., P. R. Capelo, M. Volonteri, M. Dotti, J. M. Bellovary, L. Mayer, and F. Governato (Mar. 2014). "Nuclear coups: dynamics of black holes in galaxy mergers." In: *MNRAS* 439.

Vasiliev, E. (Jan. 2019). "AGAMA: action-based galaxy modelling architecture." In: *MNRAS* 482.

Vasiliev, Eugene (Oct. 2017). "A New Fokker-Planck Approach for the Relaxation-driven Evolution of Galactic Nuclei." In: *ApJ* 848, 10.

Vasiliev, Eugene, Fabio Antonini, and David Merritt (2014). "The Final-parsec Problem in Nonspherical Galaxies Revisited." In: *ApJ* 785.2, 163.

Vogelsberger, M., S. Genel, D. Sijacki, P. Torrey, V. Springel, and L. Hernquist (Dec. 2013). "A model for cosmological simulations of galaxy formation physics." In: *MNRAS* 436.

Voges, W. et al. (1999). "The ROSAT all-sky survey bright source catalogue." In: *AAP* 349.

Volonteri, M. and R. Perna (Apr. 2005). "Dynamical evolution of intermediate-mass black holes and their observable signatures in the nearby Universe." In: *MNRAS* 358.

Volonteri, M., Y. Dubois, C. Pichon, and J. Devriendt (Aug. 2016). "The cosmic evolution of massive black holes in the Horizon-AGN simulation." In: *MNRAS* 460.

Volonteri, Marta and Jillian Bellovary (2012). "Black holes in the early Universe." In: *Reports on Progress in Physics* 75.12, 124901.

Wadsley, J. W., J. Stadel, and T. Quinn (Feb. 2004). "Gasoline: a flexible, parallel implementation of TreeSPH." In: 9.

Wang, J. and D. Merritt (Jan. 2004). "Revised Rates of Stellar Disruption in Galactic Nuclei." In: *ApJ* 600.

Weber, J. (1968). "Gravitational-Wave-Detector Events." In: *Physical Review Letters* 20.23.

Weber, J. (1969). "Evidence for Discovery of Gravitational Radiation." In: *Physical Review Letters* 22.24.

Weinberg, M. D. (1986). "Orbital Decay of Satellite Galaxies in Spherical Systems." In: *ApJ* 300.

Wheeler, J. Craig, Rafaella Margutti, Ryan Chornock, Dan Milisavljevic, Maryam Modjaz, and Sung-Chul Yoon (2019). "ELT Contributions to Tidal Disruption Events." In: *arXiv e-prints*, arXiv:1903.01575.

Yang, Yujin, Ann I. Zabludoff, Dennis Zaritsky, and J. Christopher Mihos (2008). "The Detailed Evolution of E+A Galaxies into Early Types." In: *ApJ* 688.

Zhong, Shiyan, Peter Berczik, and Rainer Spurzem (2014). "Super Massive Black Hole in Galactic Nuclei with Tidal Disruption of Stars." In: *ApJ* 792.2, 137.

del Valle, L. and A. Escala (Dec. 2012). "Binary-Disk Interaction: Gap-opening Criteria." In: *ApJ* 761, 31.

del Valle, L. and M. Volonteri (Oct. 2018). "The effect of AGN feedback on the migration time-scale of supermassive black holes binaries." In: *MNRAS* 480.

van Velzen, S., G. R. Farrar, S. Gezari, N. Morrell, D. Zaritsky, L. Östman, M. Smith, J. Gelfand, and A. J. Drake (Nov. 2011). "Optical Discovery of Probable Stellar Tidal Disruption Flares." In: *ApJ* 741, 73.